SMA-Induced Deformations in General Unsymmetric Laminates

Marie-Laure Dano

Dissertation submitted to the Faculty of the Virginia Polytechnic Institute and State University in partial fulfillment of the requirements for the degree of

Doctor of Philosophy
in
Engineering Mechanics

M. W. Hyer, Chair
O. H. Griffin, Jr.
E. R. Johnson
F. Lalande
D. H. Morris

April 22, 1997
Blacksburg, Virginia

Keywords: Shape Control, Modeling of Smart Structures, Instability, Snap Through

SMA-Induced Deformations in General Unsymmetric Laminates

Marie-Laure Dano

(ABSTRACT)

General unsymmetric laminates exhibit large natural curvatures at room temperature. Additionally, inherent to most unsymmetric laminates is the presence of two stable configurations. Multiple configurations and stability issues arise because of the geometric nonlinearities associated with the large curvatures. The laminate can be changed from one stable configuration to the other by a simple snap-through action. This situation offers the opportunity to use shape memory alloys (SMA) attached to the laminate to generate the snap-through forces and change the shape of the laminate on command. Presented is a model which can predict SMA-induced deformations in general unsymmetric laminates and, particularly, the occurrence of the snap through. First, a methodology is developed to predict the deformations of flat general unsymmetric epoxy-matrix composite laminates as they are cooled from their elevated cure temperature. Approximations to the strain fields are used in the expression for the total potential energy, and the Rayleigh-Ritz approach is used to study equilibrium. To further study the laminate deformations, finite-element analyses are performed. Experimental results are presented which confirm the predictions of the developed theory and the finite-element analyses regarding the existence of multiple solutions and the magnitude of the deformations. Results are compared with those of several other investigators. Next, the deformation behavior of general unsymmetric laminates subjected to applied forces is studied. The principle of virtual work is used to derive the equilibrium equations relating the laminate deformations to the applied forces. By solving the equilibrium equations as a function of the force level, relations between the laminate deformations and the applied force are derived, and the force level at which the laminate changes shape is determined. Finally, an existing SMA constitutive model is implemented into the developed theory to predict the deformations of simple structures to SMA-induced forces. Experiments on a narrow aluminium plate with an externally attached SMA actuator are conducted. The experimental results show good agreement with the predictions from the developed theory. Next, the deformation behavior of general unsymmetric laminates subjected to SMA actuators is predicted using the developed theory. Experiments using SMA actuators to generate the snap through of unsymmetric laminates are conducted. Good correlation with the developed theory is obtained.

Acknowledgments

I wish to express my gratitude to my advisor Prof. M. W. Hyer for his technical and professional guidance, constant support, and encouragement throughout the completion of this dissertation. I would also like to thank my committee members Profs. O. H. Griffin Jr., E. R. Johnson, F. Lalande, and D. H. Morris for their technical and editorial guidance. I am grateful to the Center for Intelligent Material Systems and Structures for allowing me to use their laboratory facilities and equipment. Special thanks are due to the personal of the Department of Engineering Science and Mechanics, especially Bob Simonds, Bill Shaver and Archie Montgomery for their technical support, Cindy Hopkins for her administrative assistance, and Beverly Williams for making my work days more enjoyable. The partial financial support for this research by the Center for Composite Material and Structures and by the NASA Langley Research Center, through grant NAG-1-343, is also greatly appreciated. I am also grateful to my friends who contributed to making these six years in Blacksburg an unforgettable experience. Finally, I would like to thank my family, especially, my parents and brother, Stéphane, for their love and support during all my studies. Very special thanks are due to my husband, Luc, for his love, ever-present encouragement, patience, and understanding.

Table of Contents

List of Figures

List of Tables

Chapter 1 Introduction

1.1 Concept

A significant amount of research is being conducted to design flexible structures that can adapt to a changing environment. Interest lies, especially, in the use of strain actuation to control structural deformations. Strain actuation can be induced by so-called smart materials like piezoelectric ceramics and shape memory alloys. Shape memory alloys, commonly denoted SMAs, are alloys that are able to engender large displacements and large actuation forces when heated. Piezoelectric ceramic materials, on the other hand, are limited to small displacement and force levels. Because of their unique features, shape-memory alloys can be used as actuators to generate large deflections in structures, and thus they can be used to actually control the shape of structures.

Interest grows also in the use of unsymmetric laminates in structures. Unsymmetric laminates offer the advantage of exhibiting natural large curvatures at room temperature. The curvatures develop during the cooling of a flat laminate from the elevated cure temperature to room temperature. During the cooling process, differences in thermal expansion in the different layers cause the laminate to warp out of plane. The resulting out-of-plane deflection can become quite large at room temperature, possibly up to one hundred times the laminate thickness. Because of their naturally curved shape, unsymmetric laminates offer interesting potential in structural applications. For example, they offer an inexpensive alternative to manufacturing curved panels. Rather than using expensive curved molds, only flat caul plates are necessary to manufacture curved panels. Another feature inherent to most unsymmetric laminates is the presence of two stable configurations at room temperature. Most familiar, perhaps, are the shapes of a cross-ply unsymmetric laminate. At room temperature this laminate can assume one of two configurations. One configuration has a cylindrical shape with its generator parallel to the *y* axis. The other configuration has another cylindrical shape with a curvature equal in magnitude but opposite in sign to the first cylinder, and with its generator parallel to the *x* axis. The laminate can be changed from one cylindrical configuration to another by a simple snap-through action. There is actually a third configuration, namely one with a saddle shape, with the curvature in the *y* direction equal and opposite to the curvature in the *x* direction. However, a stability analysis indicates that the saddle shape corresponds to an unstable configuration and is thus never observed in practice. Figure 1-1 depicts these three equilibrium configurations for a $[0_2/90_2]_T$ graphite-epoxy 12 in.

square laminate. The vertical scale is the out-of-plane displacement, *w*, normalized by the laminate thickness, *H*. The two horizontal scales are normalized by laminate side length, *L*. Note the large out-of-plane deflections of the cylindrical shapes relative to the deflections of the saddle shape. The existence of two equilibrium configurations with significantly different shapes presents interesting opportunities. It may be possible to use SMAs as a means of providing the snap-through forces and changing the shape on command. The simplest way to use SMA to generate forces on the laminates would be to attach SMA in wire form on the laminate surfaces, as depicted in Fig. 1-2. This figure shows two pairs of supports fastened to the unsymmetric laminate, one pair on the top surface (in the *y*-*z* plane) and one pair one the bottom surface (in the *x*-*z* plane). Plastically stretched SMA wires are attached to each pair of supports. When resistively

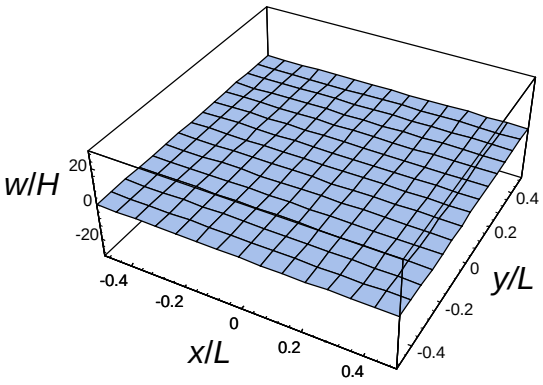

(a) Curing temperature: flat

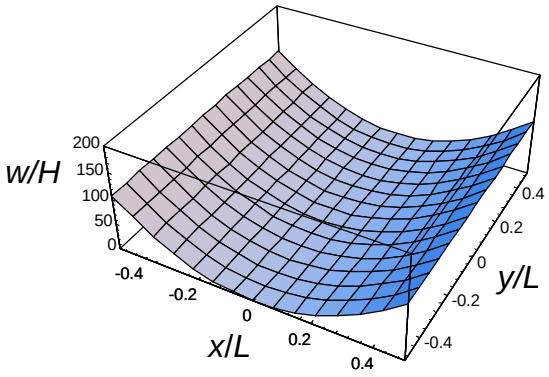

(b) Room-temperature: stable cylindrical with curvature in the *x* direction

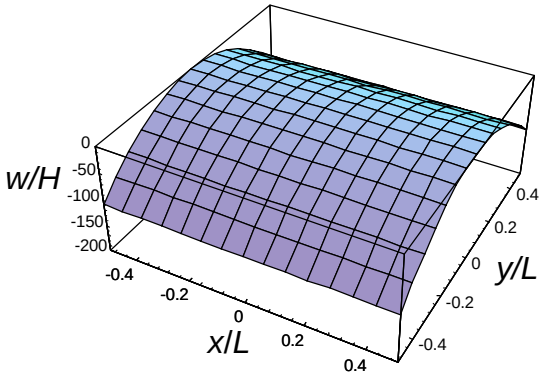

(c) Room-temperature: stable cylindrical with curvature in the *y* direction

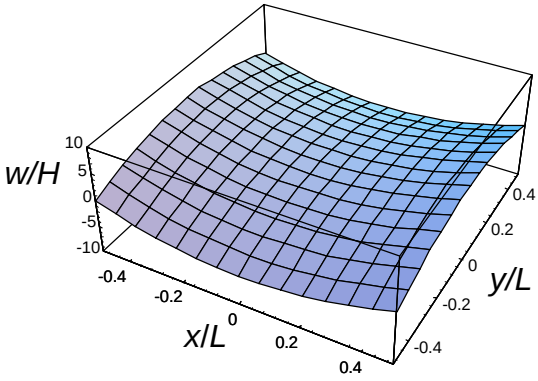

(d) Room-temperature: unstable saddle

Fig. 1-1. Shapes of $[0_2/90_2]_T$ laminate

heated by applying voltage, the plastically deformed SMA wire tends to recover its original shape and shrinks. Since the wire is restrained, it is not able to contract freely and thus forces are generated in the wire. These forces, as shown in Fig. 1-3 (a), produce moments. When the actuated force reaches a certain level, the laminate will snap to the other cylindrical shape, Fig. 1-3 (b). Then, by activating the SMA wire fastened on the top surface, the laminate will snap back to its initial shape, Fig. 1-3 (a). This could result in a system that suddenly changes stiffness. For example, with the configuration of Fig. 1-1 (b) and with forces *F* which act in the *x* direction applied to the edges of the laminate, as depicted in Fig. 1-4 (a), the bending stiffness D_{11} is the primary source of resistance to the forces. On the other hand, with the configuration of Fig. 1-1c, forces in the *x* direction are resisted by the extensional stiffness A_{11}, as illustrated in Fig. 1-4 (b). Since A_{11} is much larger than D_{11}, if the configuration changes from that of Fig. 1-4(a) to that of

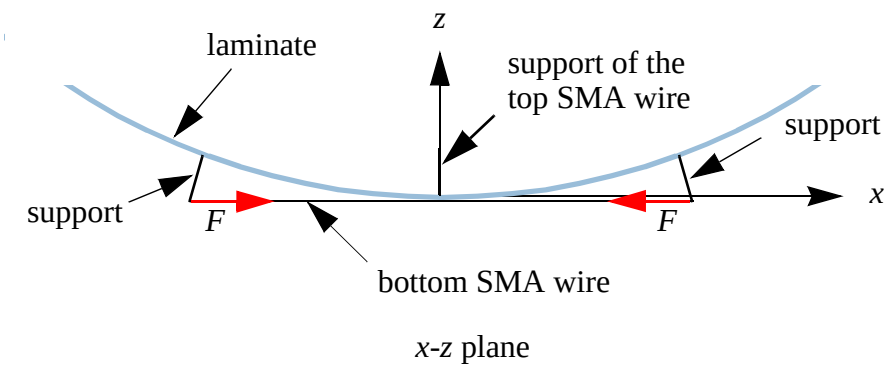

Fig. 1-2. SMA wire attached to an unsymmetric laminate

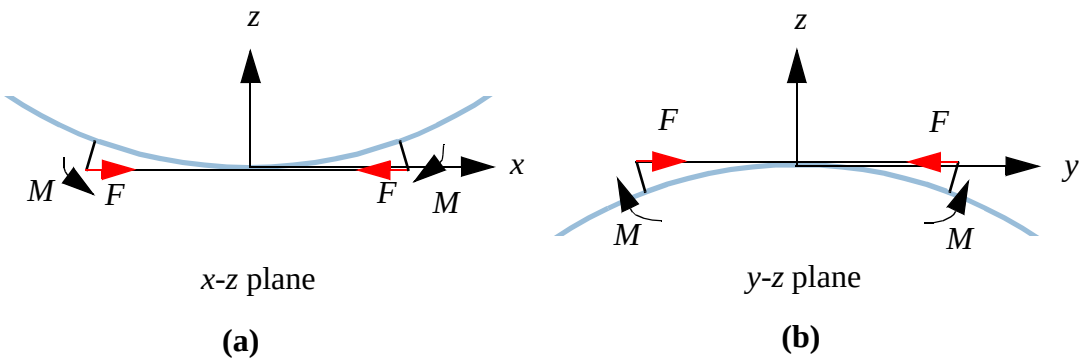

Fig. 1-3. Force actuation and laminate shape change

Fig. 1-4 (b), then the stiffness of the system suddenly increases. A change back to the configuration of Fig. 1-4 (a) suddenly reduces the stiffness again. Other potential applications include using one or more unsymmetric cross-ply laminates as portions of a conduit transporting a fluid, as shown in Fig. 1-5. A sudden change in the configuration of the conduit is possible by snapping the laminate from one configuration to another. This change in wall geometry could change the flow in the conduit on command. The feasibility of using SMA actuators to change the shape of cross-ply unsymmetric laminates has been demonstrated by Dano [1]. In this work the author developed a theory to predict the deformations of cross-ply unsymmetric laminates subjected to simple applied forces [2]. Experiments with SMA actuators to generate the snapping force were successfully conducted and proved that SMA actuators can be used efficiently to change the shape of cross-ply unsymmetric laminates.

The present work is an extension of the work originally done by Dano [1], which was restricted to cross-ply unsymmetric laminates. The work presented in this document focuses on the use of SMA in conjunction with the inherent shape characteristics of general unsymmetric laminates at room temperature. Specifically, the overall objective is to obtain a good understanding of the mechanics involved when using SMA actuators to provide the snap-through forces necessary to produce a change of shape of general unsymmetric laminates. To achieve this,

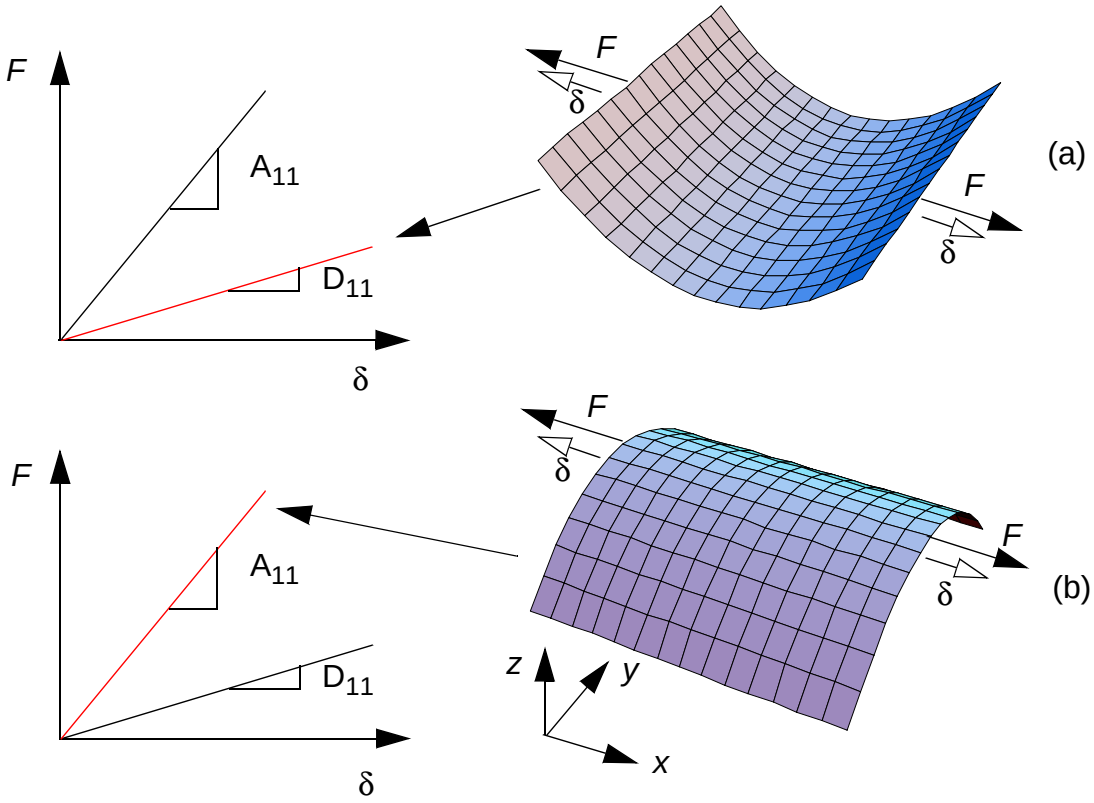

Fig. 1-4. Example of application: Unsymmetric laminates used as a bi-stiffness spring

the following steps should be accomplished. First, the shapes of general unsymmetric laminates that occur during cooling from cure should be clearly understood by developing an appropriate model. Especially important is the occurrence of several equilibrium configurations during cooling, and the room-temperature shapes. Second, the deformation behavior of general unsymmetric laminates subjected to applied actuation forces should be correctly described, particularly the snap through which occurs at a certain applied force level. The third step consists of having SMA wires used as actuators to generate the forces applied on the unsymmetric laminates. This involves combining a constitutive model for SMAs with the model of the unsymmetric laminates theory so the deformations induced by the SMA actuators on the unsymmetric laminates can be predicted as a function of the temperature of the SMA wire. By controlling the voltage in the SMA wire, and thus its temperature, the shape of unsymmetric laminates can be modified. At a certain temperature, the forces induced by the SMA actuators will be large enough to make the laminate snap into another configuration. Finally, the several representative unsymmetric laminates should be fabricated and SMA wires attached. The observed configuration changes of the laminate as a function of wire temperature or voltage should be compared with predictions.

To follow are reviews of the work to date in the areas of research relevant to the current work. Following these, specific objectives are defined, and the organization of this document is described.

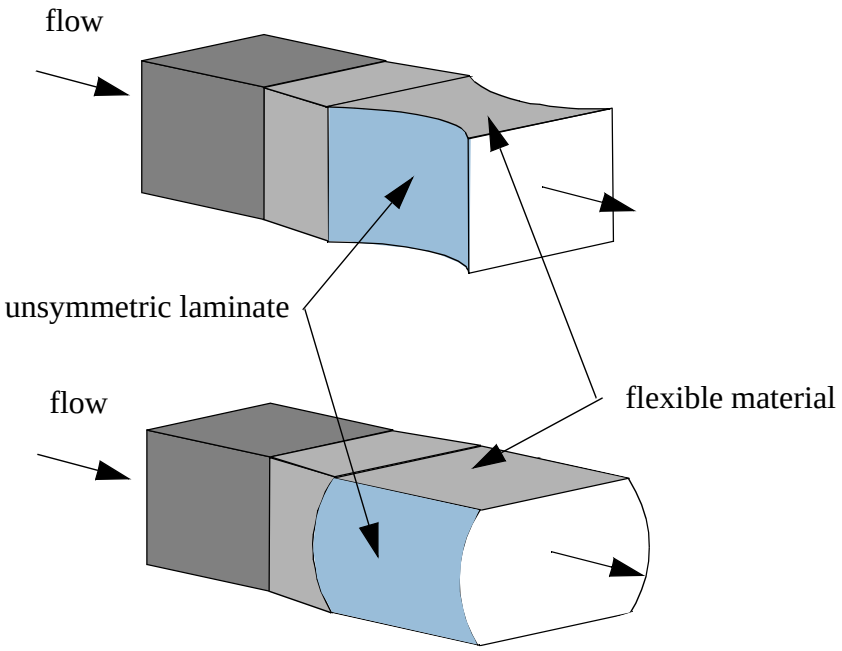

Fig. 1-5. Example of application: Conduit made with cross-ply unsymmetric laminates

1.2 Unsymmetric laminates

Historically, unsymmetric laminates have been mostly used to evaluate the stress-free temperature of a material system, or to evaluate the influence of environmental factors like moisture or temperature on material behavior. For example, Pagano and Hahn [3] used the shape of unsymmetric laminates to determine the stress-free curing temperature. Starting at room temperature, a condition for which unsymmetric laminates exhibit large curvatures, they raised the temperature until the laminates were completely flat, corresponding to curing temperature. Since the curvature of unsymmetric laminates is directly due to thermal residual stresses, Crossman, Mauri, and Warren [4] used the curvature of unsymmetric laminates to study the effects of temperature, humidity, and time on thermal residual stresses. Thus, a change in thermal residual stresses of unsymmetric laminates can be easily quantified by measuring the resulting change in the magnitude of the laminate curvature.

Unsymmetric laminates have also been used by several researchers [5-7] to study the effects of bending-stretching coupling on static deflection, vibration frequencies, and buckling loads of composite plates. In these works classical lamination theory was used to predict the behavior of unsymmetric laminates. Classical lamination theory [8] is a linear theory using the following assumptions:

- the displacements are continuous throughout the laminate
- the Kirchhoff hypothesis is assumed valid
- the strain-displacement relationships are linear
- the material response is linearly elastic
- the through-thickness stresses are small compared to the inplane stresses (the plane stress assumption)

Hyer [9] investigated the shapes of several families of unsymmetric laminates and observed that the room-temperature shapes of unsymmetric laminates do not always conform to the predictions of classical lamination theory. Instead of being a saddle shape, as predicted by the classical theory, many unsymmetric laminates have cylindrical shapes. In addition, a second cylindrical shape can sometimes be obtained by a simple snap-through action, as was discussed in connection with Fig. 1-1. Hyer observed that the deformation occurring during the cooling to room temperature of unsymmetric laminates can cause out-of-plane deflections large enough to violate the assumption of the linear strain-displacement relationships inherent to classical lamination theory. Hyer felt that incorporating geometric nonlinearities into the classical theory was necessary to explain this behavior. To correctly predict the room-temperature shapes of cross-ply laminates, Hyer developed a nonlinear theory [10, 11, 12] based on polynomial approximations to the displacements, extended classical lamination theory to include geometric nonlinearities, and used a Rayleigh-Ritz minimization of total potential energy. In the theory inplane shear strain was assumed to be negligible. Jun and Hong [13] modified Hyer’s theory by

including more terms in the polynomials to account for inplane shear strain. They found that shear strain was indeed negligible for square laminates with very large or small length-to-thickness ratios. However, for intermediate length-to-thickness ratios, shear strain can be significant. Recently, Schlecht, Schulte, and Hyer [14] performed finite-element analyses to calculate the room-temperature shapes of square unsymmetric cross-ply laminates. The finite-element analysis calculations compared very well with the predictions from Hyer's theory.

The various investigations demonstrate that the deformation behavior of unsymmetric laminates with cross-ply lay-ups is now well understood. The behavior of unsymmetric laminates with arbitrary lay-ups, however, is still not fully understood, though there has been work in this area. Dang and Tang [15] modified Hyer's theory to predict the room-temperature shapes of more general unsymmetric laminates. They generalized Hyer's theory by introducing more sophisticated polynomial displacement functions. Approximations of the displacements in the principal curvature coordinate system were used as a starting point. Through coordinate transformation, the displacements in the structural coordinate system were computed. The distinction between the two coordinate systems used for the computation of the displacements is illustrated in Fig. 1-6, the structural coordinates being the *x* and *y* axes aligned with the edges of the laminate. Geometric nonlinearities were considered and a Rayleigh-Ritz approach based on the total potential energy was used to compute shapes. The assumed displacements were not specified correctly and only the sum of two coefficients in the assumed displacement functions could be solved for, as opposed to solving for each coefficient separately. None-the-less, the comparisons with limited experimental data from Hyer [9] were good.

Adopting the same approach, several investigators have proposed different versions of the Dang and Tang theory [15]. Jun and Hong [16] modified Dang and Tang's approximate

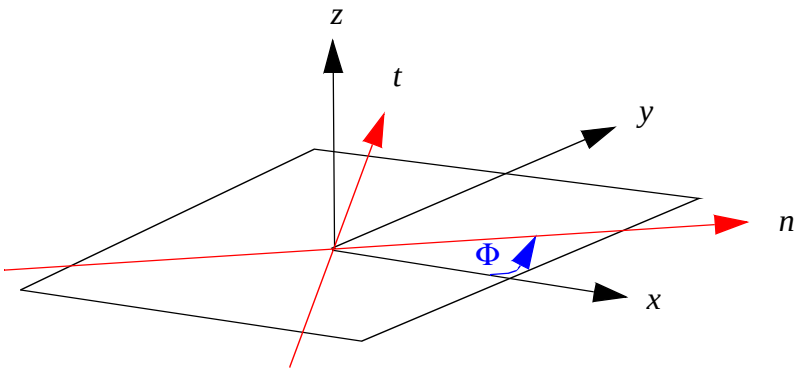

x-y: Structural (laminate) coordinate system
n-t: Principal curvature coordinate system
Φ: Principal curvature direction

Fig. 1-6. Principal curvature and structural coordinate systems

displacement functions by adding more polynomial terms. They obtained fairly complex generalized displacement expressions and used several changes of variables and trigonometric relations to simplify these expressions. The modifications brought to Dang and Tang's theory appeared to affect the predicted shapes for small length-to-thickness ratios. For larger length-to-thickness ratios, the predicted differences were negligible. To validate the theory, a few experimental results for the principal curvature direction from Hyer [9] were presented. No experimental results were presented for the magnitudes of the principal curvatures. Recently, Peeters, Powell, and Warnet [17] developed a theory for square angle-ply laminates based on the work of Jun and Hong [16]. They modified the displacement functions of Jun and Hong by using a more complete set of third-order polynomials. To compute the total potential energy, Peeters, Powell, and Warnet fixed the value for the principal curvature direction, Φ in Fig. 1-6, assuming it was 45^o relative to the laminate edge for all laminates. This assumption is based on classical lamination theory which predicts that angle-ply laminates exhibit equal curvatures in the x and y directions, and therefore have the principal curvature direction equal to 45^o. They arbitrarily forced the elongation strains in the principal curvature coordinate system to be independent of the coordinate variables in a certain fashion. They also treated the laminate as if it was square in the principal curvature coordinate system, the coordinate system which they assumed was oriented 45^o relative to the edge of the square laminate! Experimental results from a single $\pm 30^o$ angle-ply laminate were presented to compare with the theoretical model. The comparison between experiment and predictions was reasonable, but the authors went on to explain how manufacturing problems, material property uncertainties, and material inhomogeneities could have influenced their experimental results. The present work will demonstrate that angle-ply laminates actually do not all have the same principal curvature direction. Rather, the principal curvature direction should be considered as a variable, and not be constrained a priori.

The theories developed so far to predict the shapes of general unsymmetric laminates follow the same approach used originally by Dang and Tang. This approach leads to expressions and procedures for obtaining the strains that seem to be unnecessarily complex. It was felt a theoretical model could be developed using a more straightforward approach and experiments could be conducted on a variety of laminates to compare with the model. Thus one objective of the present work is to develop a theory to predict the temperature-deformation behavior of general unsymmetric laminates as they are cooled from their processing temperature to room temperature. As a check on the theory developed, and to gain additional insight into the behavior of unsymmetric laminates, finite-element calculations using the commercial code ABAQUS are made to study the deformations behavior. Additionally, another objective is to conduct experiments with a variety of laminates to verify the develop theory.

1.3 Shape memory alloys

Since their discovery in the 1950's, SMAs have received increasing interest. These materials, after being plastically deformed, regain their original shape when heated. The strain recovery process is associated with a solid-to-solid martensite phase transformation, which is

activated when the temperature reaches the phase transformation temperature. Plastic strains up to 8% can be recovered by heating the shape memory alloy. In the recovery process, a very large stress can be generated by the SMA. This stress can be used as an actuator force.

The most common alloy to exhibit shape recovery is a nickel-titanium alloy, called Nitinol, for Ni-(Nickel)-Ti-(Titanium)-Nol-(Naval Ordnance Laboratory, which developed it). Nitinol exhibits phenomenal recovery of plastic strains. Moreover, Nitinol exhibits high corrosion resistance and good fatigue behavior. Thus, Nitinol is an excellent mechanical actuator.

The shape-memory effects particular to these materials make SMA suitable to use in many applications. In the medical field [18] SMAs are employed for connecting bones and healing fractures, as well as for orthodontic wires and dental castings. SMAs are also used as switches and grips in robotic and automotive applications [19]. SMAs have been considered in structural applications, such as in an adaptive rotor blade for a helicopter [20] or in a torque box for an aircraft wing [21]. Considering SMAs for such applications implies being able to understand and describe extremely well the mechanics involved in these adaptive structures. Specifically, it is essential to be able to model the deformations induced in the structures by SMA actuators. This requires a very good understanding of the constitutive behavior of SMA. Also, the mechanics involved at the interface between the SMA actuators and the structure have to be clearly understood.

1.3.1 Constitutive models of SMAs

Since the discovery of Nitinol, numerous efforts have been made to explain and describe shape memory behavior. In particular, various constitutive models have been proposed to predict the thermomechanical response of SMAs by several investigators, such as Müller [22], Tanaka [23], Liang and Rogers [24, 25], Brinson [26], Bo and Lagoudas [27], and Boyd and Lagoudas [28].

These different models are composed of two equations which may be coupled. One is a *constitutive equation* relating the stress σ to the strain ε, temperature T, and the martensite fraction, denoted ξ. The second equation is an *evolutionary equation*, also called a kinetics equation, which governs the phase transformation. This equation relates the martensite volume fraction, ξ, to the stress, σ, and the temperature, *T*, in the SMA.

The existing models fall into two categories. They are either *phenomenological* models such as Tanaka's [23], Liang and Rogers' [24, 25] or Brinson's [26] models, or *thermodynamic* models, such as the Bo and Lagoudas' [27] or Boyd and Lagoudas' [28] models.

Phenomenological models

The form of the equations in these phenomenological models are mostly determined from

experimental observations. The one-dimensional constitutive equation obtained from Tanaka's work [23] can be written as

$$\sigma - \sigma_o = D(\xi)(\varepsilon - \varepsilon_o) + \Theta(T - T_o) + \Omega(\xi)(\xi - \xi_o) \tag{1.1}$$

where $D(\xi)$ is the extensional modulus of the SMA material, Θ the thermoelastic tensor and $\Omega(\xi)$ the transformation tensor. The variables with the subscript "o" represent the initial conditions of the SMA. The form of the kinetics equation, $\xi=\xi(\sigma, T)$, governing the phase transformation, may vary from one model to the other. Tanaka [23] expressed the kinetics equation using an exponential function of the form $\xi = \xi(\sigma, T)$. Liang and Rogers [24, 25] modified Tanaka's model by selecting a cosine based kinetics equation. Brinson [26] extended Liang and Rogers' model by including nonconstant material functions and by separating the martensite volume fraction into a thermally-induced part and a stress-induced part. The model developed by Brinson described more adequately the thermomechanical behavior of SMA than the previous models.

Thermodynamic models

Thermodynamic models, such as those by Bo and Lagoudas [27] and Boyd and Lagoudas [28], use a kinetics equation which is derived from the first law of thermodynamics to describe the energy conservation and the second law of thermodynamics to describe the energy dissipation occurring during the phase transformation. The resulting equation is complex and cannot be rearranged to obtain a simple expression of the form $\xi = \xi(\sigma, T)$, similar to the one used by Tanaka, and Liang and Rogers. The constitutive equation is a simple generalized Hooke's law, relating the stress to the strain, temperature, and martensite fraction.

Bo and Lagoudas [27] compared their thermomechanical models with the ones derived by Tanaka, and Liang and Rogers. They showed that the models are related to each other under the theory of thermodynamics. Bo and Lagoudas' model, by using appropriate assumptions, can be simplified to obtain models similar to Tanaka, and Liang and Rogers. Thus, the differences in the existing models come from the assumptions initially used.

Thus it would appear that there are two possible models of SMA that can be used for the present investigation, the Tanaka-based model, or Bo and Lagoudas model. The next section will provide information on which model was chosen for the present investigation.

1.3.2 SMAs in structures

Due to their ability to recover large strains and generate forces, SMAs can be used to advantage in many structural applications. SMAs used as actuators can control the shape of flexible structural systems. Several investigators have studied the interaction of SMA wires attached externally to a simple cantilever beam. This structural system was chosen by a number of investigators because beam theory leads to structural equations that are relatively simple. Also,

SMA wires using as external actuators, as opposed to embedded actuators, simplify the mechanics involved between the actuators and the structure.

Chaudhry and Rogers [29] showed that external SMA actuators were capable of inducing large deflections in beams. Brand, *et al.* [30] and Boller, *et al.* [31] combined Brinson's SMA constitutive model with linear and nonlinear beam theory equations to obtain a model which predicts the deformations induced in the beam as the SMA wire is heated above the phase transformation temperature. Specifically, the model predicts the strains in the beam induced by the SMA actuator as a function of the temperature in the wire. Experiments using known weights to deflect the beam were conducted and confirmed the necessity of using geometrically nonlinear beam theory to predict the deformations when large forces were applied. No experiments were presented to confirm the validity of the SMA-beam model. Xu *et al.* [32] also developed a model predicting the deformations of a beam subjected to external actuators. The major difference between their model and the model used by Brand *et al.* [30] or Boller, *et al.* [31] was in the choice for the SMA constitutive model, as Xu *et al.* used Bo and Lagoudas' SMA model. Using different models should not, however, lead to dramatic changes in the predicted response of the structure. Xu *et al.* also modeled the heat transfer taking place in the wire as the wire was heated resistively by applying voltage. Thus, the model was able to predict the strain in the beam as a function of temperature, electrical current, or time. Finally, Xu *et al.* conducted experiments to validate the developed model. A cantilever beam with externally attached SMA wires was deflected as the wires were heated using electrical current. Using a data acquisition system, they recorded the strains induced in the beam, the force generated by the SMA wire, the wire temperature, and the electrical current. Good correlations were obtained with the model predictions. Since Xu *et al.* have proven experimentally the adequacy of their model to predict accurately the deformations induced by shape memory alloys actuators, their model will be favored in the present work over the other existing model, and will be used to compute the deformations of unsymmetric laminates subjected to SMA actuators.

1.4 Summary of the research objectives

The overall goal of the research, modeling the mechanics involved when using SMA actuators to change the configuration of unsymmetric laminates, is achieved by accomplishing the following specific steps:

- Develop a theory to predict the temperature-deformation behavior of general unsymmetric laminates as they are cooled from curing temperature to room temperature.
- Compare the developed theory with theories developed previously by other investigators.
- Conduct finite-element analyses using the commercial code ABAQUS to obtain additional and more detailed predictions for the room-temperature shapes of unsymmetric laminates.

- Manufacture a variety of unsymmetric laminates, measure their room-temperature shapes, and compare the experimental results with the predictions from the developed theory and ABAQUS.
- Develop a theory to predict the deformation behavior of general unsymmetric laminates to simple applied forces, particularly the snap through which occurs at a certain force level.
- Investigate existing constitutive models for SMAs and select the one which seems the most appropriate for the present study.
- Combine the selected SMA constitutive model with the developed theory so that the deformations induced by SMA actuators on the unsymmetric laminates can be predicted as a function of the temperature in the SMA.
- Attach SMA wires on the laminate surface, measure the SMA-induced deformations in the laminates as a function of the temperature in the SMA wire, and compare the experimental results with the predictions of the model.

1.5 Outline of the document

The theory which was developed to predict the temperature-deformation behavior of general unsymmetric laminates is presented in Chapter 2. This chapter also describes the finite-element computations which were conducted using ABAQUS. Comparisons of the developed theory with previously developed theory are also provided. The procedures to manufacture the laminates and to measure their shapes are described in Chapter 3. Comparisons are established between the experimental measurements and the predictions from the developed theory and from ABAQUS. Chapter 4 presents the theory that was developed to predict the deformation behavior of general unsymmetric laminates to simple applied forces. The mechanics involved as the laminates snap through are discussed in particular. After Chapter 4, attention is focused on SMAs. In Chapter 5, a constitutive model is described and implemented into the theory developed in Chapter 4 to predict the deformations of simple structures to SMA-induced forces. The particular example of a narrow aluminium plate subjected to SMA actuators is modeled and experiments are conducted to validate the model. In Chapter 6, the deformation behavior of unsymmetric laminates due to SMA-induced forces is predicted using the model described in Chapter 5. Chapter 7 presents experiments that were conducted to check the accuracy of the model. Conclusions and suggestions for further research are stated in Chapter 8.

Chapter 2 Deformation behavior of unsymmetric laminates due to a temperature change

This chapter presents the model that has been developed in this study to predict the deformation behavior of general unsymmetric laminates subjected to a temperature change, especially the cooling from the elevated cure temperature to room temperature. The model is based on a geometrically nonlinear structural theory and accounts for the laminate characteristics (stacking sequence, elastic and thermal properties, length, width, and thickness) and the ambient temperature. A Rayleigh-Ritz approach is used to find conditions that render the total potential energy stationary. Accordingly, conditions are sought which make the first variation of the total potential energy zero. Stability of equilibrium is studied by examining the second variation of the total potential energy. The net result is that laminate curvatures are predicted as a function of temperature. To further study unsymmetric laminates and to verify the Rayleigh-Ritz approach, finite-element analyses are conducted using the commercial code ABAQUS. Details on these finite-element computations are presented in this chapter.

2.1 Problem formulation

Consider an unsymmetric laminate of dimension L_x by L_y, as shown in Fig. 2-1. The thickness of the laminate is denoted by H, and the thickness of a single ply by h. Upon cooling to room temperature, the laminate, which was flat at cure temperature, warps out of plane, assuming a cylindrical shape. For example, at room temperature a cross-ply unsymmetric laminate, as in Fig. 1-1, will develop one of the two cylindrical shapes represented in Fig.1-1(b) and Fig. 1-1(c). The laminate can be changed from one shape to the other by a simple snap-through action. Figure 1-1 shows that the laminate exhibits large out-of-plane deflections. In addition, at a given temperature the laminate can have several shapes. Thus, in the study of the laminate deformations, geometric nonlinearities should be incorporated in the analysis by way of the strain-displacement relations. The analysis should also be able to find the multiple solutions, each associated with a different shape. The presence of multiple solutions and geometric nonlinearities implies that the study of the deformation behavior of unsymmetric laminates involves stability issues.

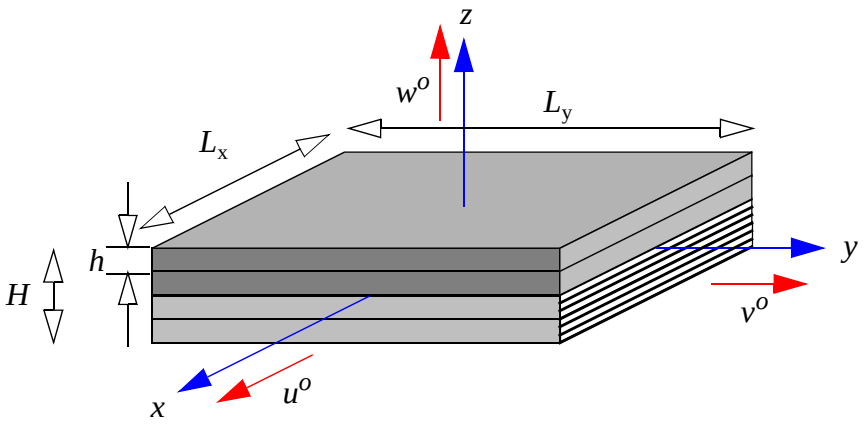

Fig. 2-1. Laminate geometry and coordinate system

The *x*-*y*-*z* laminate coordinate system used to analyze the laminate is shown in Fig. 2-1. The *z*-axis is associated with the out-of-plane direction and the *x* and *y* axes are in the plane of the laminate when it is flat at its cure temperature. The displacements of the midplane surface in the *x*, *y*, *z* directions are, respectively, denoted u^o, v^o, w^o.

2.2 The Rayleigh-Ritz approach

The key in using the Rayleigh-Ritz approach is to obtain good approximations for the displacement functions to be used in the computation of the total potential energy. However, for the present problem these displacement functions are only used to obtain expressions for the strains needed to compute the laminate strain energy. There is no external work term in the total potential energy. Thus, instead of using approximations for the displacements, as other investigators [15-17] have done, the present theory directly uses approximations for the laminate midplane strains, expressed in the laminate coordinate system.

2.2.1 Computation of the total potential energy

Assuming a plane-stress formulation, the total potential energy of the laminate, Π, can be expressed as a function of the material and geometrical properties of the laminate, the applied temperature change, ΔT, and the total strains by,

$$\Pi = \int_{\frac{-L_x}{2}}^{\frac{L_x}{2}} \int_{\frac{-L_y}{2}}^{\frac{L_y}{2}} \int_{-\frac{H}{2}}^{\frac{H}{2}} \left(\frac{1}{2}\overline{Q}_{11}\varepsilon_x^2 + \overline{Q}_{12}\varepsilon_x\varepsilon_y + \overline{Q}_{16}\gamma_{xy}\varepsilon_x + \frac{1}{2}\overline{Q}_{22}\varepsilon_y^2 + \overline{Q}_{26}\gamma_{xy}\varepsilon_y + \frac{1}{2}\overline{Q}_{66}\gamma_{xy}^2 \right.$$
$$- (\overline{Q}_{11}\alpha_x + \overline{Q}_{12}\alpha_y + \overline{Q}_{16}\alpha_{xy})\varepsilon_x \Delta T$$
$$- (\overline{Q}_{12}\alpha_x + \overline{Q}_{22}\alpha_y + \overline{Q}_{26}\alpha_{xy})\varepsilon_y \Delta T$$
$$\left. - (\overline{Q}_{16}\alpha_x + \overline{Q}_{26}\alpha_y + \overline{Q}_{66}\alpha_{xy})\gamma_{xy}\Delta T \right) dx\,dy\,dz, \tag{2.1}$$

where the Q_{ij}'s are the transformed reduced stiffnesses of the individual layers [8] and the total strains ε_x, ε_y, γ_{xy} are given by

$$\varepsilon_x = \varepsilon_x^o + z\kappa_x^o \qquad \varepsilon_y = \varepsilon_y^o + z\kappa_y^o \qquad \gamma_{xy} = \gamma_{xy}^o + z\kappa_{xy}^o. \tag{2.2}$$

The quantities ε_x^o, ε_y^o, γ_{xy}^o and κ_x^o, κ_y^o, κ_{xy}^o are the total midplane strains and curvatures, respectively, defined by

$$\varepsilon_x^o = \frac{\partial u^o}{\partial x} + \frac{1}{2}\left(\frac{\partial w^o}{\partial x}\right)^2 \qquad \varepsilon_y^o = \frac{\partial v^o}{\partial y} + \frac{1}{2}\left(\frac{\partial w^o}{\partial y}\right)^2 \qquad \gamma_{xy}^o = \frac{\partial u^o}{\partial y} + \frac{\partial v^o}{\partial x} + \frac{\partial w^o}{\partial x}\frac{\partial w^o}{\partial y} \tag{2.3}$$

$$\kappa_x^o = -\frac{\partial^2 w^o}{\partial x^2} \qquad \kappa_y^o = -\frac{\partial^2 w^o}{\partial y^2} \qquad \kappa_{xy}^o = -2\frac{\partial^2 w^o}{\partial x \partial y}, \tag{2.4}$$

where it is seen that geometric nonlinearities in the sense of von Karman are included. Here the extensional midplane strains are approximated using the following set of complete polynomials:

$$\varepsilon_x^o = c_{00} + c_{10}x + c_{01}y + c_{20}x^2 + c_{11}xy + c_{02}y^2 + c_{30}x^3 + c_{21}x^2y + c_{12}xy^2 + c_{03}y^3$$
$$\varepsilon_y^o = d_{00} + d_{10}x + d_{01}y + d_{20}x^2 + d_{11}xy + d_{02}y^2 + d_{30}x^3 + d_{21}x^2y + d_{12}xy^2 + d_{03}y^3, \tag{2.5}$$

where the c_{ij}'s and d_{ij}'s are to-be-determined coefficients. The inplane shear strain is more difficult to assume, as it must be consistent with the strains ε_x^o and ε_y^o. To assure consistent strains, the inplane shear strain is determined using the strain-displacement relations. The out-of-plane displacement, w^o, can be easily approximated by

$$w^o(x, y) = \frac{1}{2}(ax^2 + by^2 + cxy), \tag{2.6}$$

where *a, b, c* are to-be-determined coefficients which represent, respectively, the negative of the curvatures in the x and y directions and the negative of the twist curvature, as

$$\kappa_x^o = -\frac{\partial^2 w^o}{\partial x^2} = -a \qquad \kappa_y^o = -\frac{\partial^2 w^o}{\partial y^2} = -b \qquad \kappa_{xy}^o = -2\frac{\partial^2 w^o}{\partial x \partial y} = -c \cdot \tag{2.7}$$

It is seen that the curvatures are predicted to be a constant throughout the laminate. Alternatively, the curvatures *a*, *b*, and *c* can be thought of as average curvatures. The form of w^o(x, y) in eq. (2.6) is felt to represent the out-of-plane displacements for a large percentage, if not all, of the unsymmetric laminates observed.

Using the expressions for the extensional strains ε_x^o and ε_y^o, and the out-of-plane displacement w^o, the inplane displacements u^o and v^o can be determined by integrating the rearranged strain-displacement relations given by

$$\begin{aligned} \frac{\partial u^o}{\partial x} &= \varepsilon_x^o - \frac{1}{2}\left(\frac{\partial w^o}{\partial x}\right)^2 \\ &= c_{00} + c_{10}x + c_{01}y + c_{20}x^2 + c_{11}xy + c_{02}y^2 + \\ &\quad c_{30}x^3 + c_{21}x^2y + c_{12}xy^2 + c_{03}y^3 - \frac{1}{2}\left(ax + \frac{1}{2}cy\right)^2 \cdot \end{aligned} \tag{2.8}$$

and

$$\begin{aligned} \frac{\partial v^o}{\partial y} &= \varepsilon_y^o - \frac{1}{2}\left(\frac{\partial w^o}{\partial y}\right)^2 \\ &= (d_{00} + d_{10}x + d_{01}y + d_{20}x^2 + d_{11}xy) + d_{02}y^2 + \\ &\quad d_{30}x^3 + d_{21}x^2y + d_{12}xy^2 + d_{03}y^3 - \frac{1}{2}\left(by + \frac{1}{2}cx\right)^2 \cdot \end{aligned} \tag{2.9}$$

Integrating eq. (2.8) and (2.9) with respect to x and y leads to

$$\begin{aligned} u^o(x,y) &= c_{00}x + \frac{1}{2}c_{10}x^2 + c_{01}xy + \frac{1}{3}c_{20}x^3 + \frac{1}{2}c_{11}x^2y + c_{o2}xy^2 + \frac{1}{4}c_{30}x^4 + \\ &\quad \frac{1}{3}c_{21}x^3y + \frac{1}{2}c_{12}x^2y^2 + c_{03}xy^3 - \frac{1}{3}\left(\frac{1}{2}a^2\right)x^3 - \frac{1}{2}\left(\frac{1}{2}acx^2y\right) - \frac{1}{8}c^2xy^2 + h(y) \end{aligned} \tag{2.10}$$

and

$$\begin{aligned} v^o(x,y) &= d_{00}y + d_{10}xy + \frac{1}{2}d_{01}y^2 + d_{20}x^2y + \frac{1}{2}d_{11}xy^2 + \frac{1}{3}d_{02}y^3 + d_{30}x^3y + \\ &\quad \frac{1}{2}d_{21}x^2y^2 + \frac{1}{3}d_{12}xy^3 + \frac{1}{4}d_{03}y^4 - \frac{1}{3}\left(\frac{1}{2}b^2\right)y^3 - \frac{1}{2}\left(\frac{1}{2}bcxy^2\right) - \frac{1}{8}c^2x^2y + g(x), \end{aligned} \tag{2.11}$$

where *h(y)* and *g(x)* are a result of partial integration. To have ε_x^o, ε_y^o, γ_{xy}^o each be complete polynomials to order three, *h(y)* and *g(x)* were chosen to be of the following form,

$$\begin{aligned} h(y) &= e_1 y + \frac{1}{2}e_2 y^2 + \frac{1}{3}e_3 y^3 \\ g(x) &= e_6 x + \frac{1}{2}e_4 x^2 + \frac{1}{3}e_5 x^3 \,. \end{aligned} \tag{2.12}$$

In the above e_1, e_2, e_3, e_4, e_5 and e_6 are unknown coefficients. To eliminate rigid body rotation in the *x*-*y* plane, e_6 should be equal to e_1. Therefore the displacements $u^o(x, y)$ and $v^o(x, y)$ can be simply expressed as

$$\begin{aligned} u^o(x,y) &= c_{00}x + e_1 y + c_{01}xy + \frac{1}{2}(c_{10}x^2 + e_2 y^2) + \frac{1}{2}\left(c_{11} - \frac{1}{2}ac\right)x^2 y + \\ &\quad \left(c_{02} - \frac{c^2}{8}\right)xy^2 + \frac{1}{3}\left(c_{02} - \frac{1}{2}a^2\right)x^3 + \frac{1}{3}e_3 y^3 + \frac{1}{2}c_{12}x^2 y^2 + \\ &\quad \frac{1}{2}c_{21}x^3 + xy^3 c_{03} + \frac{1}{4}c_{30}x^4 \end{aligned} \tag{2.13}$$

$$\begin{aligned} v^o(x,y) &= e_1 x + d_{00}y + d_{10}xy + \frac{1}{2}(e_4 x^2 + d_{01}y^2) + \left(d_{20} - \frac{c^2}{8}\right)x^2 y + \\ &\quad \frac{1}{2}\left(d_{11} - \frac{1}{2}bc\right)xy^2 + \frac{1}{3}\left(d_{02} - \frac{1}{2}b^2\right)y^3 + \frac{1}{3}e_5 x^3 + \frac{1}{2}d_{21}x^2 y^2 + \\ &\quad x^3 y d_{30} + \frac{1}{3}d_{12}xy^3 + \frac{1}{4}d_{03}y^4. \end{aligned}$$

The inplane shear strain can then be easily computed by the third strain-displacement relation, namely,

$$\begin{aligned} \gamma_{xy}^o &= \frac{\partial u^o}{\partial y} + \frac{\partial v^o}{\partial x} + \frac{\partial w^o}{\partial x}\frac{\partial w^o}{\partial y} \\ &= 2e_1 + (e_4 + c_{01})x + (e_2 + d_{10})y + \left(ab - \frac{c^2}{4} + 2c_{02} + 2d_{20}\right)xy + \\ &\quad \left(\frac{1}{2}\left(\frac{ac}{2} + c_{11}\right) + e_5\right)x^2 + \left(\frac{1}{2}\left(\frac{bc}{2} + d_{11}\right) + e_3\right)y^2 + \\ &\quad (3c_{03} + d_{21})xy^2 + (3d_{30} + c_{12})x^2 y + \frac{c_{21}}{3}x^3 + \frac{d_{12}}{3}y^3 \,. \end{aligned} \tag{2.14}$$

This procedure insures a consistent set of expressions for the needed midplane strains. None of

the recent investigators [15-17] studying more general unsymmetric laminates appeared to have taken this simple approach. The approximations obtained for the midplane strains use a total of 28 to-be-determined coefficients. Back-substituting the midplane strains and curvatures into the total strains, eq. (2.2), and into the definition of the total potential energy, eq. (2.1), the spatial integrations in the expression for the total potential energy can be conveniently carried out. The final result is an algebraic expression for the total potential energy of the laminate of the form

$$\begin{aligned}\Pi \;=\; \Pi(&\Delta T, a, b, c, c_{00}, c_{10}, c_{01}, c_{20}, c_{11}, c_{02}, c_{30}, c_{21}, c_{12}, c_{03},\\ &d_{00}, d_{10}, d_{01}, d_{20}, d_{11}, d_{02}, d_{30}, d_{21}, d_{12}, d_{03}, e_1, e_2, e_3, e_4, e_5)\,.\end{aligned} \tag{2.15}$$

Obviously, Π is also a function of the laminate material properties and geometry, but here interest centers on the unknown coefficients and the temperature change.

2.2.2 Variation of the total potential energy

As the problem is now posed in eq. (2.15), the variation of the total potential energy is accomplished by allowing variations of the 28 displacement coefficients in eq. (2.15). From the variation of the total potential energy, the first variation, $\delta\Pi$, is obtained and can be expressed as

$$\begin{aligned}\delta\Pi \;&=\; \delta\Pi(a, \delta a, b, \delta b, c, \delta c, c_{ij}, \delta c_{ij}, d_{ij}, \delta d_{ij}, e_k, \delta e_k, \Delta T)\\ &=\; f_a(a, b, c, c_{ij}, d_{ij}, e_k, \Delta T)\delta a + f_b(a, b, c, c_{ij}, d_{ij}, e_k, \Delta T)\delta b +\\ &\quad f_c(a, b, c, c_{ij}, d_{ij}, e_k, \Delta T)\delta c + \sum_{l=0}^{3}\sum_{m=0}^{3-l} f_{c_{lm}}(a, b, c, c_{ij}, d_{ij}, e_k, \Delta T)\delta c_{lm} +\\ &\quad \sum_{l=0}^{3}\sum_{m=0}^{3-l} f_{d_{lm}}(a, b, c, c_{ij}, d_{ij}, e_k, \Delta T)\delta d_{lm} + \sum_{n=1}^{5} f_{e_n}(a, b, c, c_{ij}, d_{ij}, e_k, \Delta T)\delta e_n\end{aligned} \tag{2.16}$$

$$i \;=\; 0, 3 \qquad j \;=\; 0, 3-i \qquad k \;=\; 1, 5$$

Equating the first variation to zero results in 28 equilibrium equations for the laminate. By solving the 25 equations $f_{c_{lm}}=0$, $f_{d_{lm}}=0$, $f_{e_n}=0$, expressions for the 25 coefficients c_{ij}, d_{ij}, and e_k, are obtained as a function of a, b, and c, namely,

$$\begin{aligned} c_{ij} \;&=\; c_{ij}(a, b, c, \Delta T)\\ d_{ij} \;&=\; d_{ij}(a, b, c, \Delta T)\\ e_k \;&=\; e_k(a, b, c, \Delta T)\,.\end{aligned} \tag{2.17}$$

Substituting eq. (2.17) into the remaining equations, $f_a=0$, $f_b=0$, $f_c=0$, leads to a set of 3 nonlinear equations which are functions of the curvatures a, b, c, and the temperature change ΔT. They are

defined by

$$f_a(a, b, c, \Delta T) = 0 \qquad f_b(a, b, c, \Delta T) = 0 \qquad f_c(a, b, c, \Delta T) = 0 \cdot \tag{2.18}$$

Solving these equations as a function of ΔT using the Newton-Raphson technique gives the equilibrium configurations of the laminate as it cools from the flat curing stage. The stability of the equilibrium configurations can be analyzed by studying the second variation of the total potential energy. Alternatively, the Jacobian of f_a, f_b, and f_c needed in the Newton-Raphson technique can be used. Here the latter approach is used and is described next.

2.2.3 Stability analysis

In the computation of the equilibrium solution using the Newton-Raphson technique, the Jacobian of f_a, f_b, and f_c is computed for each temperature increment and is given by

$$J = \begin{bmatrix} \dfrac{\partial f_a}{\partial a} & \dfrac{\partial f_a}{\partial b} & \dfrac{\partial f_a}{\partial c} \\ \dfrac{\partial f_b}{\partial a} & \dfrac{\partial f_b}{\partial b} & \dfrac{\partial f_b}{\partial c} \\ \dfrac{\partial f_c}{\partial a} & \dfrac{\partial f_c}{\partial b} & \dfrac{\partial f_c}{\partial c} \end{bmatrix} . \tag{2.19}$$

The equilibrium solution is stable if and only if the matrix J given by eq. (2.19) is positive definite. By calculating the eigenvalues of the Jacobian matrix, the stability of the equilibrium solution can be assessed. When one eigenvalue is equal to zero or negative, the matrix is not positive definite and the equilibrium solution is unstable.

2.3 Finite-element analyses

Finite-element analyses using ABAQUS were conducted to simulate the cooling of the laminate from cure temperature to room temperature. The objective was to obtain predictions for the laminate deformations using a different approach and be able to compare with the results from the Rayleigh-Ritz theory. Finite-element analyses also provide more detailed results for the laminate deformations. The main difficulty in analyzing the laminate deformation behavior with finite-element analyses is the presence of multiple solutions. Because there are multiple equilibrium configurations, ABAQUS must be coaxed to continue on a particular path to obtain the different shapes at room temperature. To force ABAQUS to follow a particular path, a slight geometrical imperfection was introduced in the initial shape of the laminate. The imperfection, $\delta(x, y)$, was chosen to give the laminate an initial cylindrical shape, and was defined by the

function

$$\delta(x, y) = A(x\cos\beta + y\sin\beta)^2, \tag{2.20}$$

where A is equal to 0.1% of the total laminate thickness H, and β is approximately equal to the principal curvature direction. Without any imperfection ABAQUS usually converged to the unstable shape. With the imperfection, ABAQUS would converge to one of the two stable shapes. Thus, to obtain the three shapes, three series of finite-element calculations were conducted. For each finite-element analysis a mesh of 100 4-nodes-shell elements was used, as shown in Fig. 2-2. Each element had four nodes with five degrees of freedom each. Since free edge conditions were assumed, only the node at the center of the laminate was constrained. Namely, at x=0, y=0,

$$u = v = w = \frac{\partial w}{\partial x} = \frac{\partial w}{\partial y} = 0 \cdot \tag{2.21}$$

A constant temperature change was applied at the nodes. The displacement field and the curvatures κ_x^o, κ_y^o, and κ_{xy}^o of the laminate were computed by ABAQUS at every node.

2.4 Numerical results

The thermally-induced deformation behavior of three families of unsymmetric laminates with stacking sequences $[-\Theta_4/\Theta_4]_T$, $[(90-\Theta)_4/\Theta_4]_T$, and $[(\Theta-90)_4/\Theta_4]_T$ were analyzed. The last family is cross-ply laminates that are rotated in the z-axis of the structural coordinate. The

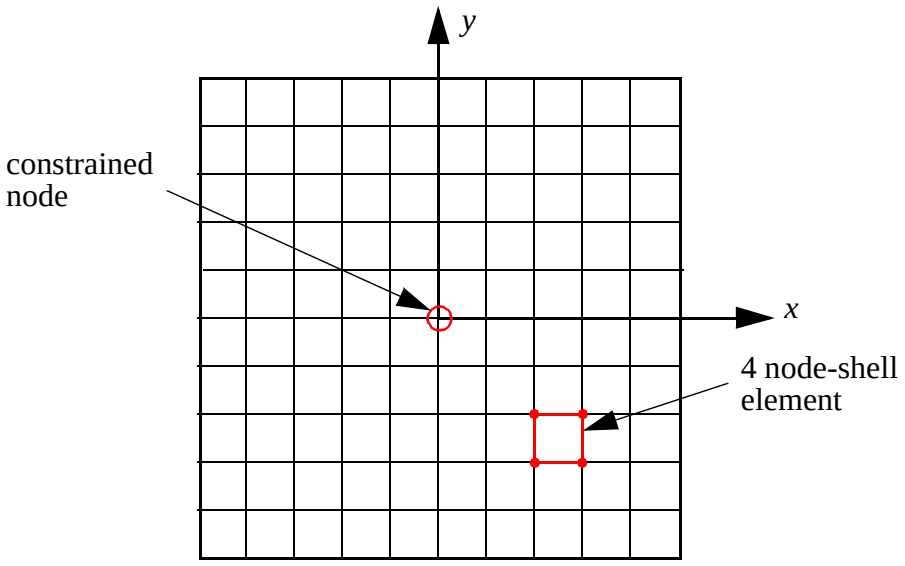

Fig. 2-2. Finite-element mesh for the laminate

particular laminates studied are square, approximately 11.5 by 11.5 in., and made of eight 0.005 in.-thick plies of graphite-epoxy prepreg, resulting in a total thickness H=0.040 in. The material properties of the graphite-epoxy used in the predictions, and the experiments to be discussed later, are assumed to be

$$\begin{aligned} E_1 &= 24.77\times10^6\text{psi} \qquad E_2 = 1.27\times10^6\text{psi} \qquad G_{12} = 1.03\times10^6\text{psi} \\ \nu_{12} &= 0.335 \qquad \alpha_1 = 0.345\times10^{-6}/^{o}\text{F} \qquad \alpha_2 = 15.34\times10^{-6}/^{o}\text{F}\,. \end{aligned} \tag{2.22}$$

2.4.1 Solution procedure used for the developed theory

The set of three equations given by eq. (2.18) was solved to predict the curvatures of the unsymmetric laminates as a function of temperature change, ΔT. Solving the set of equilibrium equations by the Newton-Raphson technique was sometimes difficult, particularly if multiple solutions were expected. Good initial values were required to obtain a meaningful converged solution. The stacking sequences of the laminates studied were chosen judiciously to overcome this difficulty. Each stacking sequence family has at least one value of Θ for which the laminate curvatures are known. At Θ=0, the laminate of the first family is flat, and the laminates of the two other families are cross-ply. For the latter two families, with Θ=0, the shapes could be computed using Hyer's theory [10, 11, 12]. Then, by increasing the value of Θ slightly, the curvatures computed at $\Theta=0^o$ could be used as initial values to solve the equilibrium equations at this increased value of Θ. This procedure was repeated for increasing Θ, using the solution for the previous value of Θ as initial values for the curvatures to solve the new set of equations. To simulate the cooling of the laminate, the equilibrium equations were solved for a temperature change ΔT starting from zero, corresponding to the curing temperature, and decreasing to -280 ^{o}F, corresponding to room temperature. Stability of the predicted solution was checked for each ΔT. With three families of laminates and a range of Θ and ΔT for each family, a number of numerical calculations were required to understand the behavior of the laminates. The symbolic manipulation package *Mathematica*® [33] was used to compute the set of three equations given by eq. (2.18). To solve the set of equations as a function of ΔT and assess the stability of the solutions, a Fortran program was developed.

2.4.2 Finite-element results post-processing

For every finite-element analysis performed, the displacement field and the curvatures κ_x^o, κ_y^o, and κ_{xy}^o of the laminate were computed at every node and at different temperature increments. Counter to the assumption of the developed theory, the curvatures were not constant over the laminate surface, as for the case of a $[60_4/30_4]_T$ laminate illustrated in Fig. 2-3. The largest deviations from being constant occurred at the edges. To be able to compare the values for the curvatures computed by ABAQUS with the curvatures predicted by the developed theory, an average value for value for the finite-element curvatures was obtained by fitting the out-of-plane

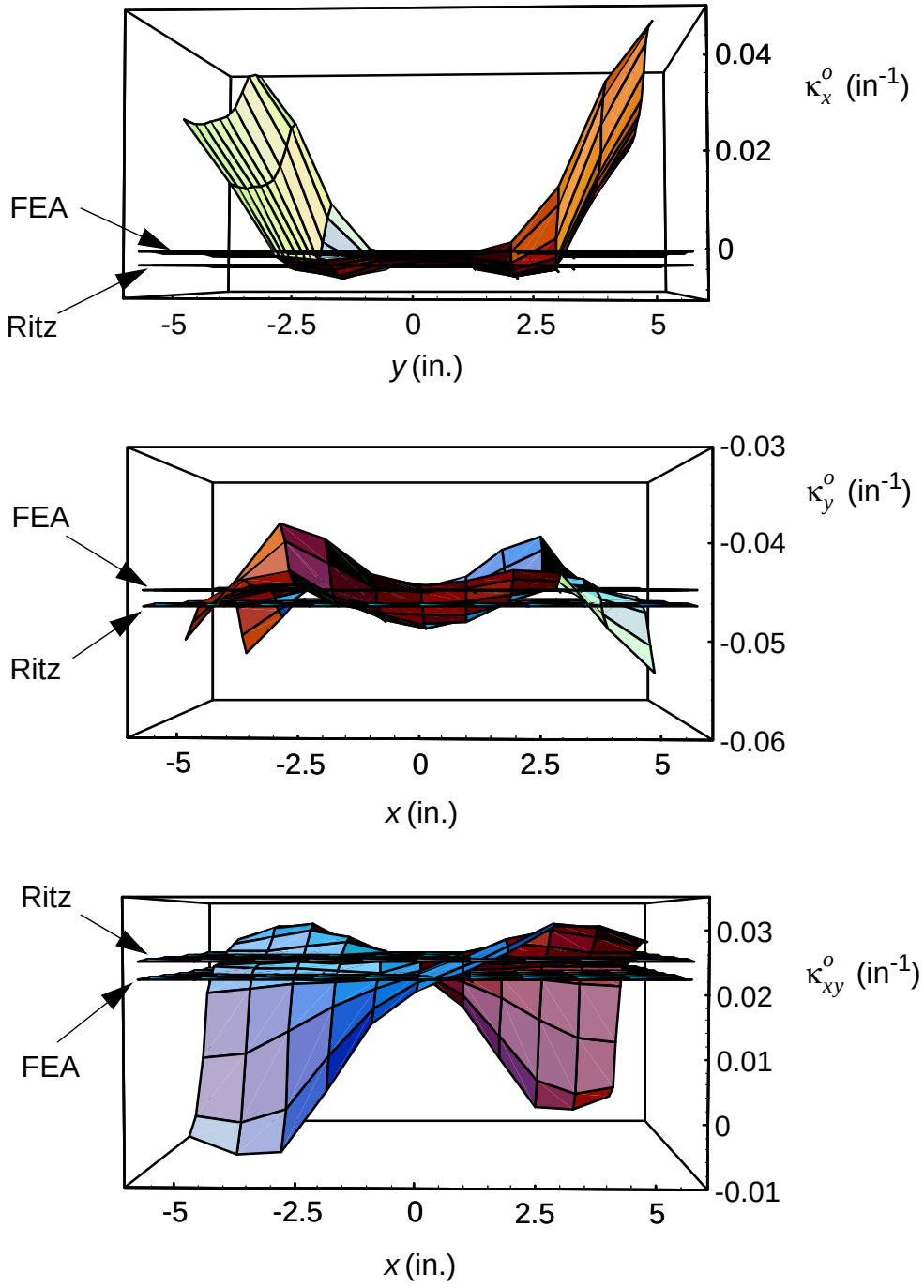

Fig. 2-3. Curvatures of a $[60_4/30_4]_T$ laminate

deflections computed by ABAQUS to an equation of the form

$$w(x, y) = c_1 x^2 + c_2 y^2 + c_3 xy, \tag{2.23}$$

which is identical to the form assumed in eq. (2.6). The average values for the curvatures κ_x^o, κ_y^o, and κ_{xy}^o of the laminate were thus determined by the coefficients c_1, c_2, and c_3. In the case shown in Fig. 2-3, the average curvatures evaluated by using the finite-element results are represented by the planes, labeled FEA, cutting through the three-dimensional surfaces representing the local curvatures. The curvatures predicted by the developed theory are indicated by the planes labeled Ritz. Good correlations can be observed for that particular laminate, and thus the curvatures computed by the developed theory are good estimates for the average curvatures of the laminate.

2.4.3 Predicted curvatures for the three families of unsymmetric laminates

The results from the developed theory obtained for each family are presented in Figs. 2-4 to 2-6 in the form of curvatures, i. e., (-*a*), (-*b*), and (-*c*), vs. ΔT. The curvatures of only two laminates per family are shown so the figures are not cluttered. The average curvatures computed by the finite-element analyses are represented by the diamonds and correspond to the room-temperature shapes of the laminate (ΔT=-280^{o}F). Referring to the figures, at the curing temperature (point A) the curvatures are all zero since the laminate is flat. As the temperature is decreased slightly, some of the curvatures begin to have nonzero values, while other curvatures remain zero.

Considering first the laminates from the $[-\Theta_4/\Theta_4]_T$ family in Fig. 2-4, it is noticed that as the temperature is decreased slightly below the cure temperature, only the twist curvature κ_{xy}^o has a nonzero value. As the temperature is further decreased to point B, the temperature-curvature relations bifurcate. They follow either path BC, path BE, or path BD. With path BC the curvatures in the *x* and *y* directions start increasing with decreasing temperature, while the twist curvature continues to increase but with a higher rate. For Θ=45^o the curvatures κ_x^o and κ_y^o are equal, but for Θ=30^o the curvature κ_x^o is slightly smaller than κ_y^o. This result is in contradiction with the assumption used by Peeters, Powell, and Warnet [17], that states the curvatures κ_x^o and κ_y^o are equal for all square angle-ply laminates. This point will be discussed again later. Path BD is very similar to path BC. The curvatures in the *x* and *y* directions on path BD are equal in magnitude but opposite in sign to the curvatures on path BC. The twist curvature on path BD is exactly the same as the twist curvature on path BC. With path BE the curvatures in the x and y directions remain zero as the laminate is cooled. The twist curvature gradually increases but with a much smaller rate than for the two other paths. The stability analysis shows paths BC and BD are stable. Path BE is unstable and thus the corresponding shape is never observed at room temperature. The average curvatures computed from the finite-element results agree very well with the predictions of the developed theory for the two stable shapes. However for the unstable shape, the finite-element average twist curvature is larger than the predicted twist curvature. The right portion of Fig. 2-4 shows the three equilibrium shapes of the $[-45_4/45_4]_T$ laminate at room temperature (ΔT=-

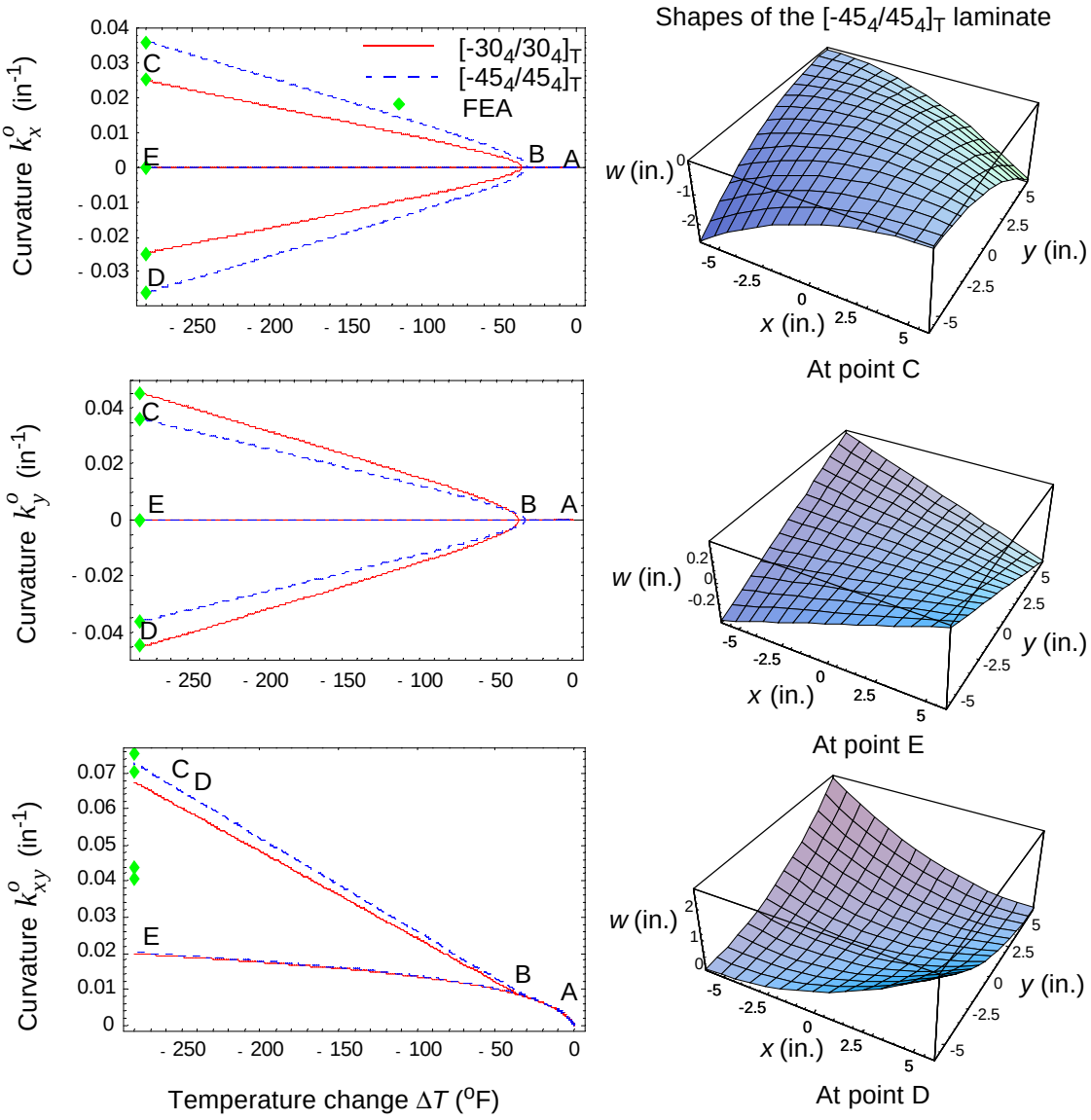

Fig. 2-4. Temperature-curvature relations for $[-\Theta_4/\Theta_4]_T$ laminates

280°F) as predicted by the developed theory. With these shape illustrations, u^o, v^o and w^o are taken to be zero at the geometric center of the laminate. It is important to note the differences in the magnitude of the out-of-plane deflections for the unstable saddle shape compared to the two stable cylindrical shapes.

Considering the graphs obtained for the second family, $[(90-\Theta)_4/\Theta_4]_T$, in Fig. 2-5, as the temperature decreases slightly from curing temperature, the curvatures in the x and y direction take nonzero values. Specifically, κ_x^o is positive and κ_y^o is equal in magnitude to κ_x^o but is

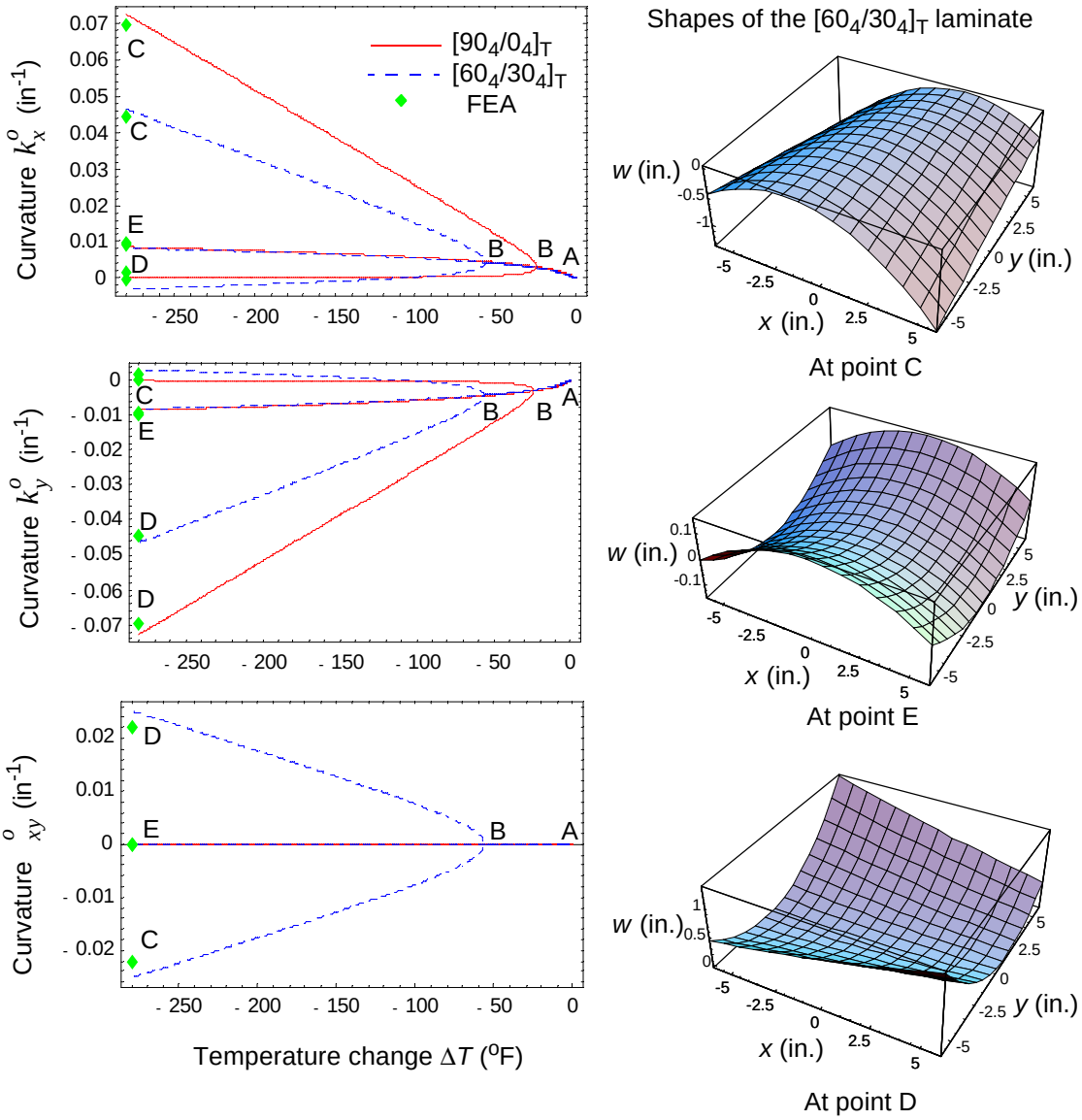

Fig. 2-5. Temperature-curvature relations for $[(90\text{-}\Theta)_4/\Theta_4]_T$ laminates

negative. Since the twist curvature remains equal to zero, the shape of the laminate is a shallow saddle shape. As the temperature is further decreased to point B, the temperature-curvature relations bifurcate into three possible paths, as was observed for the first family. Along path BC curvature κ_x^o increases while curvature κ_y^o decreases, though it was not that large at the bifurcation temperature. At room temperature curvature κ_y^o has virtually disappeared. The twist curvature remains equal to zero down to room temperature for $\Theta=0^o$, as the laminate is a cross-ply, the shape being cylindrical with its curvature in the *x* direction. For $\Theta=30^o$, κ_{xy}^o increases in magnitude along path BC as the temperature is decreased below the bifurcation temperature. The

shape of the laminate corresponding to this path is cylindrical with a large positive curvature in the *x* direction but the generator of the cylinder is rotated by a small angle relative to the *y* axis. With path BD κ_y^o and κ_{xy}^o increase in magnitude with decreasing temperature, while κ_x^o decreases, reaching a value close to zero at room temperature. The shape of the laminate at room temperature is cylindrical with a large negative curvature in the *y* direction equal in magnitude but opposite in sign to the first shape. The generator of this cylinder is rotated slightly relative to the *x* axis. With path BE κ_{xy}^o remains zero but κ_x^o and κ_y^o both increase in magnitude, but they are relatively small, and they are opposite in sign. This corresponds to a saddle shape. The stability analysis shows that paths BC and BD are stable and path BE is unstable. The only two possible shapes at room temperature are thus the two cylindrical ones. The two stable shapes and the unstable one, all at room temperature, are shown in the right portion of Fig. 2-5. The average curvatures computed from the finite-element analyses are slightly smaller, in magnitude, than the ones predicted by the developed theory.

Finally, the cooling of the laminates of the third family, $[(\Theta\text{-}90)_4/\Theta_4]_T$, is illustrated in Fig. 2-6. As the laminate is cooled from curing temperature it begins exhibiting small curvatures in the *x* and *y* directions which are equal in magnitude but opposite in sign, as well as some positive twist curvature. After bifurcation, with path BC κ_x^o increases along with κ_{xy}^o, except for the case of the cross-ply laminate, where $\Theta=0^o$. The curvature κ_y^o is influenced by the value of Θ. For $\Theta=0^o$ the magnitude of κ_y^o decreases to become close to zero for all temperatures. As Θ is increased, curvature κ_y^o increases and takes a positive value. When Θ is 45^o, the stacking sequence of the laminate becomes $[-45_4/45_4]_T$, which is common to the first family. For this case it has been observed that the curvature in the *x* direction is equal to the curvature in the *y* direction. Along path BD in Fig. 2-6, the curvatures κ_x^o and κ_y^o are equal in magnitude to, respectively, the curvatures κ_y^o and κ_x^o of path BC, but are opposite in sign. The twist curvature on path BD is identical to the twist curvature on path BC. With path BE all curvatures show a minimal increase, with curvatures κ_x^o and κ_y^o remaining equal in magnitude and opposite in sign. A stability analysis shows that path BE is unstable, while paths BC and BD are stable. Actually, all laminates studied exhibited two stable cylindrical shapes and one unstable saddle shape at room temperature. These equilibrium configurations are discussed in detail for the three families of laminates in the section to follow.

Good correlations can be observed between the curvatures predicted by the developed theory and the finite-element analyses for the two cylindrical shapes. For the saddle shape however, differences can be noticed between the twist curvature predicted by the finite-element analysis and the developed theory. Reasons for the difference in the twist curvature magnitude for some of the laminate unstable shapes are so far not clear.

2.4.4 Room-temperature shapes for the three families of unsymmetric laminates

To illustrate more clearly how the laminates look at room temperature, contour plots of the function $w^o(x, y)$ were obtained for each laminate of the three families. These plots are

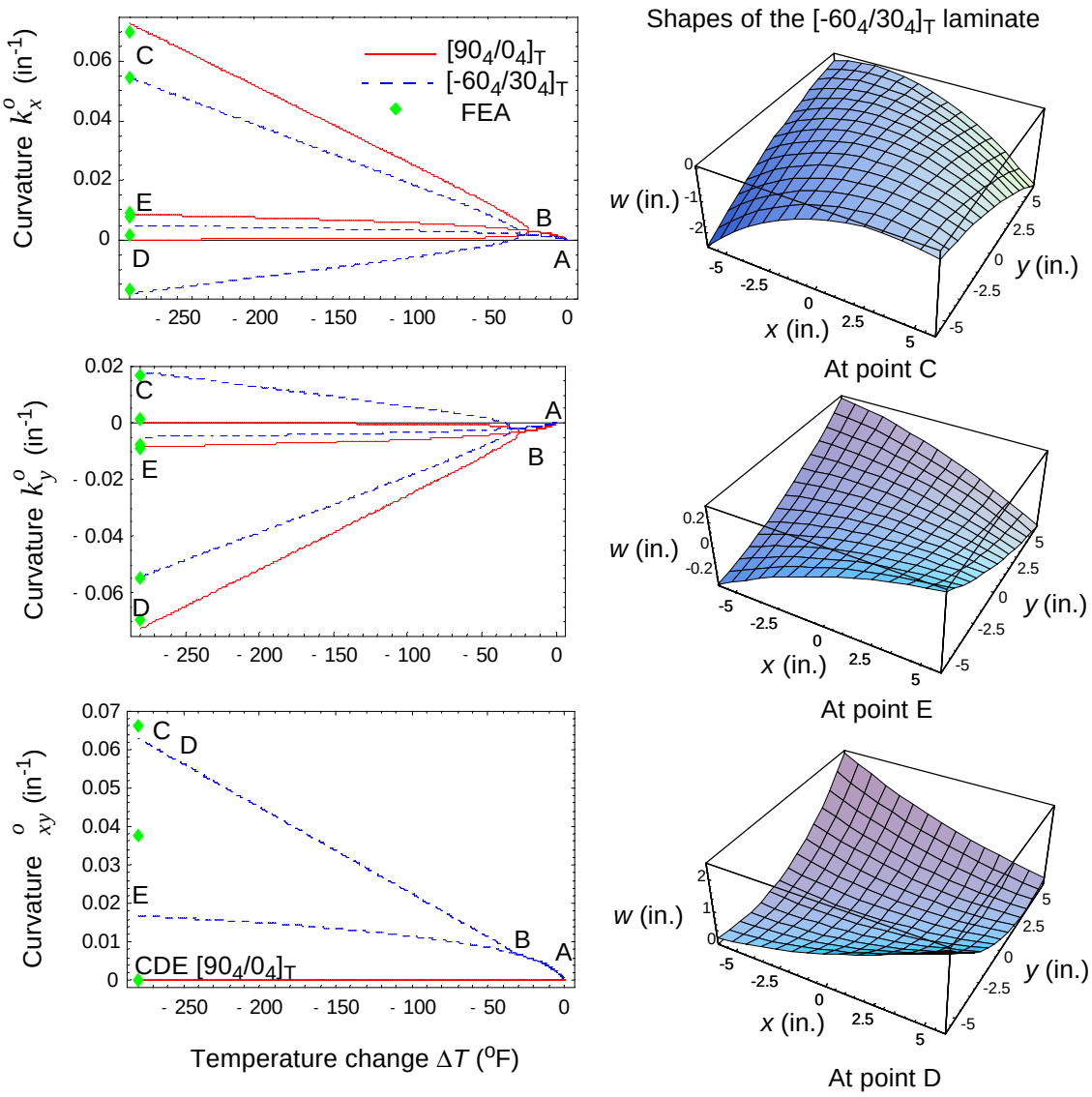

Fig. 2-6. Temperature-curvature relations for [(Θ-90)$_4$/Θ$_4$]$_T$ laminates

represented in Figs. 2-7 to 2-9. In these figures the two stable shapes and the unstable shape, corresponding respectively to point C, D, and E in the previous figures, are depicted. Looking at the contour plots, the darkest areas correspond to the lowest values for $w^o(x, y)$ while the lightest areas correspond to the highest values. In addition the principal curvatures, denoted K_1 and K_2, and the principal curvature direction, denoted Φ, of each shape are indicated in the figures. So far the equilibrium configurations have been described using the curvatures κ_x^o, κ_y^o, and κ_{xy}^o. But it is actually quite difficult to visualize how the laminates look like using these characteristics. It was found more convenient to describe the laminates shapes by using the principal curvatures and principal curvature direction. In the chapters to follow, the use of K_1, K_2, and Φ to describe the

shapes will be favored over κ_x^o, κ_y^o, and κ_{xy}^o. The principal curvatures and principal curvature direction were evaluated from the laminate curvatures κ_x^o, κ_y^o, and κ_{xy}^o, by

$$K_1 = \frac{\kappa_x^o + \kappa_y^o}{2} + \sqrt{\left(\frac{\kappa_x^o - \kappa_y^o}{2}\right)^2 + \left(\frac{\kappa_{xy}^o}{2}\right)^2}$$

$$K_2 = \frac{\kappa_x^o + \kappa_y^o}{2} - \sqrt{\left(\frac{\kappa_x^o - \kappa_y^o}{2}\right)^2 + \left(\frac{\kappa_{xy}^o}{2}\right)^2} \qquad (2.24)$$

$$\Phi = \frac{1}{2}\operatorname{atan}\left(\frac{\kappa_{xy}^o}{\kappa_x^o - \kappa_y^o}\right).$$

To obtain consistent results for all laminates, the principal curvature direction Φ was arbitrary chosen to be associated with the principal curvature which had the largest magnitude. Thus, it was in some cases necessary to add or subtract $\pi/2$ to or from the value of Φ obtained from eq. (2.24).

Considering first the laminates from the $[-\Theta_4/\Theta_4]_T$ family in Fig. 2-7, it is interesting to note that the principal curvatures and principal curvature directions of one stable cylindrical shape are equal in magnitude but opposite in sign to the principal curvatures and principal curvature directions of the second stable cylindrical shape. Of the two principal curvatures of a given cylindrical shape, one is virtually zero while the other increases in magnitude with Θ. On the other hand, for any unstable shape curvatures K_1 and K_2 are equal but opposite in sign. As a result there are two possible values for the principal curvature direction of the unstable saddle, i. e., plus or minus 45^o. It is important to observe that the magnitude of the principal curvature direction for the cylindrical shapes are different from one laminate to the other. Starting at 60^o for $\Theta=15^o$ the magnitude of Φ decreases to 45^o when $\Theta=45^o$. The present results conflict with the assumption used by Peeters, Powell, and Warnet [17] to calculate the shapes of angle-ply laminates. As discussed in Chapter 1, they assumed in their theory that the principal curvature direction Φ was equal to 45^o for all angle-ply laminates. From the present results it seems that their basic assumption is incorrect. This issue will be further discussed in the following chapter where experimental measurements of the laminate shapes will be presented.

Considering the laminates from family $[(90-\Theta)_4/\Theta_4]_T$, Fig. 2-8, again one of the two principal curvatures for the stable shapes is close to zero. The other one decreases with Θ, becoming zero at $\Theta=45^o$, which corresponds to a flat laminate. As with the first family, the principal curvatures for the unstable shapes are equal in magnitude but opposite in sign. This results in two possible values for the principal curvature direction of the unstable saddle, 0^o or -90^o. As can be observed in the contour plots and in the numerical computations, the principal curvature direction of the cylindrical shape corresponding to point C increases in magnitude with Θ, while the principal curvature direction of the cylindrical shape corresponding to point D decreases in magnitude with Θ.

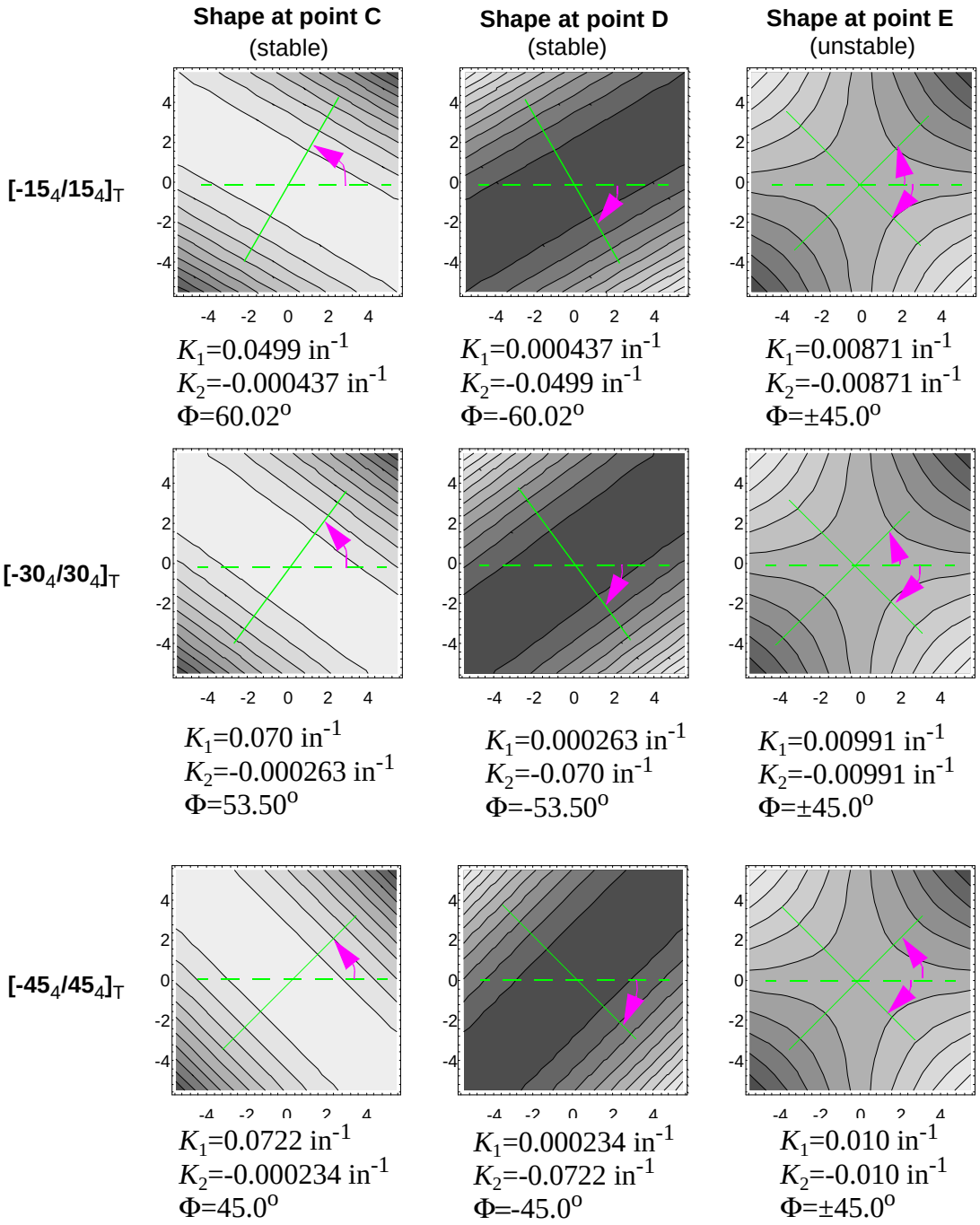

Fig. 2-7. Contour plots of the room-temperature shapes of $[-\Theta_4/\Theta_4]_T$ laminates

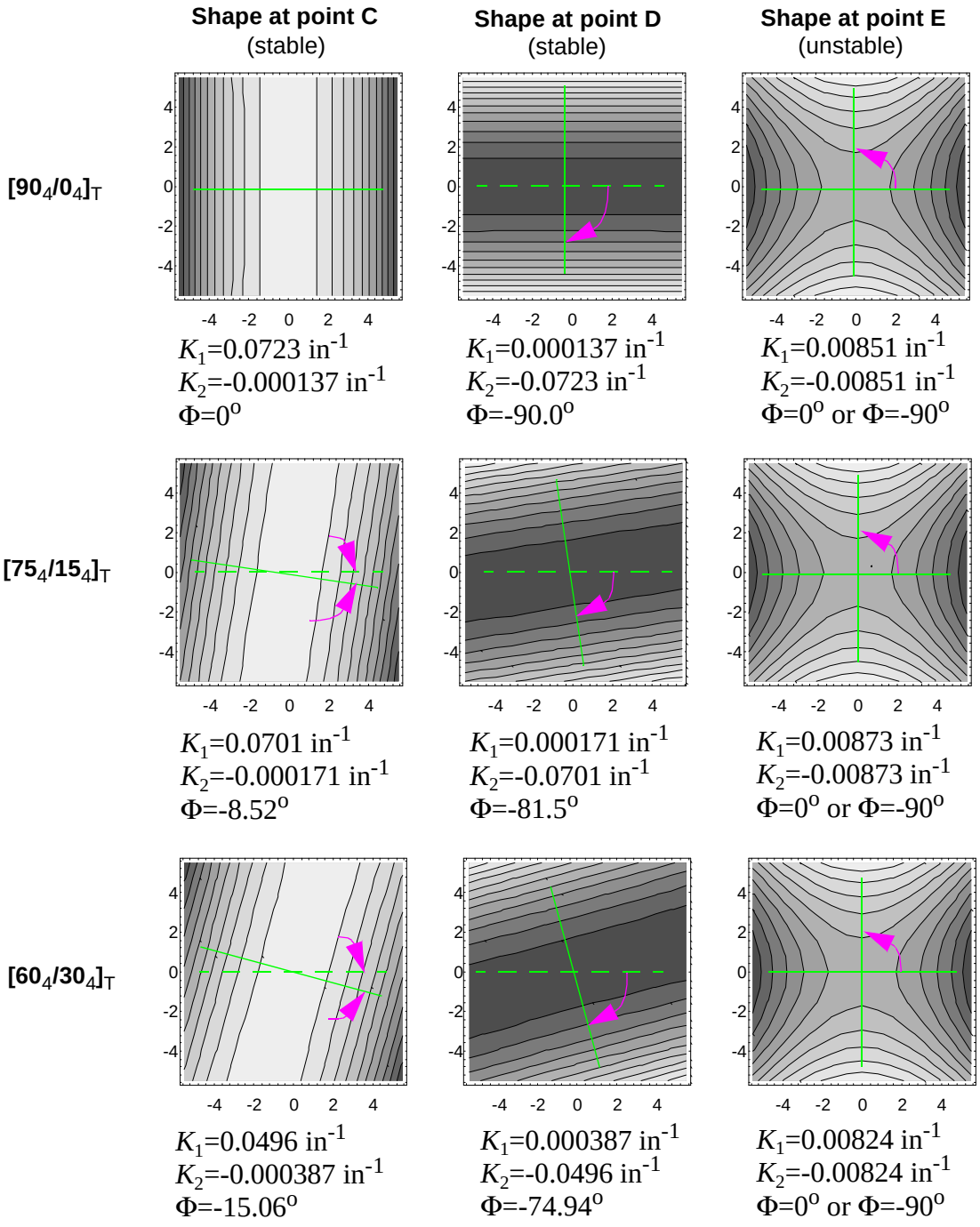

Fig. 2-8. Contour plots of the room-temperature shapes of $[(90\text{-}\Theta)_4/\Theta_4]_T$ laminates

Finally, the contour plots and numerical results for the $[(\Theta\text{-}90)_4/\Theta_4]_T$ family are presented in Fig. 2-9. As observed for the previous families, the principal curvatures for the unstable saddle shape are equal in magnitude and opposite in sign. Thus, two values for the principal curvature direction Φ are possible. Whereas for the first two families the saddle shape was the same for any Θ, it is interesting to note that the saddle shape for this family is rotated by an angle equal to Θ as Θ increases. Concerning the stable cylindrical shapes, while one of the two principal curvatures remains close to zero, the other takes a large value which remains basically unchanged as Θ increases. For Θ=0, the laminate is a cross-ply. The major principal curvature is equal to 0.0723 in^{-1}, and the principal curvature direction is equal to zero. As Θ increases, the laminate becomes a cross-ply rotated in the laminate coordinate system by an angle equal to Θ. The major principal curvature stays close to the curvature of the cross-ply laminate. The principal curvature direction, Φ, is actually equal to Θ or Θ-90 depending on the cylindrical shape considered. It is interesting to note that laminates in this family have the particularity to have the same principal curvature axes for all equilibrium configurations independent of whether the configuration is stable or unstable. This was not observed for the first two families of unsymmetric laminates.

2.5 Remarks on the developed theory

For all the laminates studied, several coefficients in the expressions for the midplane strains appeared to always take zero values. For the midplane extensional strains, c_{10}, c_{01}, c_{30}, c_{12}, c_{21}, c_{03}, and d_{10}, d_{01}, d_{30}, d_{21}, d_{12}, d_{03} were always exactly zero. In the midplane shear strain, coefficients e_2 and e_4 were also zero. Looking at eqs. (2.5) and (2.14), and the Pascal triangle shown in Fig. 2-10, it is seen that the zero-value coefficients correspond to the second and fourth row. It seems that the polynomial for the midplane strains only needs to contain powers in x and y that add to an even number. In fact, then, the present model uses an unnecessary high number of unknown coefficients. From these observations, it seems that approximating the laminate midplane strains by polynomials using only 14 coefficients is sufficient. The midplane strains can thus be expressed as

$$\begin{aligned}
\varepsilon_x^o &= c_{00} + c_{20}x^2 + c_{11}xy + c_{02}y^2 \\
\varepsilon_y^o &= d_{00} + d_{20}x^2 + d_{11}xy + d_{02}y^2 \\
\gamma_{xy}^o &= 2e_1 + \left(ab - \frac{c^2}{4} + 2c_{02} + 2d_{20}\right)xy + \\
&\qquad \left(\frac{1}{2}\left(\frac{ac}{2} + c_{11}\right) + e_3\right)x^2 + \left(\frac{1}{2}\left(\frac{bc}{2} + d_{11}\right) + e_5\right)y^2 .
\end{aligned} \tag{2.25}$$

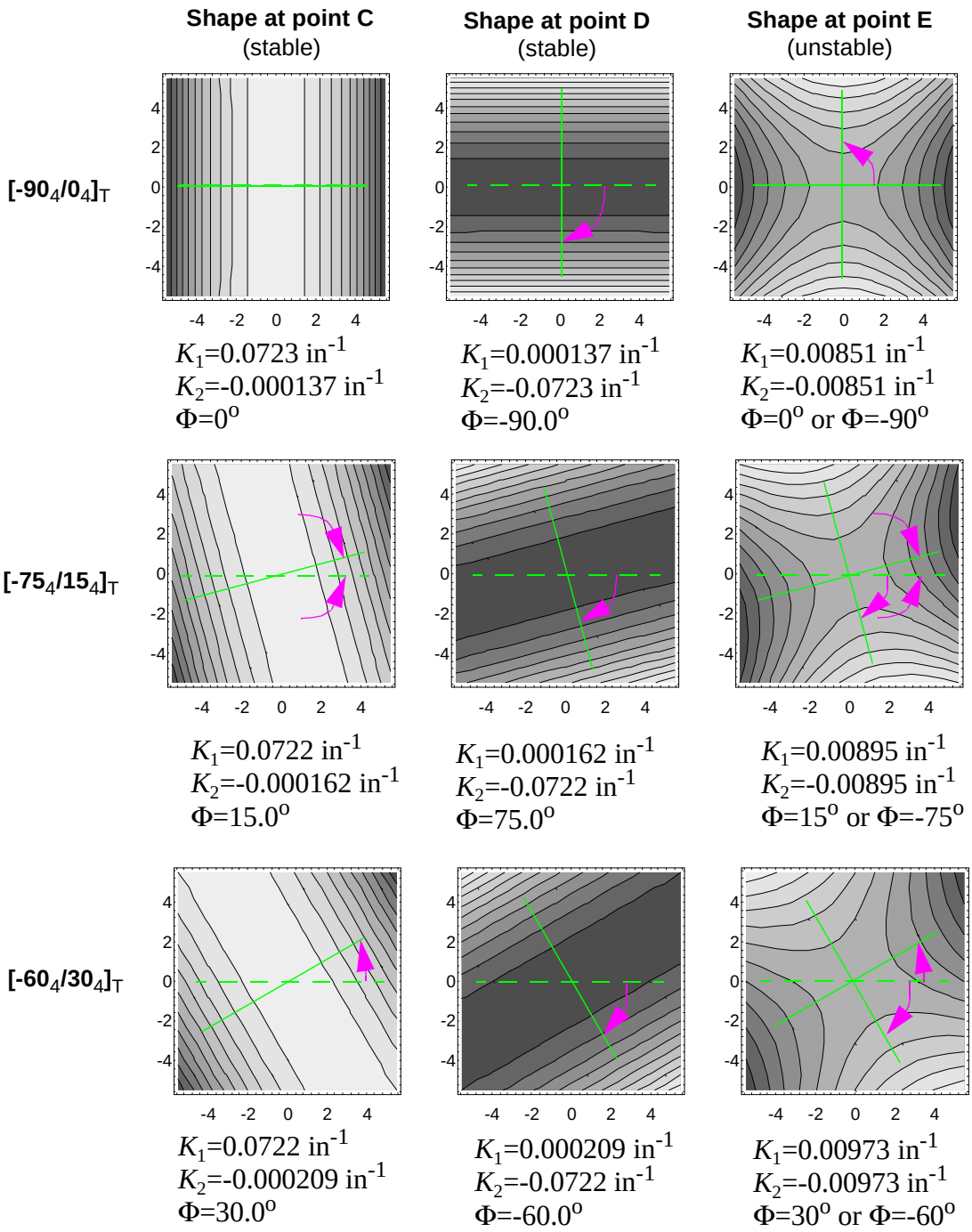

Fig. 2-9. Contour plots of the room-temperature shapes of $[(\Theta\text{-}90)_4/\Theta_4]_T$ laminates

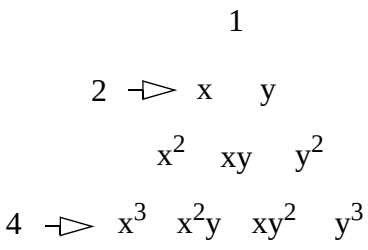

Fig. 2-10. Pascal's triangle

It is interesting to note that the order of these polynomials is the same as the order of the polynomials used by Jun and Hong [16]. However, whereas the above form has 14 independent coefficients, Jun and Hong began their analysis using only 11 independent coefficients in their assumed displacements. They needed only 11 coefficients because they assumed some of the coefficients in $u^o(x, y)$ also appeared in $v^o(x, y)$. In addition, they developed relations among the 11 coefficients by defining combinations of coefficients, thereby reducing the number of independent coefficients to 7. In the present study, based on the numerical values of the 14 coefficients in eq. (2.25), there were no coefficients in $u^o(x, y)$ that were always common to $v^o(x, y)$. For some laminates and temperatures, the coefficients appeared similar, while for other laminates and temperatures the coefficients were quite different. Thus the use of some of the same coefficients in $u^o(x, y)$ and $v^o(x, y)$ would seem to impose an artificial constraint on the problem.

To highlight the effects of having more spatial variables in the expressions for the strains, a comparison between the curvatures predicted by Jun and Hong's theory [16] and the present theory is presented in Fig. 2-11. The curvatures of a 7-in.-square $[0_2/30_2]_T$ unsymmetric laminate were computed using the Jun and Hong theory and the present theory. The diamonds in the figures correspond to results from finite-element analyses. The laminate corresponds to one of the families of unsymmetric laminates Jun and Hong studied in their paper. The material properties used are the same as the ones used in the previous computations. They are given by eq. (2.22). (Note: These are not the properties used by Jun and Hong). Referring to the figure, as with the past cases discussed, upon cooling, the temperature-curvature relations of the laminate bifurcate. Differences exist between the theories in the prediction of the bifurcation temperature. Jun and Hong predict the bifurcation temperature to be about -25^{o}F, whereas the developed theory and the finite-element analysis predict it to be between -40 and -50^{o}F. Although the temperature where the finite-element analysis predicts bifurcation agrees well with the bifurcation temperature predicted by the developed theory, some differences exist around the bifurcation temperature between the curvatures predicted by the finite-element analyses and those predicted by the developed theory. As the temperature is further decreased, the results from the developed theory tend to agree with the results from the finite-element analyses. However, along path BE a slight difference in the curvatures remains. The predictions from the Jun and Hong theory come closer to the developed theory and the finite-element results as the temperature is decreased to room

temperature.

As observed for the laminates presented previously, paths BC and BD are stable and path BE unstable. The laminate exhibits two stable shapes at room temperature, corresponding to point C and point D, but the shapes do not exhibit any kind of symmetry relative to one another. At room temperature the curvatures κ_x^o, κ_y^o, and κ_{xy}^o of one shape are not equal in magnitude to any of the curvatures of the second shape. This is different than the cases considered in Figs. 2.4 to 2.6, where there was an equal but opposite character to the two cylindrical shapes.

The most noticeable differences between the predictions from the Jun and Hong theory and the present theory are around the bifurcation temperature. Differences can also be observed in the prediction of the curvatures for the unstable path, namely path BE. For the two stable shapes at room temperature, however, the two theories agree. Thus, adding more variables in the strains influence the predicted bifurcation temperature as well as the curvatures of one of the three shapes, specifically the unstable shape. The finite-element analyses performed on this laminate show that for temperatures near cure, the present theory seems to give more accurate results than the Jun and Hong theory. Specifically, the Jun and Hong theory does not seem to predict the bifurcation temperature as accurately.

In the chapter to follow, experimental measurements of the shapes of unsymmetric laminates will be described. Also correlations between the experimental results and the predictions from the developed theory and ABAQUS will be presented.

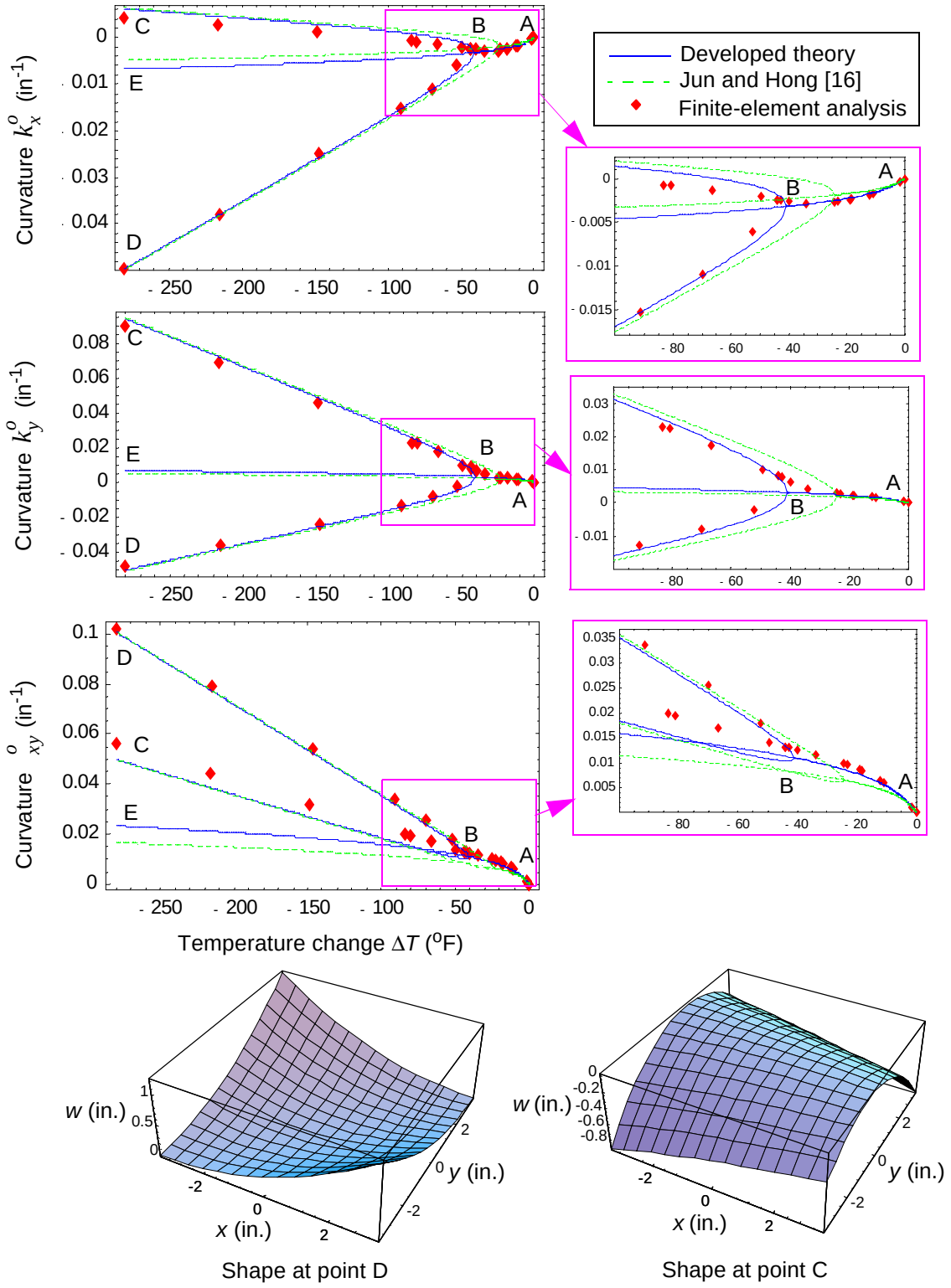

Fig. 2-11. Comparison of the present theory with Jun and Hong [16] theory: Temperature-curvature relations for a $[0_2/30_2]_T$ laminate

Chapter 3 Experimental measurements of the shapes of unsymmetric laminates

To validate the present theory, laminates from the three families, $[-\Theta_4/\Theta_4]_T$, $[(90-\Theta)_4/\Theta_4]_T$, and $[(\Theta-90)_4/\Theta_4]_T$, were manufactured, Θ ranging from 0^o to 45^o in 15^o increments. Due to the stacking sequence chosen for the families, it was not necessary to increase Θ beyond 45^o. With reorientation relative to the laminate coordinate system, the laminates corresponding to Θ between 45^o and 90^o were equivalent to the laminates obtained with Θ between 0^o and 45^o. The laminates were made of 8 plies of Hercules IM7/8551-7A graphite-epoxy preimpregnated material. The material properties of the manufactured laminates were as given by eq. (2.22). The material properties had been determined by measurements on unidirectional specimens (see Dano [1] for details).

3.1 Initial coordinates

The main issue in measuring the shapes of the laminates was to obtain experimental data that could be compared with the predictions of the developed theory. In the developed theory the displacement field is measured using the initially flat laminate as a reference. For example, referring to Fig. 3-1, the displacement functions $u^o(x, y)$, $v^o(x, y)$, and $w^o(x, y)$ measure the displacement, respectively, in the x, y, and z directions of a point P' which was initially at the coordinates (x, y) measured when the laminate was flat, namely point P. Ideally the shape of the laminate, actually the out-of-plane deflection, should be measured from the same reference state as used in the theory. Thus, for out-of-plane deflection measurements it was necessary to know what the initial coordinates of the point were. To achieve this, Kevlar® fibers were laid at one inch intervals to form a reference grid that was used to indicate the initial coordinates of 121 points on the flat uncured laminate surface. The deflections of these points could then be measured and compared with the displacements predicted by the function $w^o(x, y)$ from the theory.

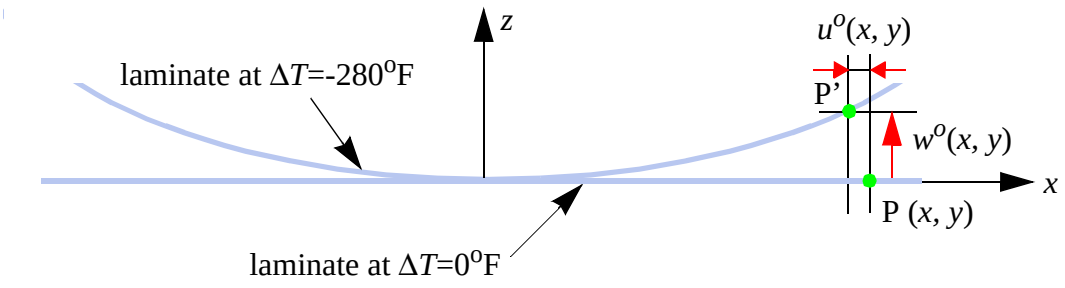

Fig. 3-1. Problem description

3.2 Manufacture of the laminates

A total of 8 laminates were actually manufactured, some of them being used for more than one family. After the 8 plies of graphite-epoxy preimpregnated materials were laid up, the laminate was placed on an aluminium plate slightly larger than the laminate. The Kevlar fibers were laid at one inch intervals across the top surface of the laminate, and were kept in position by taping the ends of the fibers on the aluminium plate, as illustrated in Fig. 3-2. The laminate on the aluminium plate was cured in a hot press at 350°F. After curing, the laminates were flatten between two stiff plates and cut along the four edges to be 11.5 by 11.5 in. square. To ensure that the laminates did not contain any moisture, which would have affected the magnitude of the curvatures, the laminates were kept in an oven at 130°F for a few days. After cooling the laminates to room temperature, the out-of-plane deflections were measured.

3.3 Measurement description

The out-of-plane deflections of each laminate were measured using two different methods. One method consisted of using a simple dial-gage, moved around by hand, to measure the out-of-plane deflections. Another method was used six months later to check these measurements. This time, the out-of-plane deflections as well as the inplane displacements, were measured using a automated shape-measuring instrument.

Two sets of measurements were made for each laminate, each set corresponding to one of the two room-temperature shapes. The deflections were fit to a polynomial equation of the form

$$w(x, y) = c_1 x^2 + c_2 y^2 + c_3 xy + c_4 x + c_5 y + c_6 \cdot \tag{3.1}$$

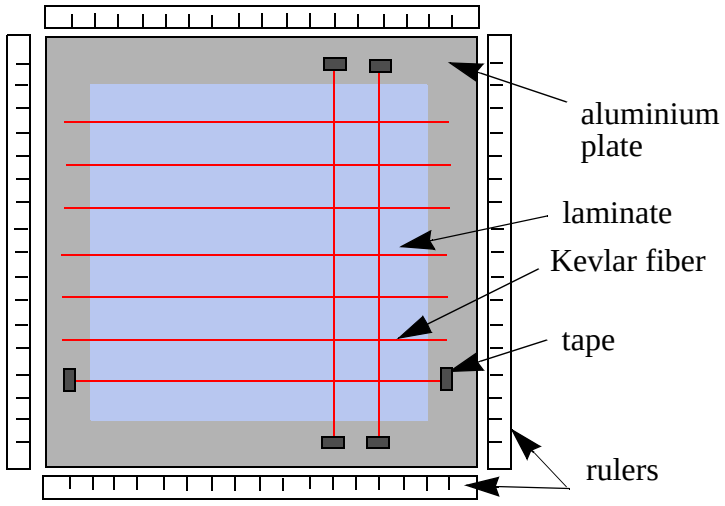

Fig. 3-2. Set-up to lay the Kevlar fibers

The measurements of the 121 points were used in a least-square fit to determine the 6 coefficients of the polynomial. The curvatures κ_x^o, κ_y^o, and κ_{xy}^o of the laminate were determined by the coefficients c_1, c_2, and c_3. The coefficients c_4-c_6 represented rigid body rotations and displacement of the laminate relative to the measurement fixture. From the values of these curvatures, the principal curvatures, K_1 and K_2, and principal curvature directions, Φ, of the laminates were evaluated using the same procedure as the one outlined in section 2.4.4 of Chapter 2. As a result, the principal curvature direction Φ was again always associated with the principal curvature which had the largest magnitude.

3.4 Comparison of the measurements with the predictions

Comparisons were established using the measured principal curvatures and principal directions, as well as using directly the measured out-of-plane deflection of each point.

3.4.1 Principal curvatures and principal curvature directions

The measurements were compared with predictions obtained with the developed theory and ABAQUS. The results obtained for the principal curvatures and principal curvature directions of each family are presented in Figs. 3-3 to 3-5.

Figure 3-3 presents the predicted and measured results for both stable shapes for the $[-\Theta_4/\Theta_4]_T$ family. The measured principal curvatures follow the same trends as the predictions from

the present theory, denoted as Ritz, and from the finite-element analysis, denoted as FEA. Some differences between the magnitudes of the predicted and measured principal curvatures exist. The measured principal curvatures are almost always smaller than the predicted curvatures. It is also interesting to notice that the curvatures measured the second time six months later, and labeled exp 2, are systematically lower that the initial measurements, which are labeled exp 1. The measured principal curvature directions agree very well with the present analysis and the finite-element analysis. As already mentioned in Chapter 2, it is obvious from the measurements and the predictions that the principal curvature direction is different for every angle-ply laminate. It is equal to 45^o only for the $[-45_4/45_4]_T$ laminate. Thus, the assumption used by Peeters, Powell, and Warnet [17] to calculate the shapes of angle-ply laminates is incorrect. The principal curvature direction for angle-ply laminates should be considered as a variable and, not be constrained a priori.

For the $[(90\text{-}\Theta)_4/\Theta_4]_T$ family, good correlation is established between the predictions and the experimental data measured the first time, as illustrated in Fig. 3-4. The curvatures measured during the second experiment do not correlate as well. The measurements for the principal curvature direction correlate fairly well with the predictions.

Finally, the results for the $[(\Theta–90)_4/\Theta_4]_T$ family are presented in Fig. 3-5. The correlations between the present theory, the finite-element analysis, and the first experimental results are good. The curvatures measured during the second experiment are, as observed previously, smaller.

3.4.2 Comparisons of the overall shapes

As mentioned, the measured curvatures in Figs. 3-3 to 3-5 were evaluated using a function fit with the out-of-plane displacements. It is of valuable to directly compare the out-of-plane displacement measurements with the displacements $w^o(x, y)$ computed by the theory. For each laminate, using *Mathematica* [33], a three-dimensional surface plot was created directly from the measured out-of-plane deflection data. This surface plot was superposed on a three-dimensional representation of the function $w^o(x, y)$ using predicted values of a, b, and c. An additional three-dimensional plot representing the out-of-plane deflection computed by ABAQUS was added in the figures to compare further the measurements with the predictions. The results for a few laminates are shown in Figs. 3-6 to 3-9. In the figures the scale chosen exaggerates the out-of-plane deflections so the surface shapes are not representative of the actual shapes. Also, the breakup of the surface grid in the figures is due to the slight overlap of the surfaces in certain regions.

Figure 3-6 represents the out-of-plane deflection for the cross-ply $[90_4/0_4]_T$ laminate. The predictions by the present theory correlate very well with the deflections measured during the first experiment. Some differences in the magnitude can be noted at the edges. The deflections measured six months later are lower, as noted previously. Reasons for these differences are not

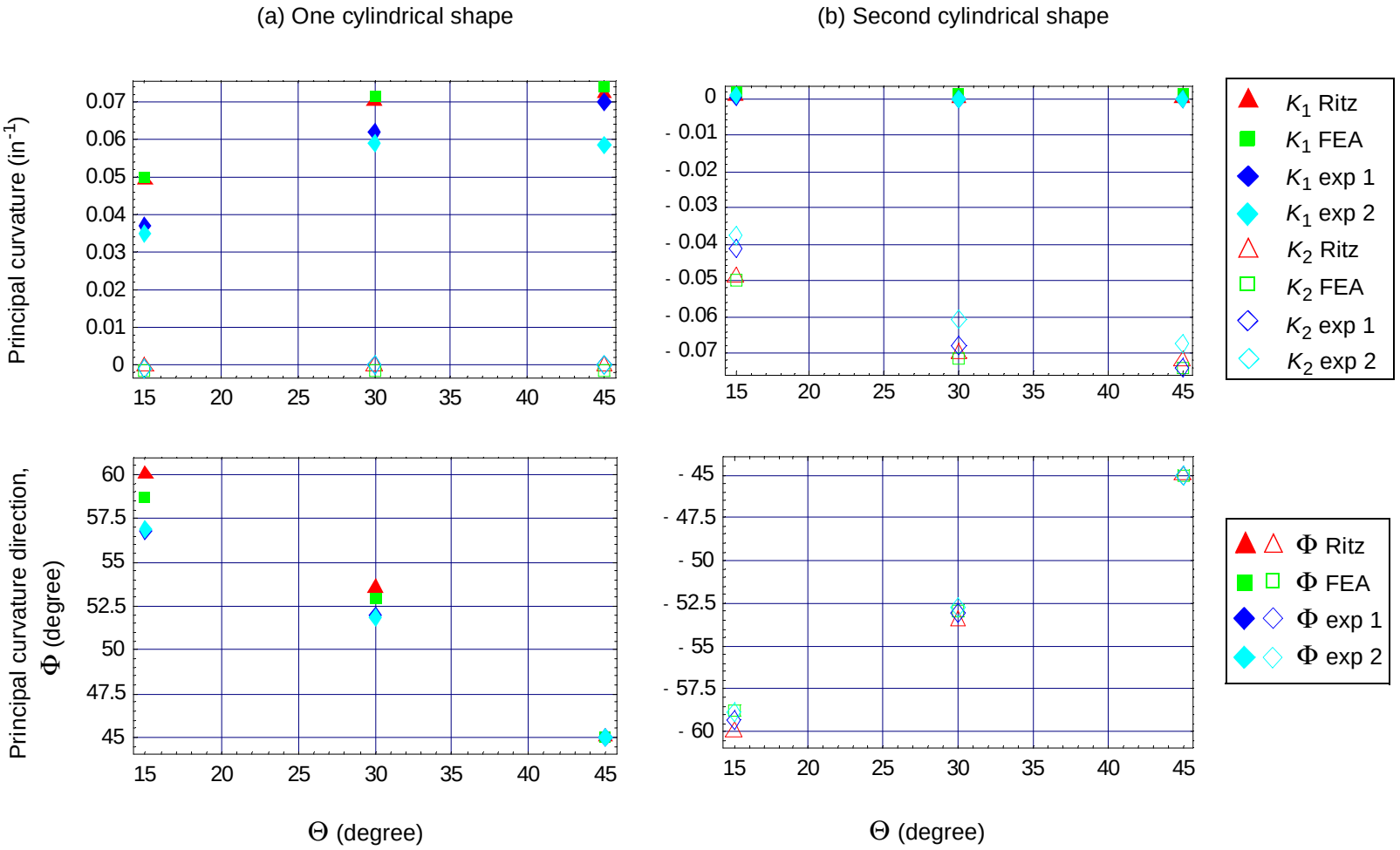

Fig. 3-3. Comparisons between predictions and experiments for $[-\Theta_4/\Theta_4]_T$ laminates

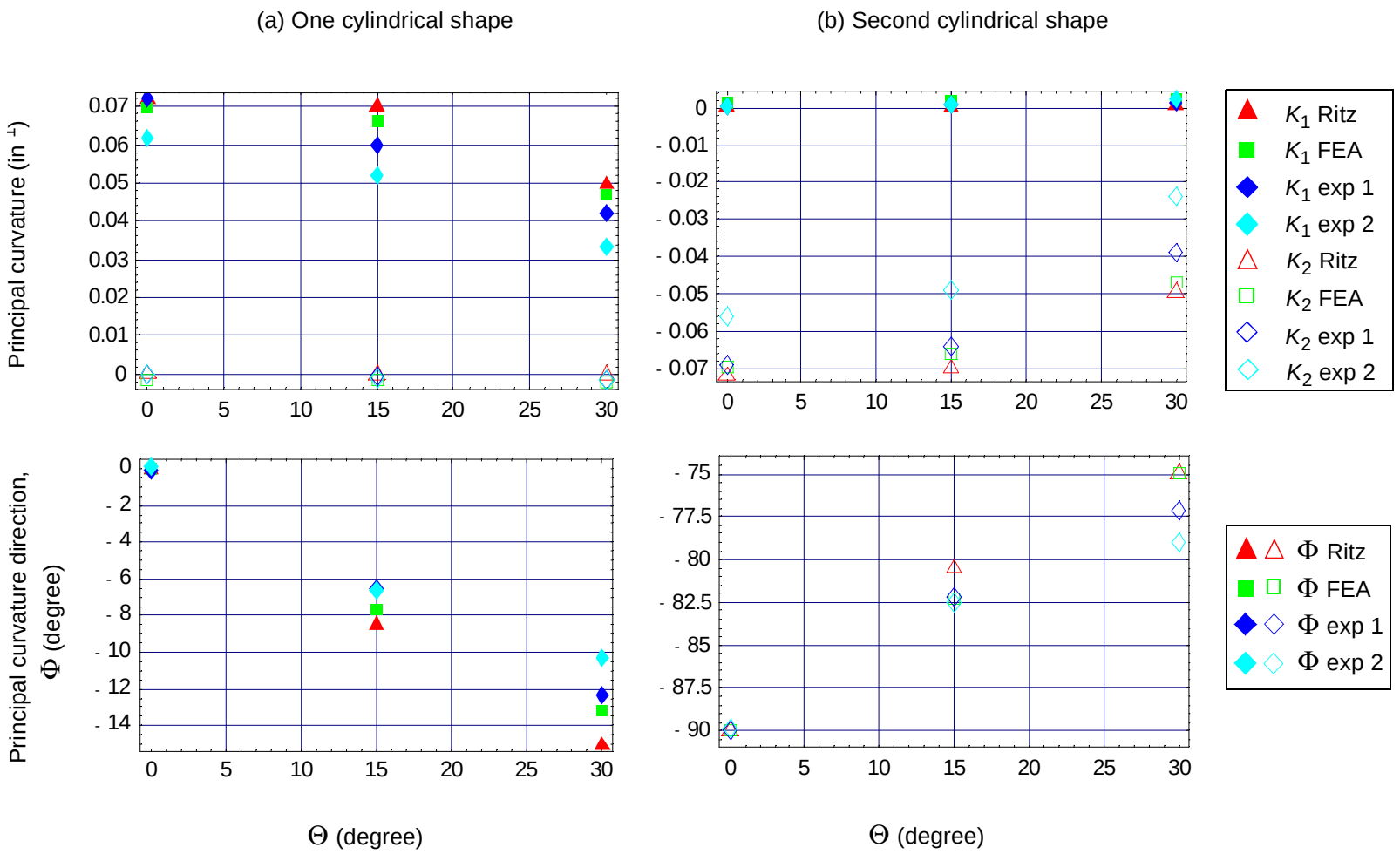

Fig. 3-4. Comparisons between predictions and experiments for $[(90\text{-}\Theta)_4/\Theta_4]_T$ laminates

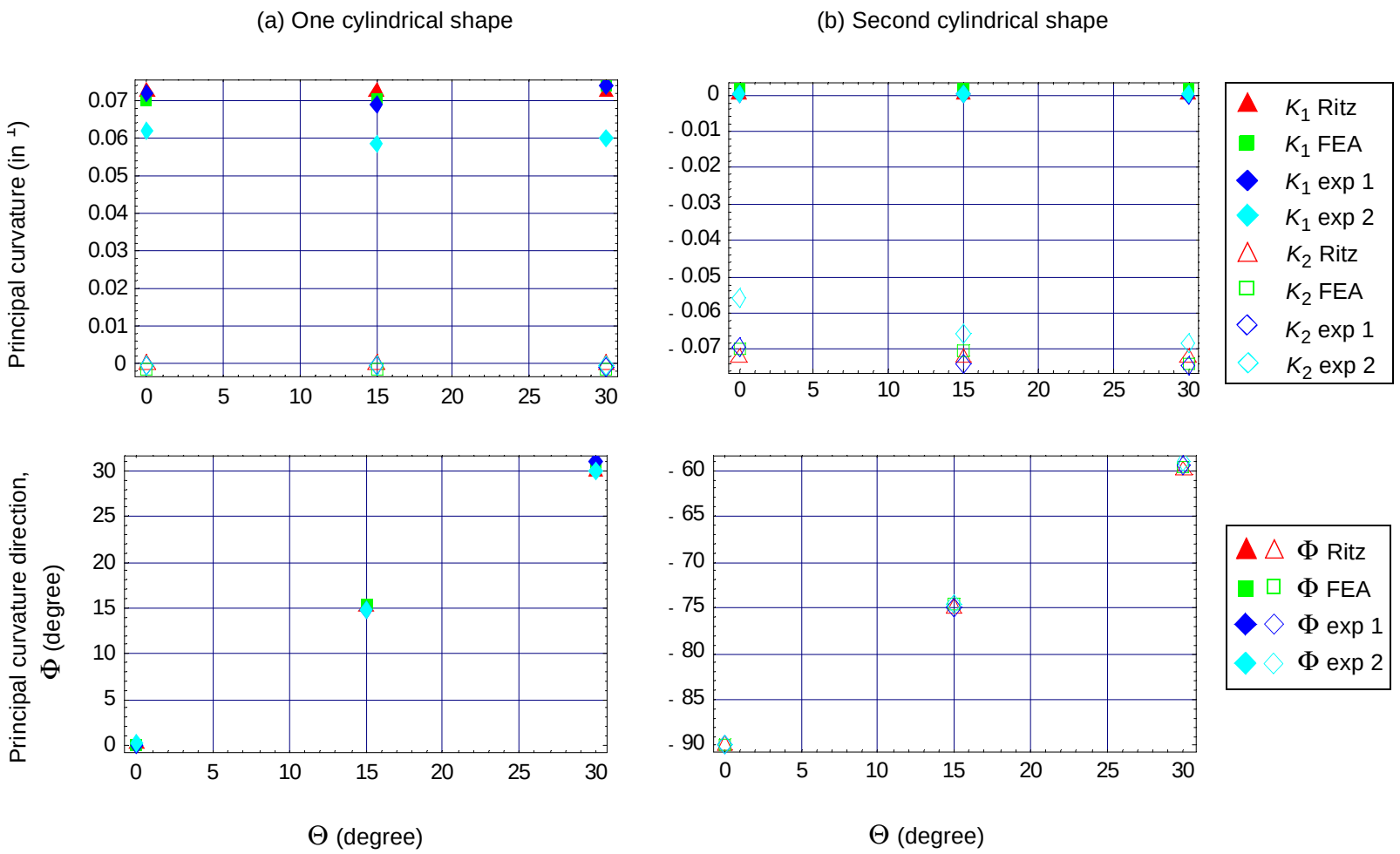

Fig. 3-5. Comparisons between predictions and experiments for $[(\Theta\text{-}90)_4/\Theta_4]_T$ laminates

obvious. It may be possible that relaxation of the epoxy matrix occurred during the elapsed time, leading to a decrease in the laminate curvatures.

The predicted and measured out-of-plane deflections for the $[-30_4/30_4]_T$ laminate are presented in Fig. 3-7. In this and the following figures, the results from the second experiment are not presented. The theory predicts very well the out-of-plane deflections of the laminate. It is actually difficult to distinguish between the different surfaces. The surface plots for the $[60_4/30_4]_T$ laminate are presented in Fig. 3-8. Some differences between the measured and predicted out-of-plane deflections can be noticed at the edges. Figure 3-9 represents the out-of-plane deflections of the $[-30_4/60_4]_T$ laminate. Good correlations are observed between the predictions and the measurements.

Figures 3-10 to 3-12 compare the photographs of a few laminates with the shapes predicted by the theory. The predicted shapes were oriented to obtain a view similar to the ones shown in the photographs. The shapes predicted by the theory exhibit the same characteristics as the ones shown in the photographs. From all the results presented in this Chapter, it is obvious that the developed theory is successful in characterizing the shapes of general unsymmetric laminates. Also the key assumption of Peeters, Powell, and Warnet [17] has been shown to be incorrect.

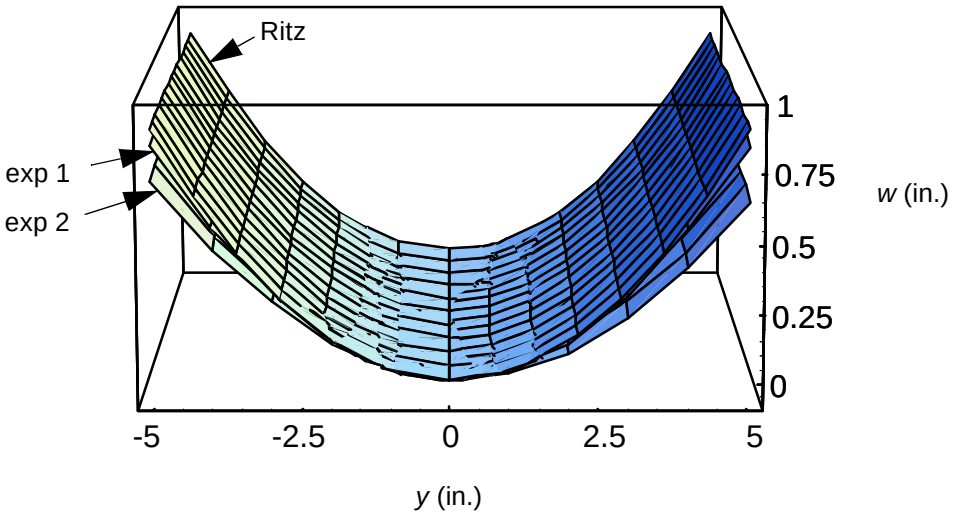

Fig. 3-6. Predicted and measured out-of-plane deflections for the $[90_4/0_4]_T$ laminate

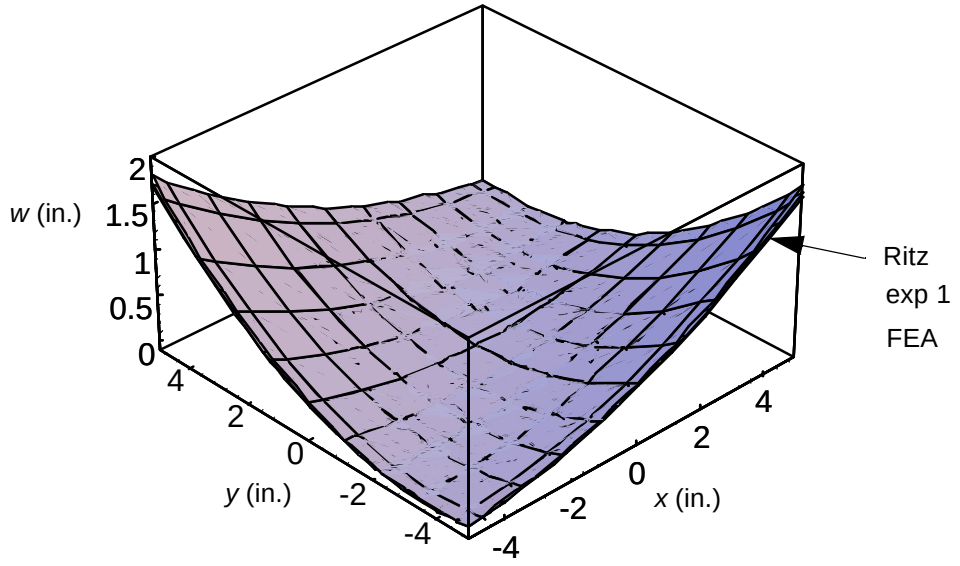

Fig. 3-7. Predicted and measured out-of-plane deflections for the $[-30_4/30_4]_T$ laminate

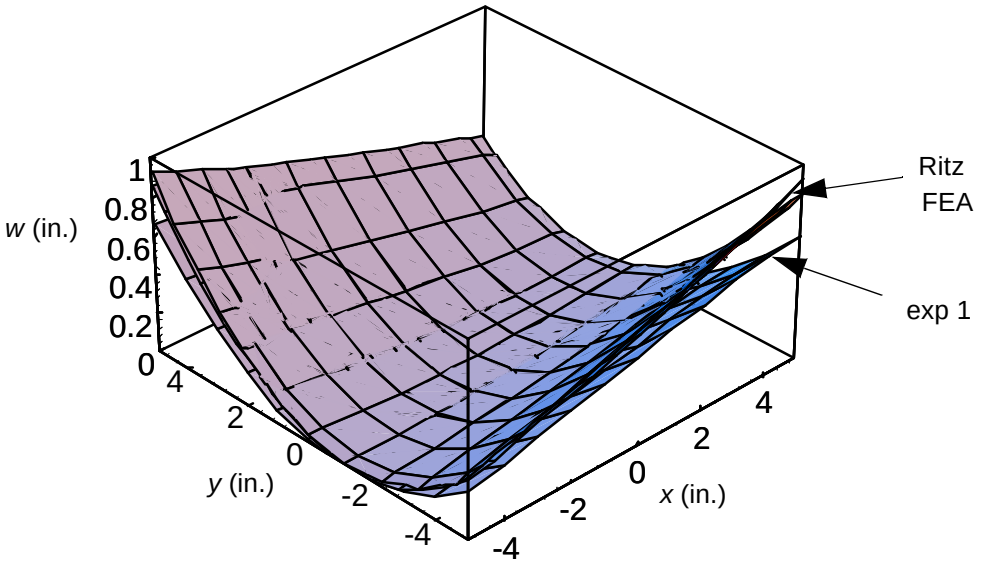

Fig. 3-8. Predicted and measured out-of-plane deflections for the $[60_4/30_4]_T$ laminate

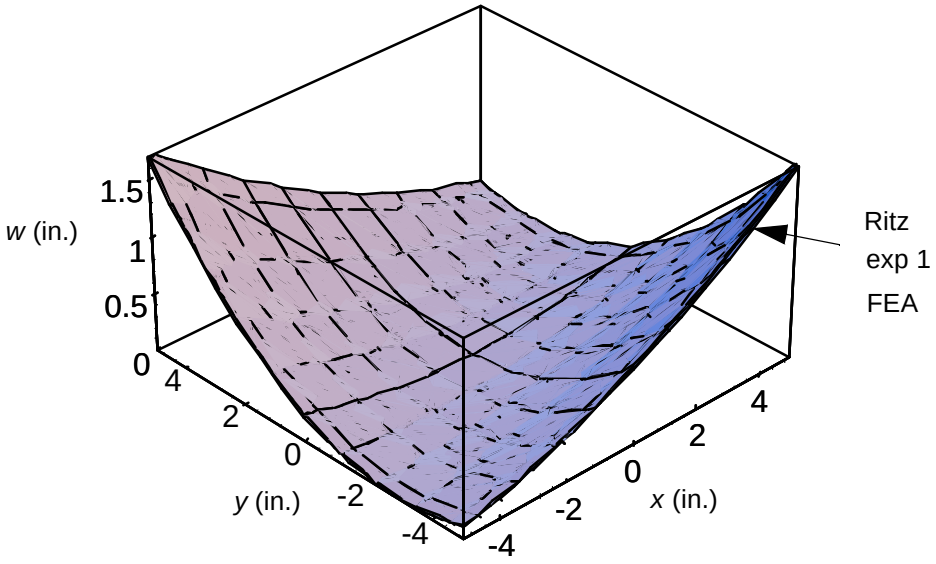

Fig. 3-9. Predicted and measured out-of-plane deflections for the $[-60_4/30_4]_T$ laminate

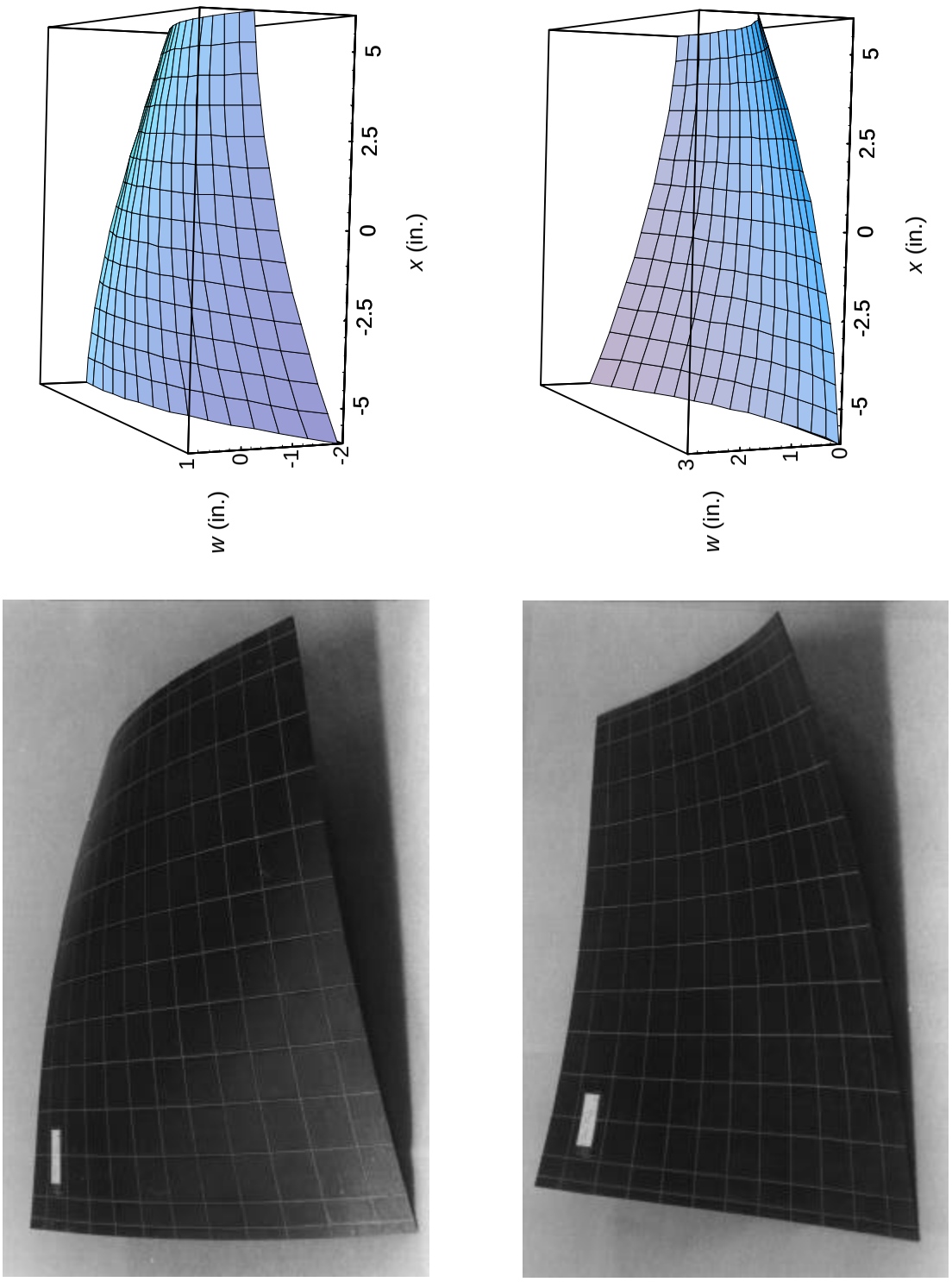

Fig. 3-10. Predicted and actual shapes of the $[-30_4/30_4]_T$ laminate

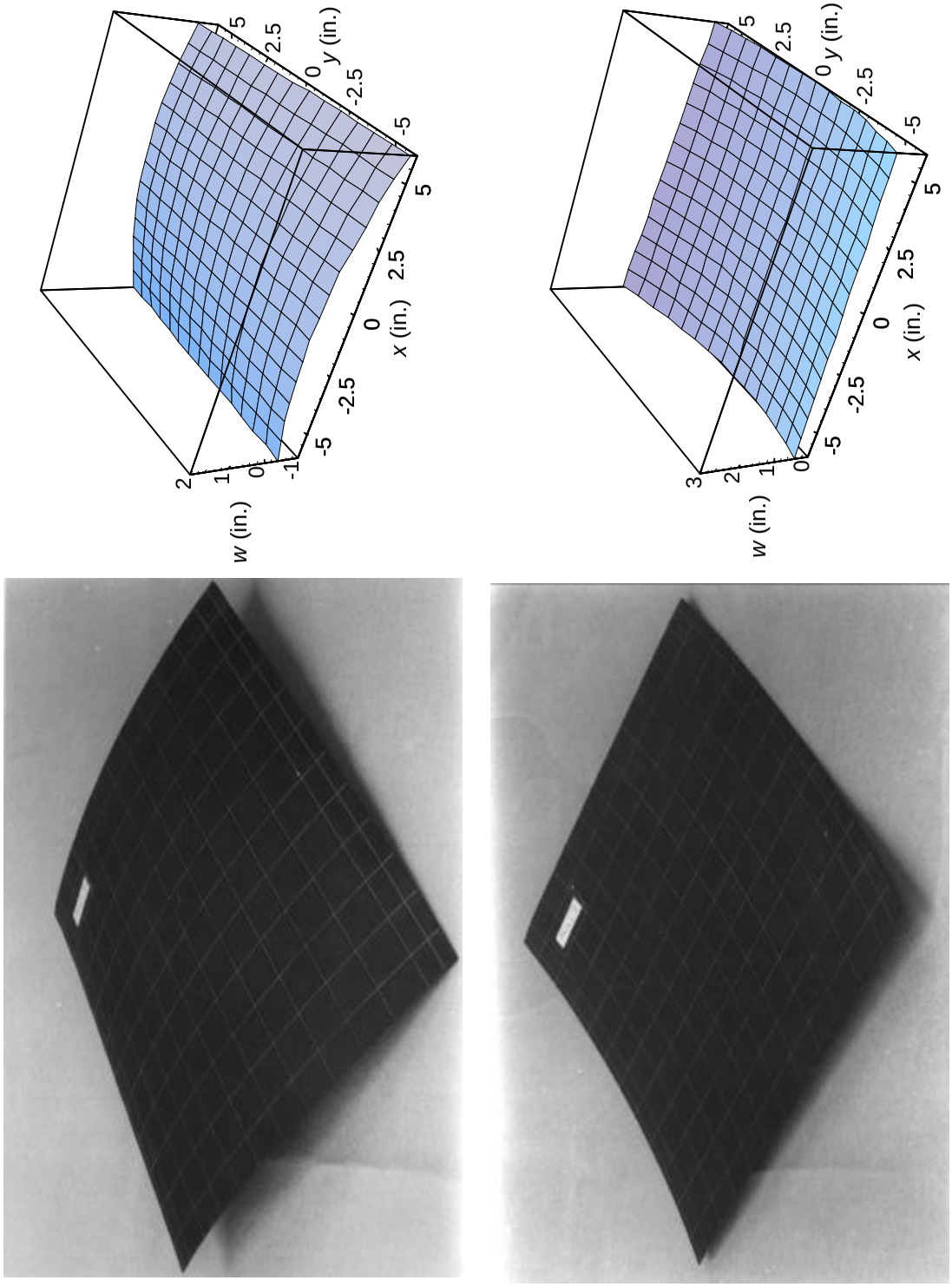

Fig. 3-11. Predicted and actual shapes of the $[60_4/30_4]_T$ laminate

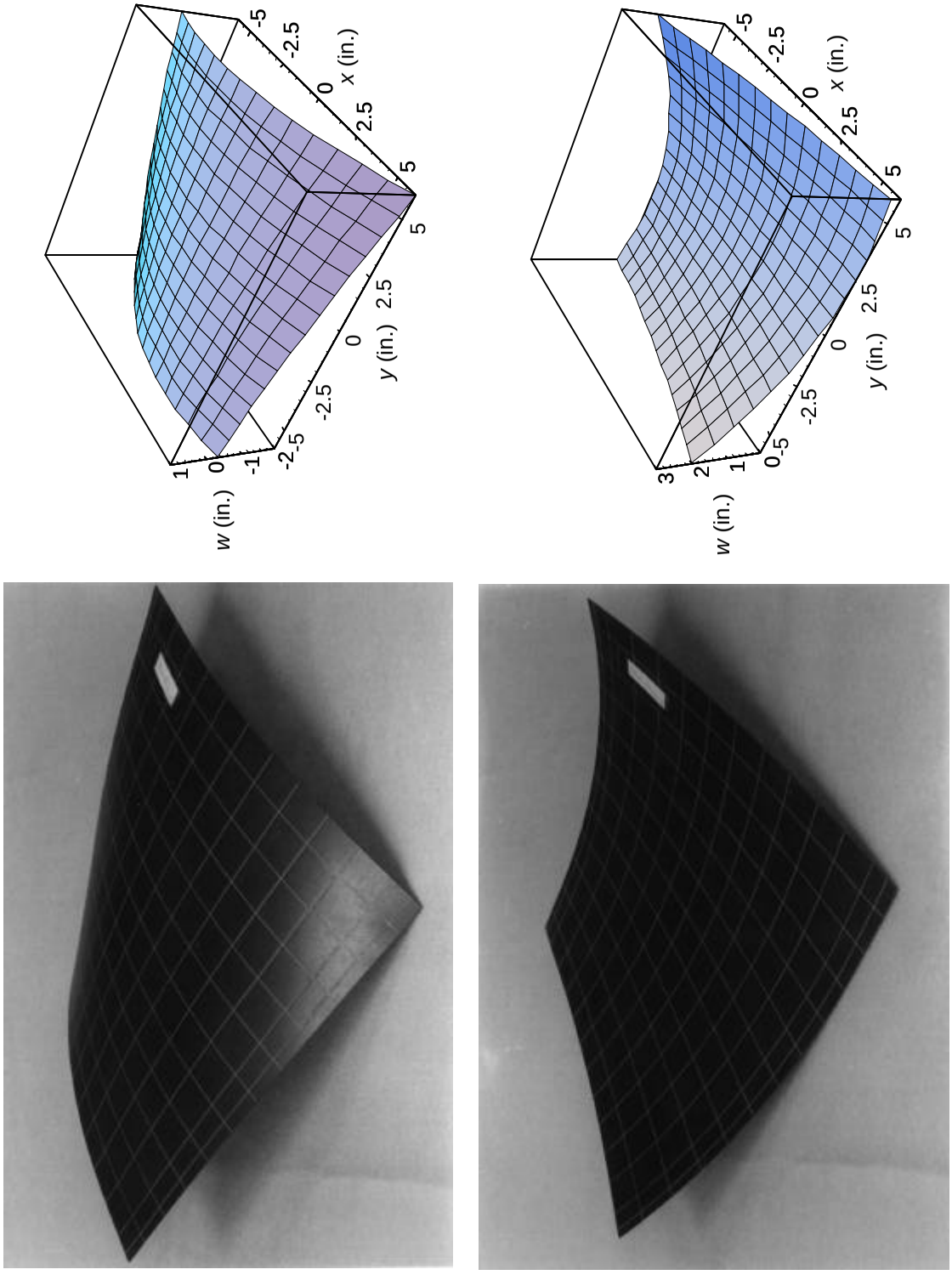

Fig. 3-12. Predicted and actual shapes of the $[-60_4/30_4]_T$ laminate

Chapter 4 Mechanics of general unsymmetric laminates subjected to known applied forces

This chapter presents the theory that was developed to predict the room-temperature deformation behavior of general unsymmetric laminates subjected to applied forces. The principle of virtual work will be used to derived the equilibrium equations relating the laminate curvatures to the applied forces. By solving the equilibrium equations as a function of the force level, relations between the laminate curvatures and the applied force can be derived and the force level at which the laminate changes shape can be determined. This simple approach has been previously used by the author and has proven to quite accurately predict the response of cross-ply unsymmetric laminates to applied forces [1, 2]. Understanding the effects of applied forces on the response of unsymmetric laminates is an important step in using SMAs to cause a change in the configuration.

4.1 Problem description

As described in Chapter 2, general unsymmetric laminates usually exhibit twist curvature as they are cooled to room temperature. This aspect needs to be taken into consideration when applying forces on the laminates. For a cross-ply unsymmetric laminate the twist curvature is zero and the forces can be simply applied either along the *x* or *y* direction, depending upon whether the major curvature is κ_x^o or κ_y^o. This was illustrated in Fig. 1-3 in the introduction. On the other hand, for a general unsymmetric laminate the twist curvature is non-zero. This means that to be the most efficient the forces should be applied along the principal curvature direction of the laminate.

Another aspect to consider is the fact that the model should simulate the effect of forces which eventually will be generated by SMA wires attached to the laminate, as was illustrated in Fig. 1-2. This implies that the forces will be applied along the line passing through the tips of the two supports shown in that figure. As these forces are applied on the laminate, the laminate curvatures should decrease, which, in turn, should induce small displacements of the support tips. As a result, the direction of the force may change from its initial orientation. This aspect has to be taken into account in the theory.

From these preliminary considerations, it was decided to fastened the supports along the direction of the larger principal room-temperature curvature, as illustrated in Fig. 4-1 (a). As was indicated in Chapter 2, this principal curvature direction is noted Φ_o, where the subscript "o" indicates that this value corresponds to the principal curvature of the laminate at room temperature and with no forces applied. Thus, Φ_o is the principal curvature direction computed in Chapter 2. The distance between the two supports is equal to $2L_s$. The location of the supports is given by the coordinates

$$\begin{aligned} x_s &= \pm L_s \cos\Phi_o \\ y_s &= \pm L_s \sin\Phi_o \,. \end{aligned} \tag{4.1}$$

Figure 4-1(b) shows an unsymmetric laminate subjected to forces F applied on supports attached to the laminate. The forces acting at a perpendicular distance e from the laminate surface are oriented along the line defined by the two support tips, denoted l, which is at an angle β with respect to the x axis. Note that β is equal to Φ_o when no force is applied. The forces exert a moment on the laminate which has a magnitude proportional to F and e. The response of the laminate to this force will be determined using the principle of virtual work.

4.2 Principle of virtual work

The principle of virtual work states that a structure is in equilibrium if and only if the total virtual work vanishes for every virtual displacement consistent with the constraints. This statement can be written as

$$\delta W_T = \delta\Pi - \delta W_F = 0, \tag{4.2}$$

where δW_T is the total virtual work, $\delta\Pi$ the first variation of the strain energy, and δW_F the virtual work done by the applied force. The first variation of the strain energy was computed in Chapter 2. Therefore, only the virtual work of the applied force needs to be determined. Considering the laminate in a deformed configuration, the virtual work of the applied force is defined as the work done by the force F as the laminate is given a virtual displacement. The resulting virtual displacement of the force is denoted as $\delta\vec{R}_F$, as illustrated in Fig. 4-2. The figure represents half of the cross section of the laminate along the l axis, which is oriented at an angle β with the x direction. Similar effects occur at the other support. Note that during the virtual displacement the force remains parallel to the x-y plane. The total virtual work of the force F acting on the two supports can be expressed as,

$$\delta W_F = \vec{F} \cdot \delta\overrightarrow{R_F}\Big|_{\substack{x = L_s\cos\Phi_o \\ y = L_s\sin\Phi_o}} + \vec{F} \cdot \delta\overrightarrow{R_F}\Big|_{\substack{x = -L_s\cos\Phi_o \\ y = -L_s\sin\Phi_o}}. \tag{4.3}$$

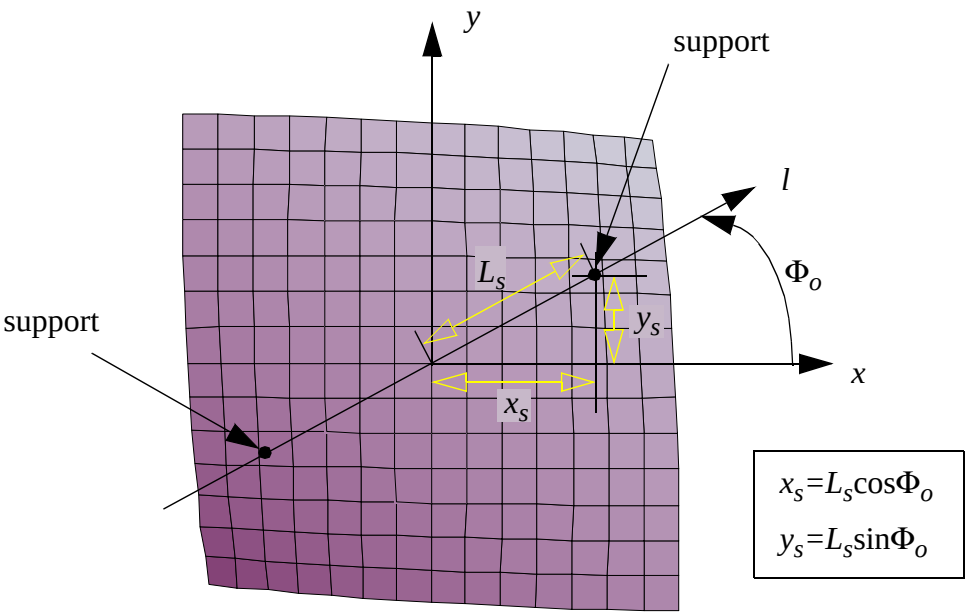

(a) plan view (F=0)

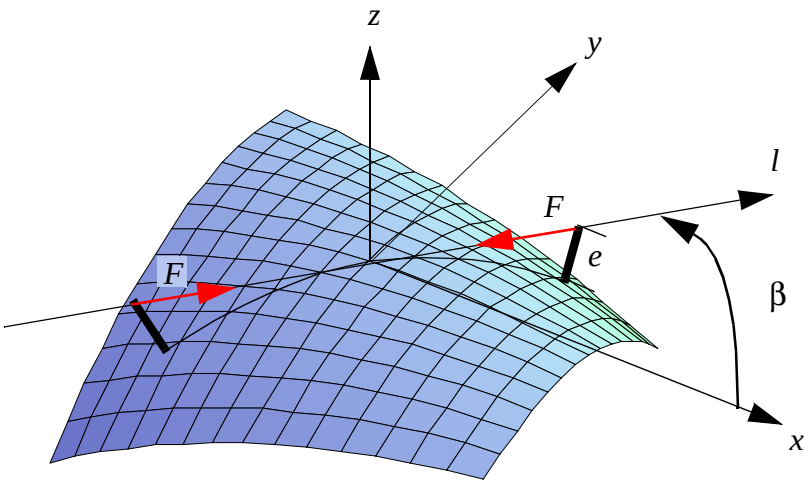

(b) overall view (F applied)

Fig. 4-1. Geometry of the force configuration

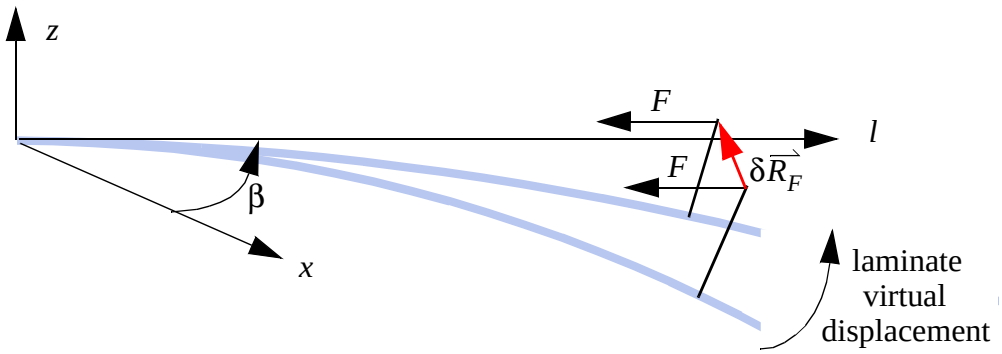

Fig. 4-2. Virtual displacement of the laminate

The virtual displacement $\delta\vec{R}_F$ is evaluated by first computing the position vector $\vec{R}_F$ of the force, relative to the origin of the coordinate system, and then taking its variation. The position vector $\vec{R}_F$ can be expressed as the sum of the position vector to the base of the support, $\vec{r}$, and the vector directed from the base of the support to the tip of the support, $\vec{n}^*$, as illustrated in Fig. 4-3, i. e.,

$$\vec{R}_F = \vec{r} + \vec{n}^*. \tag{4.4}$$

The vector $\vec{r}$, can be written as,

$$\begin{aligned}\vec{r}(x, y) = {} & (x + u^o(a, b, c, \Delta T, x, y))\vec{i} + \\ & (y + v^o(a, b, c, \Delta T, x, y))\vec{j} + \\ & w^o(a, b, c, \Delta T, x, y)\vec{k},\end{aligned} \tag{4.5}$$

where the expressions for the displacements u^o and v^o in terms of the unknown coefficients a, b, c are obtained by substituting eq. (2.17) into eq. (2.13). Since the vector $\vec{n}^*$ is normal to the surface, it can be expressed as

$$\vec{n}^* = \left(e + \frac{H}{2}\right)\vec{n}, \tag{4.6}$$

where $\vec{n}$ is the unit vector normal to the laminate surface at the support locations ($x = \pm L_s \cos\Phi_o$, $y = \pm L_s \sin\Phi_o$) and $\left(e + \frac{H}{2}\right)$ is the distance from the laminate reference surface to the tip of the support. By definition [34], the unit vector $\vec{n}$ at a point (x, y) on the laminate surface is given by,

$$\vec{n}(x, y) = \frac{\frac{\partial\vec{r}}{\partial x} \times \frac{\partial\vec{r}}{\partial y}}{\left|\frac{\partial\vec{r}}{\partial x} \times \frac{\partial\vec{r}}{\partial y}\right|}, \tag{4.7}$$

where the vectors $\frac{\partial\vec{r}}{\partial x}$ and $\frac{\partial\vec{r}}{\partial y}$ are tangent to the surface at point (x, y). Using the definition of $\vec{r}$

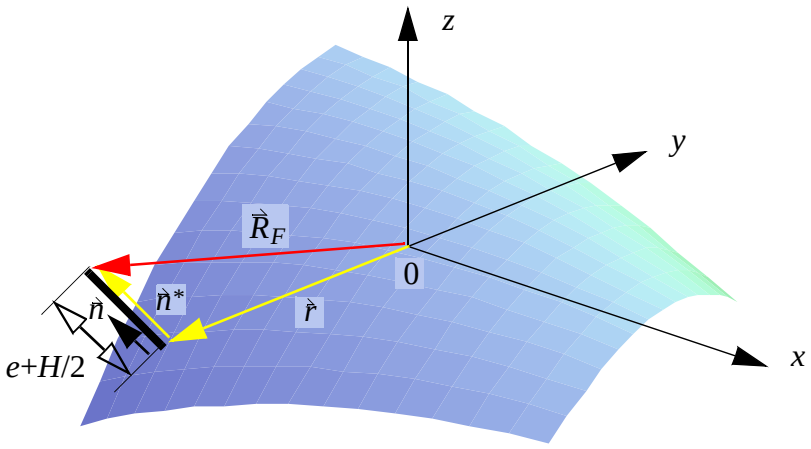

Fig. 4-3. Force position vector computation

given by eq. (4.5) to compute the unit vector $\hat{n}$, vector $\hat{n}^*$ can then be evaluated. Substituting the expressions for $\hat{n}^*$ and $\hat{r}$ into eq. (4.4), the force position vector $\vec{R}_F$ can be expressed as a function of *a*, *b*, and *c*, by

$$\vec{R}_F(x, y) = \hat{r}(a, b, c, \Delta T, x, y) + \left(e + \frac{H}{2}\right)\hat{n}(a, b, c, \Delta T, x, y) \cdot \tag{4.8}$$

Next, the virtual displacement $\delta\vec{R}_F$ can be computed by taking the variation of eq. (4.8), namely,

$$\begin{aligned} \delta\vec{R}_F &= \frac{\partial\vec{R}_F}{\partial a}\delta a + \frac{\partial\vec{R}_F}{\partial b}\delta b + \frac{\partial\vec{R}_F}{\partial c}\delta c \\ &= \delta\vec{R}_F(a, b, c, \delta a, \delta b, \delta c, \Delta T, x, y) \cdot \end{aligned} \tag{4.9}$$

The applied force $\vec{F}$ can be expressed in terms of its components in the *x*-*y*-*z* coordinate system by,

$$\begin{aligned} \vec{F}\Big|_{\substack{x = L_s\cos\Phi_o \\ y = L_s\sin\Phi_o}} &= (-F\cos\beta)\hat{i} + (-F\sin\beta)\hat{j} \\ \vec{F}\Big|_{\substack{x = -L_s\cos\Phi_o \\ y = -L_s\sin\Phi_o}} &= (F\cos\beta)\hat{i} + (F\sin\beta)\hat{j}, \end{aligned} \tag{4.10}$$

where the cos β and sin β can be evaluated using the expression for $\vec{R}_F$ given by eq. (4.8). Let $\hat{e}_l$ define the unit vector along the *l*-axis. Then $\hat{e}_l$ can be expressed as a function of $\vec{R}_F$ by,

$$\hat{e}_l = \frac{\vec{\bar{R}}_F(x_s, y_s) - \vec{\bar{R}}_F(-x_s, -y_s)}{\left|\vec{\bar{R}}_F(x_s, y_s) - \vec{\bar{R}}_F(-x_s, -y_s)\right|}, \tag{4.11}$$

where the vector defined by $\vec{\bar{R}}_F(x_s, y_s) - \vec{\bar{R}}_F(-x_s, -y_s)$ represents the vector pointing from the tip of the support at ($-L_s\cos\Phi_o$, $-L_s\sin\Phi_o$) to the tip of support at ($L_s\cos\Phi_o$, $L_s\sin\Phi_o$), as described in Fig. 4-4. Then the expressions for $\cos\beta$ and $\sin\beta$ needed in eq. (4.10) can be deduced from eq. (4.11) since,

$$\hat{e}_l = \frac{\vec{\bar{R}}_F(x_s, y_s) - \vec{\bar{R}}_F(-x_s, -y_s)}{\left|\vec{\bar{R}}_F(x_s, y_s) - \vec{\bar{R}}_F(-x_s, -y_s)\right|} = \cos\beta\,\vec{i} + \sin\beta\,\vec{j}\,. \tag{4.12}$$

By substituting eq. (4.10) and eq. (4.9) into eq. (4.3), and carrying out the dot product, the virtual work of the force can be expressed as,

$$\begin{aligned} \delta W_F &= \delta W_F(a, b, c, \delta a, \delta b, \delta c, F, \Delta T) \\ &= f_a^{\,v}(a, b, c, F, \Delta T)\delta a + f_b^{\,v}(a, b, c, F, \Delta T)\delta b + f_c^{\,v}(a, b, c, F, \Delta T)\delta c\,. \end{aligned} \tag{4.13}$$

Obviously, $f_a^{\,v}$, $f_b^{\,v}$, $f_c^{\,v}$ are also functions of the variables Φ_o, L, and e, which define the geometry associated with the supports on the laminate. Substituting eq. (4.13) into eq. (4.2), the total virtual work can be expressed as,

$$\begin{aligned} \delta W_T &= \delta\Pi(a, b, c, \Delta T) - \delta W_F(a, b, c, \delta a, \delta b, \delta c, \Delta T, F) \\ &= \frac{\partial\Pi}{\partial a}\delta a + \frac{\partial\Pi}{\partial b}\delta b + \frac{\partial\Pi}{\partial c}\delta c - f_a^{\,v}\delta a - f_b^{\,v}\delta b - f_c^{\,v}\delta c \\ &= (f_a - f_a^{\,v})\delta a + (f_b - f_b^{\,v})\delta b + (f_c - f_c^{\,v})\delta c \\ &= f_a^{\,F}(a, b, c, \Delta T, F)\delta a + f_b^{\,F}(a, b, c, \Delta T, F)\delta b + \\ &\quad f_c^{\,F}(a, b, c, \Delta T, F)\delta c\,. \end{aligned} \tag{4.14}$$

The laminate is in equilibrium if the total virtual work vanishes, i. e., $\delta W_T = 0$, for every admissible virtual displacement δa, δb, δc. Equating δW_T to zero results in 3 equilibrium equations relating the coefficients a, b, c to ΔT and F. These equations are given by

$$\begin{aligned} f_a^F(a, b, c, \Delta T, F) &= 0 \\ f_b^F(a, b, c, \Delta T, F) &= 0 \\ f_c^F(a, b, c, \Delta T, F) &= 0\,. \end{aligned} \tag{4.15}$$

Note that the equations of eq. (4.15) become the same as the ones in eq. (2.18) when the force F is equal to zero. By setting the temperature change ΔT equal to -280^{o}F and the force F to zero,

solving the equilibrium equations gives the cured shapes of the laminate at room temperature. By increasing F and keeping ΔT at -280°F, the solutions of the equilibrium equations give the configurations of the laminate as it is deformed by the force F at room temperature.

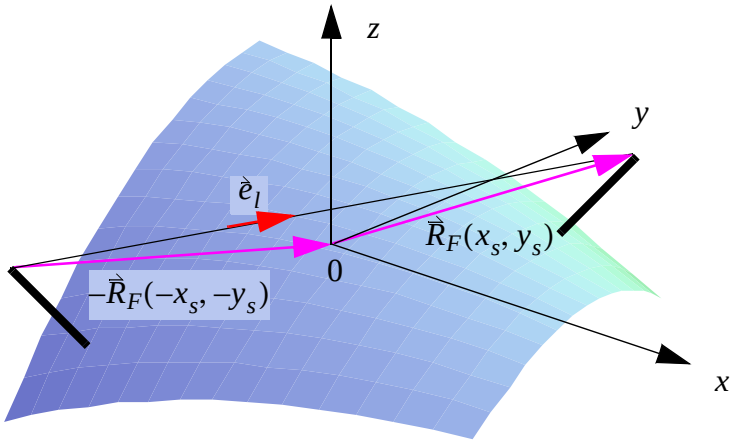

Fig. 4-4. Computation of unit vector $\grave{e}_l$

4.3 Numerical results

The set of three equations given by eq. (4.15) is solved for the 8 laminates from the three families. The geometric and material properties for the laminates are the ones used in Chapters 2 and 3. The force is applied according to the configuration given in Fig. 4-1, with e=0.55 in., L_s=4 in., and Φ_o taking the value for each laminate according to the results from Chapter 2. The value of e was chosen based on considerations of the force levels attainable with SMA wires, recovery strain levels in the SMA wires, and the moment levels needed to affect snap through. This will be discussed later. The temperature change is set equal to -280°F, while the force is increased from zero to a level at which the snap through of the laminate occurs. For every force level the equilibrium equations are solved, giving the curvatures κ_x^o, κ_y^o, κ_{xy}^o of the deformed laminate. From the values of the curvatures, the principal curvatures and principal curvature directions are computed using eq. (2.24). In addition, the angle β was computed as a function of F. All these computations were performed using *Mathematica* [33]. The results for the various laminates are represented in Figs. 4-5 to 4-10.

The deformation behavior of the laminates from the $[-\Theta_4/\Theta_4]_T$ family is illustrated in Fig. 4.5. When no force is applied the initial shapes of the laminates are cylindrical, with a large

principal curvature K_1 and a negligible principal curvature K_2. This corresponds to point C in the three parts of the figure. At F=0 the equilibrium equations have two other solutions for the laminates configuration. One corresponds to the unstable shape, point E, and the other corresponds to the second stable cylindrical shape, point D. Points C, D, and E are the same points denoted in Fig. 2-4. As the force is increased, curvature K_1 of the laminates decreases. When the force is large enough, point G in the figure, the laminates reach an unstable configuration and snap into the other cylindrical shape. The snap through is indicated by the arrow from G to D'. During the application of the force, the principal curvature direction Φ of the laminates decreases from its initial value Φ_o, except for the $[-45_4/45_4]_T$ laminate, for which Φ remains constant. At point G the principal curvature direction is equal or close to 45^o. This corresponds to the principal curvature direction for the unstable shape, as noticed in Fig. 2-7. To become unstable and snap, it seems that the laminate has to be brought back to a configuration similar to the initial unstable shape, corresponding to point E in Fig. 2-4. Thus, the principal curvature direction Φ has to decrease from its initial value Φ_o to become closer to the direction associated with point E, which is equal to 45^o for the laminates of this family. Since the principal curvature direction for the $[-45_4/45_4]_T$ is initially 45^o, it remains constant through the application of the force. Note that the snapping force increases with Θ, the highest value being for the $[-45_4/45_4]_T$ laminate. Considering now Fig. 4-6 representing the angle β as a function of the applied force, it can be noticed that this angle remains virtually the same as its initial value, Φ_o, throughout the application of the force, i. e., the direction the force is applied remains the same.

The force-curvature relations for the laminates from the $[(90\text{-}\Theta)_4/\Theta_4]_T$ family are presented in Fig. 4-7. At F=0 the laminates are initially in the configuration given by point C. Points C, E, and D in Fig. 4-5 correspond to these same points in Fig. 2-5. As the force increases, curvature K_1 decreases. Except for the cross-ply laminate ($\Theta=0^o$), the principal curvature direction Φ also decreases. When a certain force level is reached, the laminate becomes unstable, point G, and snaps into the other stable configuration D'. At point G the principal curvature direction Φ has become equal or close to zero. This corresponds to the value for the principal curvature direction of the unstable shape, as can be observed in Fig. 2-8, where the twist curvature for the unstable shape is equal to zero, and therefore Φ is also equal to zero. Note that for this family the snap-through force is maximum for the $[90_4/0_4]_T$ laminate and decreases with increasing Θ. Looking at the force-angle β relation depicted in Fig. 4-8, it is interesting to note that β remains essentially invariant with force level.

Figure 4-9 represents the force-induced behavior of the laminates from the $[(\Theta\text{-}90)_4/\Theta_4]_T$ family. As for the first two families, at F=0 the initial shape of the laminates is given by point C. As the force is applied, laminate principal curvature K_1 decreases. When the force is large enough the laminates reach an unstable configuration, point G, and suddenly change shape to the configuration giving by point D'. For this family the principal curvature direction remains the same up to the snap through. This is expected since it was observed in Fig. 2-9 that the stable cylindrical shapes had the same principal axes as the unstable saddle shape. The snapping force for the laminates from this family do not vary as much as for the first two families. However, as for the $[(90\text{-}\Theta)_4/\Theta_4]_T$ family, the $[90_4/0_4]_T$ laminate requires the largest force. This laminate is actually the one which requires the largest snapping force among all the unsymmetric laminates

considered in this work. Considering now the relation force-angle β represented in Fig. 4-10, it can be noticed that the angle β remains equal to its initial value Φ_o. Thus, as was observed for the first two families, the direction of the force is applied remains constant as the force level increases.

From the results presented in this chapter, it seems that the magnitude of the force generating the snap through is somewhat proportional to the magnitude of the angle between the fibers. For example, referring to Fig. 4-5, a $[-15_4/15_4]_T$ laminate, where the angle between the fibers is equal to 30^o, requires a smaller snapping force than a $[-30_4/30_4]_T$ or $[-45_4/45_4]_T$ laminate, where the angle between the fibers is, respectively, 60^o and 90^o. This relation is understandable, since the larger the angle between the fibers is, the larger the major principal curvature at room temperature is, as can be observed in Figs. 3-3 to 3-5. From these results it can be concluded that the snapping force is proportional to the room-temperature major principal curvature of the laminate.

4.4 Concluding remarks

The theory developed in this chapter appears to be able to model the deformation behavior of unsymmetric laminates subjected to applied forces, particularly the snap-through phenomenon occurring when the force reaches a certain value. Experiments conducted by the author [1,2] on a simple cross-ply $[0_2/90_2]_T$ graphite-epoxy laminate show that the developed theory predicts quite accurately the force-induced deformation of that laminate, as illustrated in Fig. 4-11. In the figure the strains at the top and bottom surface are represented as a function of the force applied on the laminate. The sudden change in the strains near F=5 lb is associated with the snap-through event. The magnitude of the measured snap-through load correlates well with the predicted snap-through load. Also, correlation of the strains between the theory and experiments is quite good except for force levels just prior to snap through. The deviations in the strains are thought to be due to local deformations occurring at the supports locations and to the unstable nature of the laminate as the force reaches the level for snap through. Despite the differences in the strains around the snap through, the developed theory appears to model the fundamental phenomenon correctly. It is anticipated that the theory just presented for more general unsymmetric laminates will be as accurate. This, of course, will be verified in the ensuing chapters.

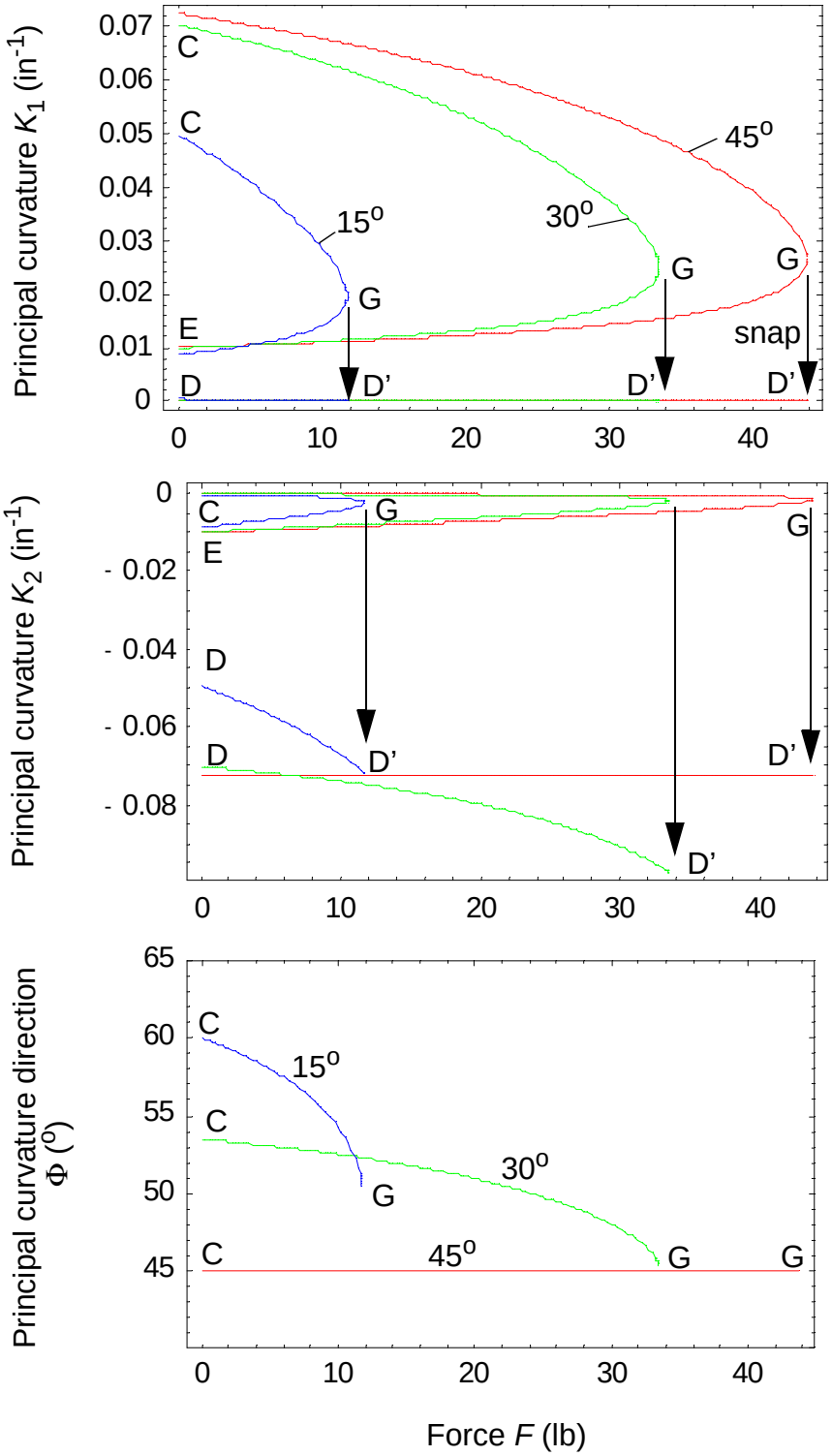

Fig. 4-5. Force-deformation relation for $[-\Theta_4/\Theta_4]_T$ laminates

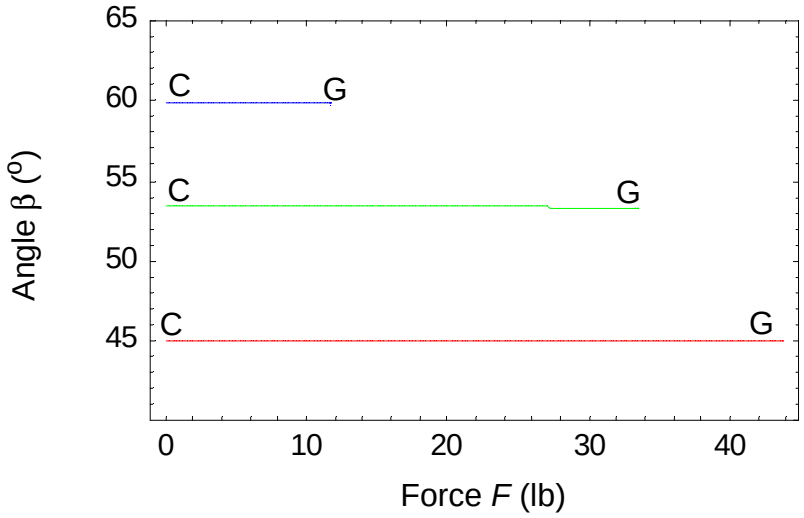

Fig. 4-6. Force-angle β relation for $[-\Theta_4/\Theta_4]_T$ laminates

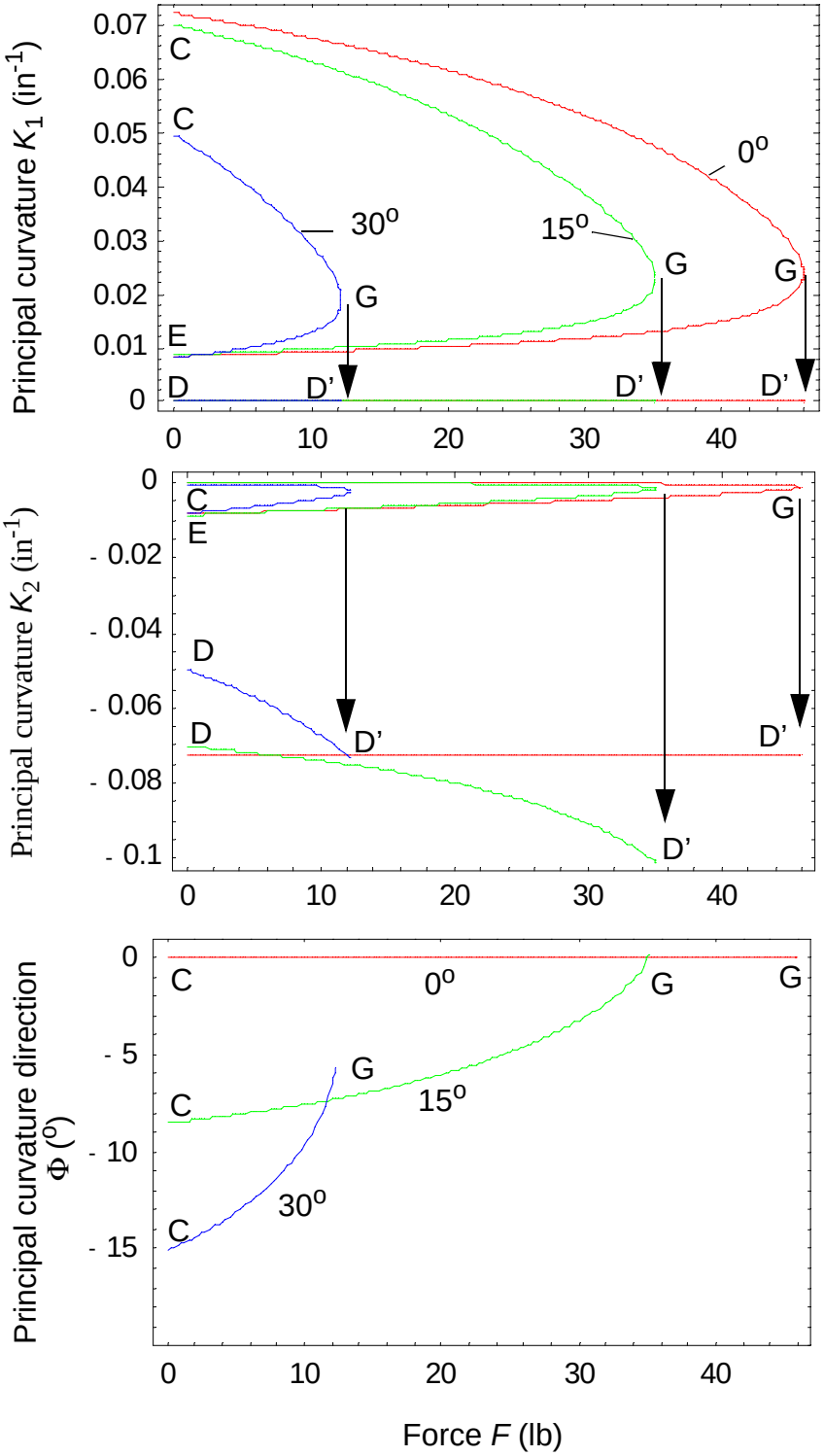

Fig. 4-7. Force-deformation relation for $[(90\text{-}\Theta)_4/\Theta_4]_T$ laminates

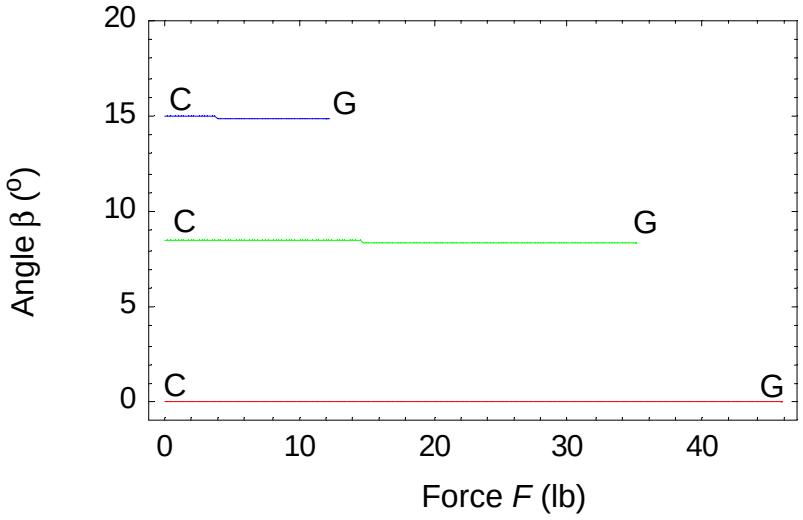

Fig. 4-8. Force-angle β relation for $[(90\text{-}\Theta)_4/\Theta_4]_T$ laminates

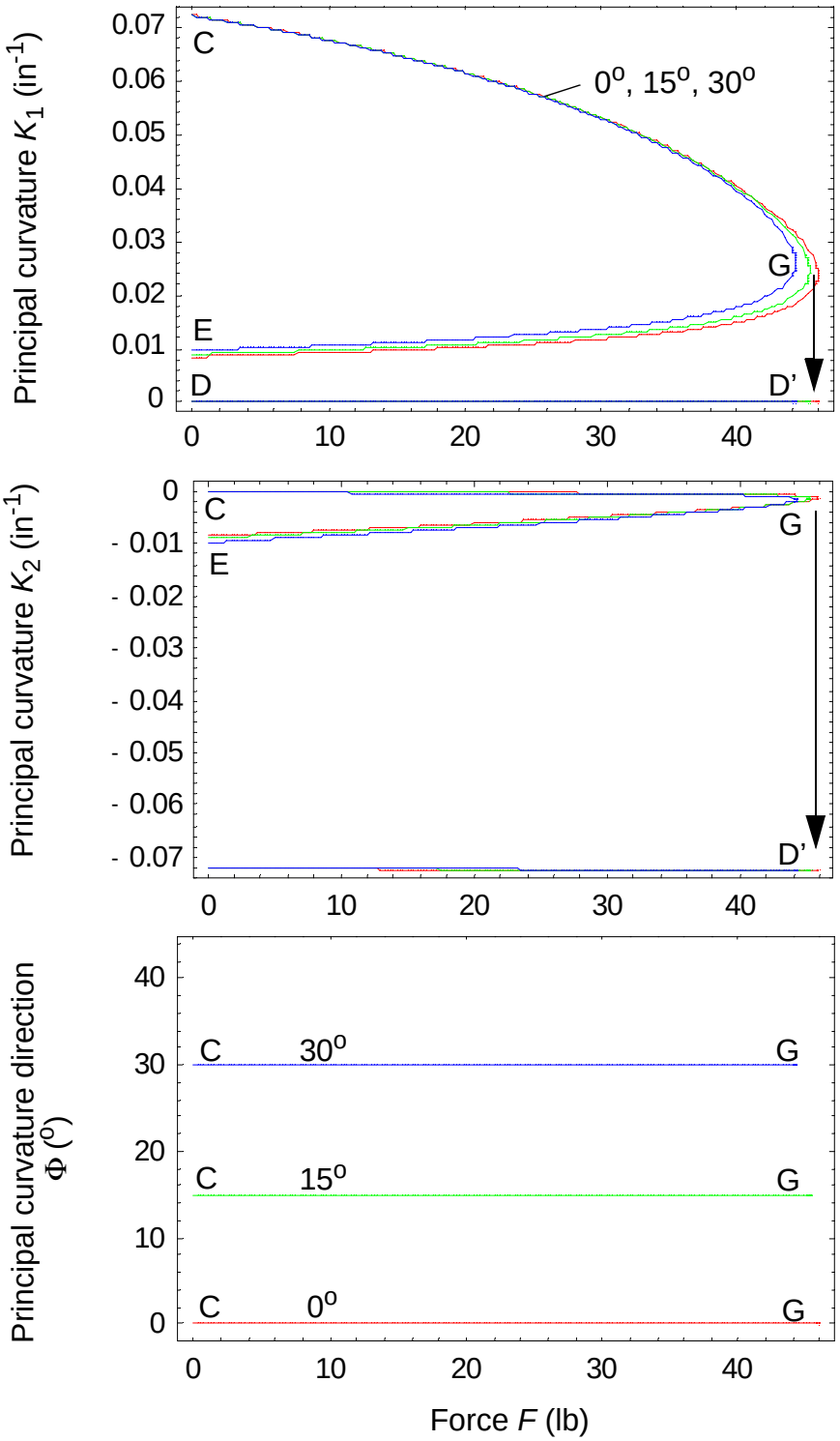

Fig. 4-9. Force-deformation relation for $[(\Theta\text{-}90)_4/\Theta_4]_T$ laminates

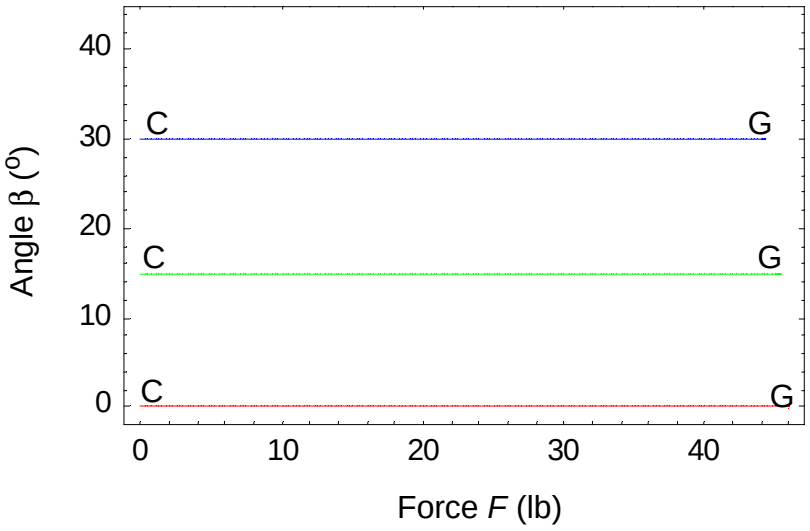

Fig. 4-10. Force-angle β relation for $[(\Theta\text{-}90)_4/\Theta_4]_T$ laminates

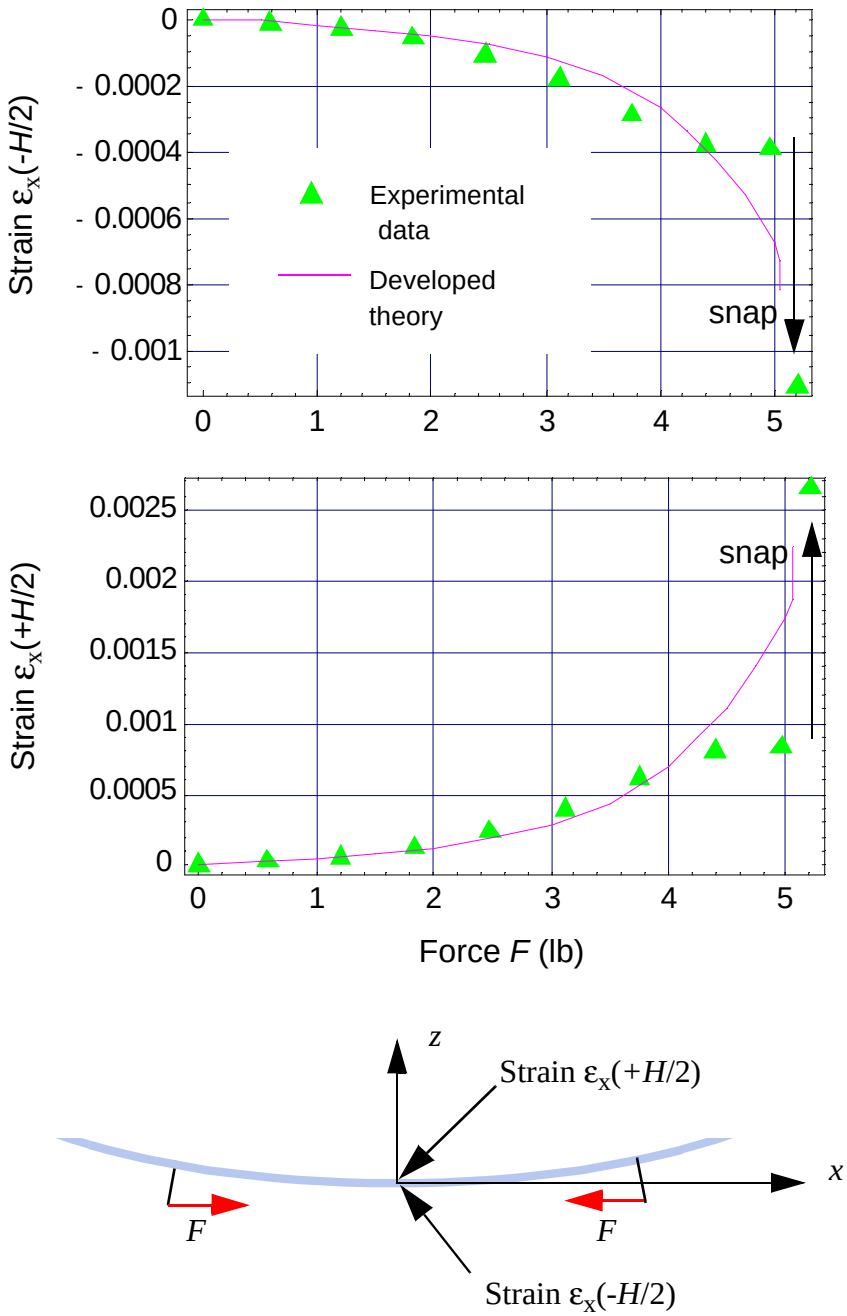

Fig. 4-11. Measured[1] and theoretical strains: Case of a $[0_2/90_2]_T$ laminate

1. Experimental results from Dano [1]

Chapter 5 Shape memory alloys in structures

In this chapter an existing constitutive model of SMAs will be briefly presented and implemented into the theory presented in Chapter 4 to predict the deformations of simple structures to SMA-induced forces. The discussed work in this chapter is viewed as somewhat of a calibration of the SMA wire used in the study.

5.1 Phenomenological approach

As was stated in Chapter 1, SMAs are alloys which, when plastically deformed and subsequently heated, are able to regain their original shape. The mechanism responsible for the shape recovery is a phase transformation of the material from martensite to austenite. In the martensitic phase the SMA is soft and can be plastically deformed with low stress levels. As the alloy is heated, austenitic transformation occurs between a certain temperature range, starting at temperature A_s (austenite start) and ending at temperature A_f (austenite finish), as illustrated in Fig. 5-1. As the alloy has reached the full austenitic phase at $T>A_f$, the martensite volume fraction, denoted ξ, takes a zero value. The phase transformation is reversible and can be initiated by lowering the temperature below temperature M_s (martensite start). A martensite volume fraction of one is reached when the alloy is cooled below M_f (martensite finish). The phase transformation from martensite to austenite is associated with the process of strain recovery. If the SMA is restrained by, for example, being attached to a structure, a force is generated in the SMA which, in turn, induces deformations in the structure. Figure 5-2 illustrates the particular example of a SMA wire attached on a narrow flat plate by way of short supports. As the SMA wire is heated above temperature A_s, strain recovery associated with the austenitic transformation is initiated and a force F is generated in the SMA wire. The force causes the plate to deform, specifically, to develop curvature.

To be able to predict the deformation behavior of a structure subjected to SMA-induced forces, the interaction of the SMA wire with the structure needs to be clearly understood, as well as the thermo-mechanical constitutive modeling involved in the strain recovery of the SMA.

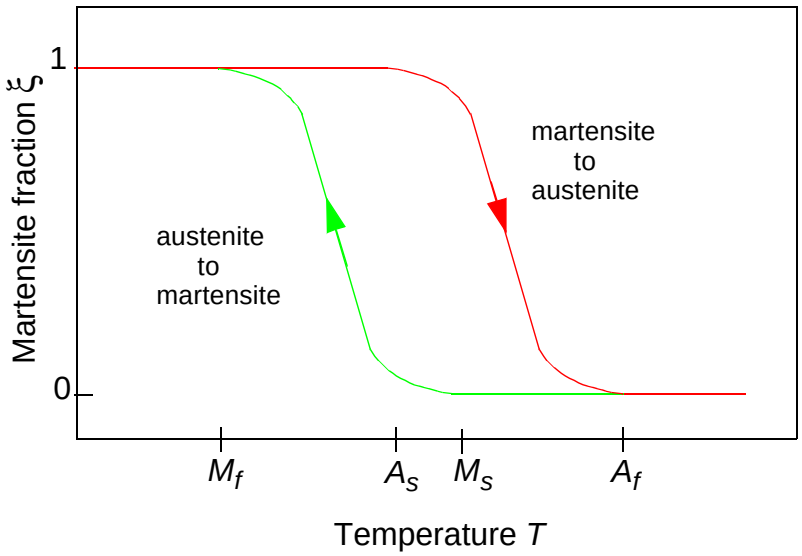

Fig 5-1. Phase transformation phenomenon in SMA

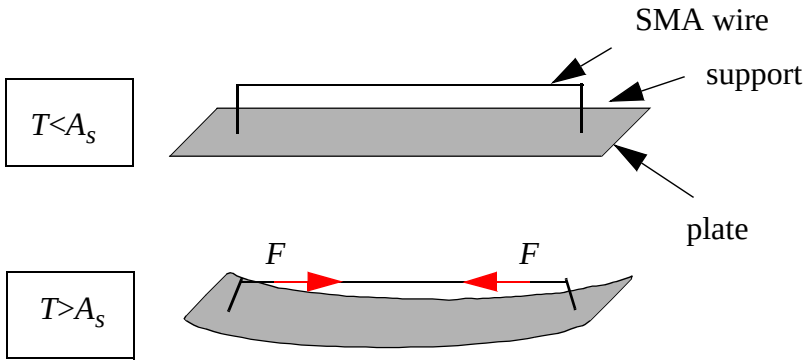

Fig 5-2. SMA wire attached on a simple narrow flat plate

5.2 Constitutive model of SMAs

As detailed in Chapter 1, the work here will be based on the SMA model developed by Boyd and Lagoudas [28]. The model uses a set of several equations relating the stress, strain, temperature, and martensite volume fraction in the SMA wire. The constitutive law is a simple

generalized Hooke's law, specifically,

$$\sigma = E\varepsilon^{e} = E(\varepsilon - \varepsilon^{t} - \alpha(T - T_o)), \tag{5.1}$$

where, σ, ε^{e}, ε, and ε^{t} are the uniaxial stress, elastic strain, total strain, and transformation strain, respectively. The quantities T and T_o are, respectively, the current and reference temperature. The extensional modulus E and thermal expansion coefficient α both dependent on the martensite volume fraction ξ, and are assumed to follow a rule-of-mixtures relationship, namely,

$$\begin{aligned} E &= E_A + \xi(E_M - E_A) \\ \alpha &= \alpha_A + \xi(\alpha_M - \alpha_A), \end{aligned} \tag{5.2}$$

where E_A, α_A and E_M, α_M are the properties of the SMA in, respectively, a pure austenitic (subscript A) and pure martensitic (subscript M) phase. The transformation strain ε^{t} is directly related to the martensite volume fraction by

$$\varepsilon^{t} = \varepsilon_o \xi, \tag{5.3}$$

ε_o being the initial plastic strain in the SMA wire. At ξ=1 the SMA wire is fully martensitic and the transformation strain is equal to the initial strain ε_o. As transformation from the martensitic to the austenitic phases occurs, the initial strain is recovered and therefore strain ε^{t} decreases. The constitutive equation eq. (5.1) is used in parallel with a kinetic equation governing the phase transformation which has been derived by using the first and second law of thermodynamics (see Boyd and Lagoudas [28] for more details). This kinetic equation can be expressed as

$$\Psi = \sigma^{eff}\varepsilon_o + \frac{1}{2}\Delta a^{1}\sigma^{2} + \Delta\alpha\sigma(T - T_o) + \rho\Delta a^{4}T - \frac{\partial f(\xi)}{\partial \xi} - Y = 0, \tag{5.4}$$

where ρ is the SMA density, Δa^{1}=1/E_M-1/E_A, $\Delta\alpha$=α_M-α_A, σ^{eff}=σ-$\rho b_2 \varepsilon^{t}$, b_2 being the kinetic hardening parameter, $\rho\Delta a^{4}$ is the difference of the entropy between the martensite and the austenite phases at the reference state, Y is the threshold value of transformation, $f(\xi) = \frac{1}{2}\rho b_1 \xi^{2}$, b_1 being the isotropic hardening parameter. Parameter b_2 is assumed to be zero. Parameters $\rho\Delta a^{4}$, Y, and b_1 take different values, depending on the direction of the transformation, martensite-to-austenite or austenite-to-martensite. For a martensite-to-austenite transformation,

$$\begin{aligned} \rho\Delta a^{4} &= -C_A\varepsilon_o \\ Y &= -C_A\varepsilon_o A_{fo} \\ b_1 &= \frac{1}{\rho}C_A\varepsilon_o(A_{fo} - A_{so}), \end{aligned} \tag{5.5}$$

whereas for a austenite-to-martensite transformation,

$$\begin{aligned} \rho\Delta a^4 &= -C_M\varepsilon_o \\ Y &= -C_M\varepsilon_o M_{so} \\ b_1 &= \frac{1}{\rho}C_M\varepsilon_o(M_{so}-M_{fo})\,. \end{aligned} \tag{5.6}$$

In the above expressions M_{so}, A_{so}, M_{fo}, and A_{fo} are the start and finish temperatures at zero stress for, respectively, the martensitic (M) and the austenitic (A) transformation. The parameter C_A and C_M are the slopes of the curves of the so-called critical stress versus temperature. The stress in the SMA wire should stay within a certain interval for a transformation of phase to take place. For transformation to martensite,

$$C_M(T-M_{so}) < \sigma < C_M(T-M_{fo})\ , \tag{5.7}$$

and for transformation to austenite,

$$C_A(T-A_{fo}) < \sigma < C_A(T-A_{so})\ , \tag{5.8}$$

the expressions on the left and right side of each inequality being referred to as the critical stresses. Fig. 5-3 represents the latter equation. As the wire is heated above A_{so}, the austenitic transformation is initiated and the SMA wire starts recovering strain. As long as the stress σ greater than one critical stress and less than the other critical stress, the transformation and the strain recovery processes continue. As the stress reaches the critical value, the transformation ends and the recovery process is terminated, even though the initial strain may not be totally recovered. As the phase transformation can only take place when $C_A(T-A_{fo}) < \sigma < C_A(T-A_{so})$, the use of eq. (5.4) is valid only in this stress interval.

Substituting eqs. (5.1) and (5.3) into eq. (5.4) leads to a nonlinear algebraic equation expressed in terms of variables ε, T, and ξ, namely,

$$\Psi = \Psi(\varepsilon, T, \xi) = 0\,. \tag{5.9}$$

The thermomechanical response of the SMA wire can be characterized by solving eq. (5.9), relating the stress, strain, martensite volume fraction, and temperature in the wire.

This constitutive model can be used to predict the deformations of structures actuated by SMAs. In the following section the case of a simple narrow aluminium plate being deformed by an externally attached SMA wire will be discussed.

5.3 Modeling of a narrow aluminium plate deformed by a SMA wire

The motivation for studying SMA actuators on a simple narrow aluminium plate is to make sure that the interaction between the structure and the SMA actuators is correctly understood, and

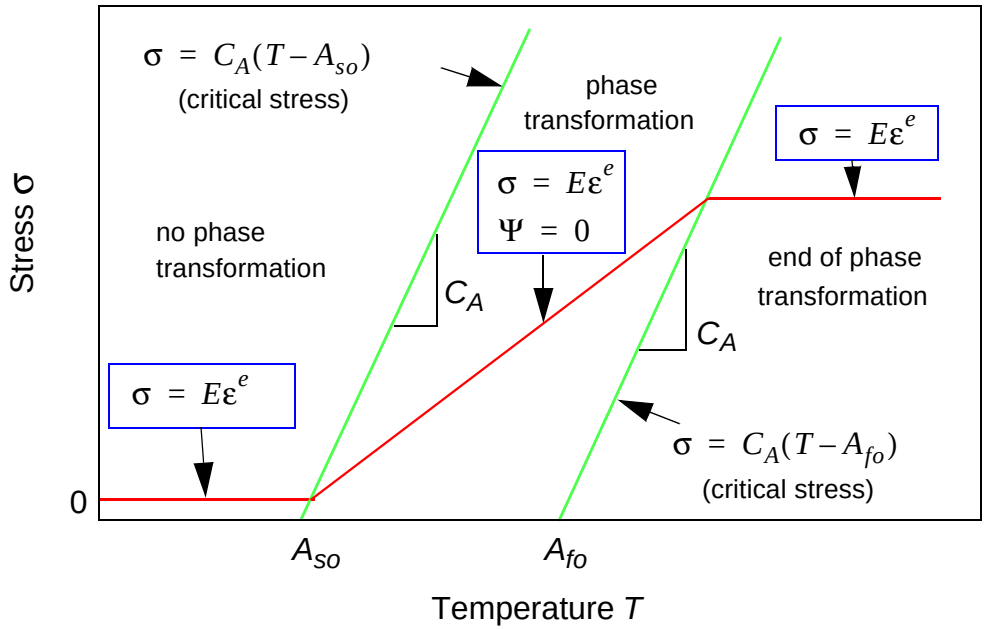

Fig 5-3. Stress-temperature relation of SMA

to check the accuracy of the SMA model by performing actual experiments. Accordingly, the SMA wire was attached to the plate in a manner similar to that to be used on the unsymmetric laminates. The idea was to obtain similar conditions for using the SMA wire so that the results obtained with the narrow aluminium plate could be used to understand the response that the unsymmetric laminate subjected to a similar wire would have. Moreover, using a similar method for attaching an SMA wire to the plate would allow the use of the equations that were derived in Chapter 4, eq. (4.15), to describe the deformations of the laminates due to applied forces. These equations, given by

$$\begin{aligned} f_a^F(a, b, c, \Delta T, F) &= 0 \\ f_b^F(a, b, c, \Delta T, F) &= 0 \\ f_c^F(a, b, c, \Delta T, F) &= 0, \end{aligned} \tag{5.10}$$

relate the laminate curvatures (-a), (-b), and (-c) to the applied force F and temperature change ΔT. In Chapter 4 the forces were applied to the unsymmetric laminate at room temperature. Therefore, ΔT was set equal to -280^{o}F, as illustrated in Fig. 5-4 (a). To study the effect of the forces on a flat unsymmetric laminate, eq. (5.10) can still be used by setting ΔT to zero, Fig. 5-4 (b). Additionally, by changing the geometrical and material properties of the laminate, the deformations of a narrow aluminium plate, Fig. 5-4 (c) can be studied using the same set of equations.

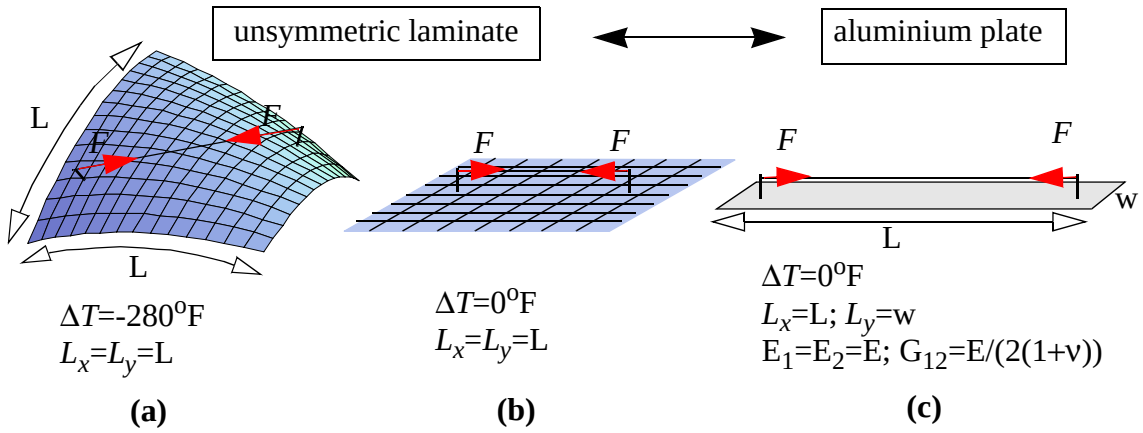

Fig 5-4. Problem examples which can be solved using eq. (5.10)

In the above spirit, then, the set of equations in eq. (5.10) is solved using

$$E = 10\times10^6 \text{ psi} \qquad \nu = 0.3 \qquad G = \frac{E}{2(1+\nu)} = 3.84\times10^6 \text{ psi}$$
$$L_x = 20.75 \text{ in} \qquad L_y = 3 \text{ in} \qquad H = 0.0625 \text{ in} \tag{5.11}$$

for the properties of the aluminium plate, and

$$e = 0.625 \text{ in} \qquad x_s = 9.75 \text{ in} \qquad y_s = 0 \tag{5.12}$$

for the force configuration, as illustrated in Fig. 5-5. The equations are solved as a function of F in terms of a, b, and c representing the plate curvatures, κ_x^o, κ_y^o, and κ_{xy}^o. The results are shown in Fig. 5-6. As expected, when forces are applied, the plate develops a large negative curvature κ_x^o, a small positive curvature κ_y^o, and no twist curvature κ_{xy}^o. From the values for a, b, c, the remaining 25 coefficients (c_{ij}, d_{ij}, e_k) of eq. (2. 17) can be computed and the strains in the plate evaluated. The strains induced at the center of the plate (x=y=0) are given by

$$\begin{aligned}\varepsilon_x(z) &= \varepsilon_x^o\Big|_{x=y=0} + z\kappa_x^o \\ &= c_{oo} - za \cdot\end{aligned} \tag{5.13}$$

The strains at the top (z=+H/2) and bottom (z=-H/2) surface of the plate are represented in Fig. 5-7. Note that the strain at the top surface is negative. The quantity -ε_x(+H/2) is represented on the graph so that the magnitude of the two strains can be conveniently compared. It is interesting to note that the top and bottom strains are not equal in magnitude. The strain at the top surface

$\varepsilon_x(+H/2)$ is actually larger in magnitude than the strain at the bottom surface $\varepsilon_x(-H/2)$. This is due to the combined effects of the compressive force F and the geometric nonlinearities, the latter actually having the largest contribution.

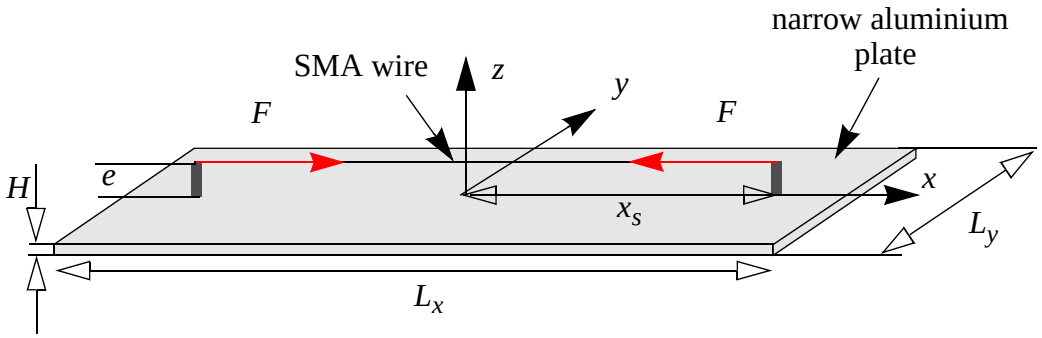

Fig 5-5. Set-up for aluminium plate experiment

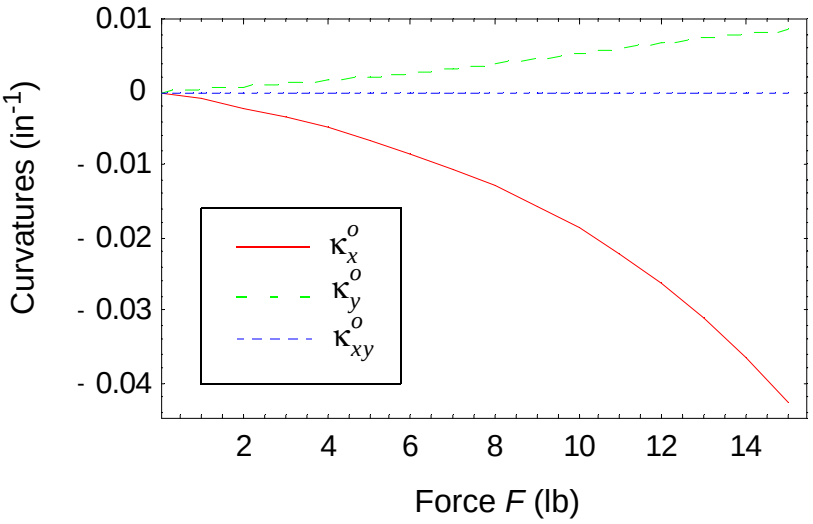

Fig 5-6. Force-curvature relations for the narrow aluminium plate

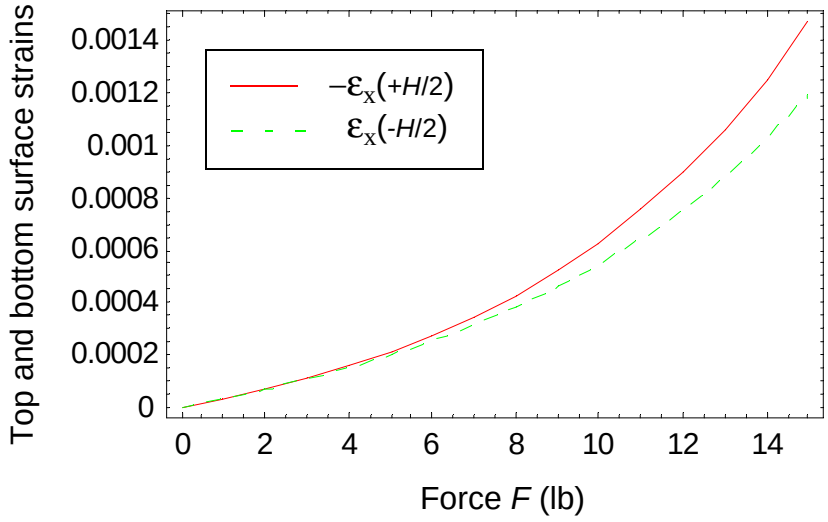

Fig 5-7. Force-strain relations for the narrow aluminium plate

Considering the forces induced by a SMA wire: The stress and total strain in the wire are related to the plate deformations by

$$\sigma = \frac{F}{A_{SMA}} \tag{5.14}$$

$$\varepsilon = \varepsilon_o + \frac{\Delta L_{SMA}}{L^o_{SMA}} = \varepsilon_o + \frac{L_{SMA} - L^o_{SMA}}{L^o{}_{SMA}}, \tag{5.15}$$

where A_{SMA} is the SMA wire cross section area, and ΔL_{SMA}, L_{SMA}, and L^o_{SMA} are respectively, the change in length, current length, and length of the SMA wire just after it has been deformed to strain level ε_o. As illustrated in Fig. 5-8, ΔL_{SMA} can be computed for a given force F using the support displacements. These can be evaluated from the plate deformations (see Chapter 4), namely,

$$\begin{aligned} \Delta L_{SMA} &= L_{SMA} - L^o_{SMA} \\ &= \left|\vec{R}_F(x_S) - \vec{R}_F(-x_S)\right| - \left|\vec{R}_F(x_S) - \vec{R}_F(-x_S)\right|_{F=0}. \end{aligned} \tag{5.16}$$

In the above x_S is the horizontal distance from the center of the plate to the base of a support, and $\vec{R}_F$ is the position vector to the tip of the support, where the force F is applied. Thus, the strain in the SMA wire can be expressed by

$$\varepsilon = \varepsilon_o + \left(\frac{\left|\vec{R}_F(x_S) - \vec{R}_F(-x_S)\right|}{\left|\vec{R}_F(x_S) - \vec{R}_F(-x_S)\right|_{F=0}} - 1 \right). \tag{5.17}$$

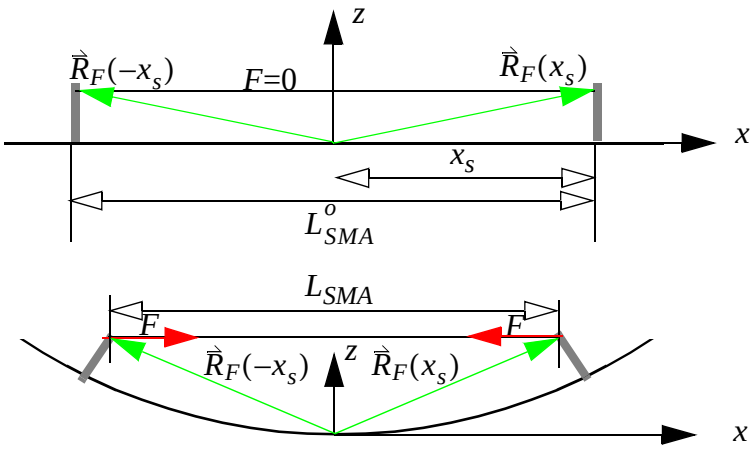

Fig 5-8. Computation of the change in length of the SMA wire

Using an iterative process, the deformations of the plate can be predicted as a function of the temperature in the SMA wire. Assuming values for the total strain in the wire, ε, and the temperature of the wire, *T*, the nonlinear equation Ψ=0, eq. (5.4), can be solved for the martensite volume fraction ξ. Substituting this value into eq. (5.3), the transformation strain ε^t is evaluated. Substituting the values for ε, *T*, and ε^t into eq. (5.1) the stress in the SMA wire is determined. Using eq. (5.14), the force *F* applied on the plate is obtained and the curvatures of the plate are computed by solving eq. (5.10). From the values for *a*, *b*, and *c*, $\vec{R}_F$ can be evaluated. Substituting these values into eq. (5.17), a new value for the strain in the SMA wire, ε, is computed. The same computations are performed another time with the new value for ε. This procedure is followed until the value computed for ε has converged. Using *Mathematica* [33], this iterative process is performed for every increase in the SMA wire temperature. The computation method is summarized in Fig. 5-9.

The computations are performed using the following material properties and initial plastic strain ε_o for the SMA wire,

$$\begin{array}{ll} E_A=9710 \text{ Ksi} & C_A=1.987 \text{ Ksi/}^o\text{C} \\ E_M=3810 \text{ Ksi} & A_{so}=34.6\ ^o\text{C} \\ a_A=11\times10^{-6}\ /^o\text{C} & A_{fo}=49\ ^o\text{C} \\ a_M=6.6\times10^{-6}\ /^o\text{C} & A_{SMA}=(\pi d^2)/4 \\ \varepsilon_o=5\% & d=20\ 10^{-3} \text{ in.} \end{array} \qquad (5.18)$$

where *d* is the diameter of the SMA wire. The results are presented in Figs. 5-10 to 5-12. In Fig. 5-10 the predicted actuation force generated by the SMA wire is represented as a function of the temperature in the wire. As the temperature reaches the austenite start temperature A_{so}, the

austenitic transformation is initiated and strain recovery in the wire begins to generate a force. As the wire is further heated, the force continues to increase. The phase transformation should finish as soon as the force F reaches the critical value (dotted line on right), or when the strain is fully recovered.

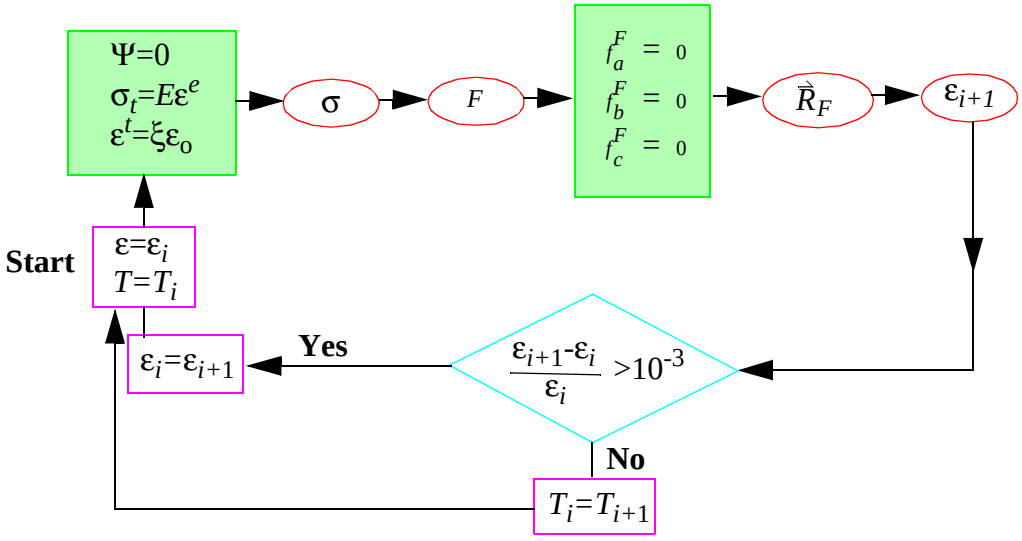

Fig 5-9. Description of the iterative process used in the computation

The predicted strains at the top and bottom surface of the plate induced by the SMA wire are represented in Figs. 5-11 and 5-12. No strains are induced in the plate as long as the SMA wire is not heated above A_{so}. When the temperature exceeds A_{so}, strains start to develop as the SMA-actuated force increases.

From these theoretical results, it is predicted that the SMA wire is able to induce reasonable strain levels in the plate. To check the validity of the predictions, experiments were conducted on a narrow aluminium plate with an SMA wire attached in the manner assumed in Fig. 5-5.

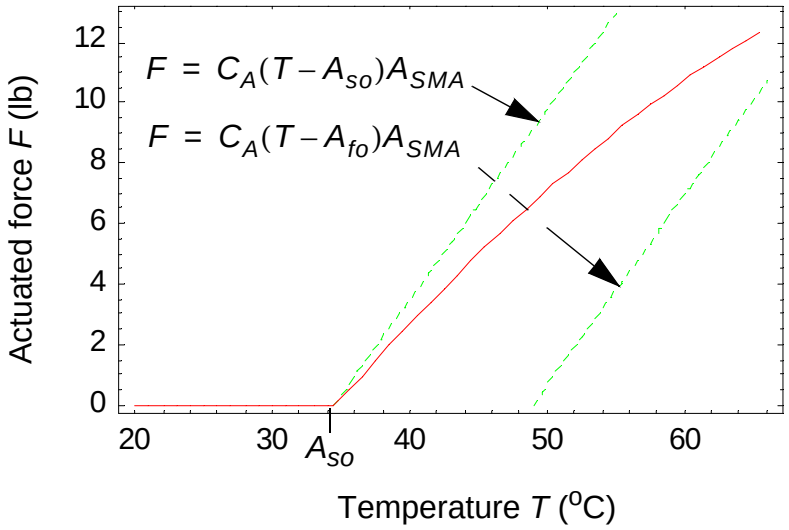

Fig 5-10. Temperature-actuation force relation

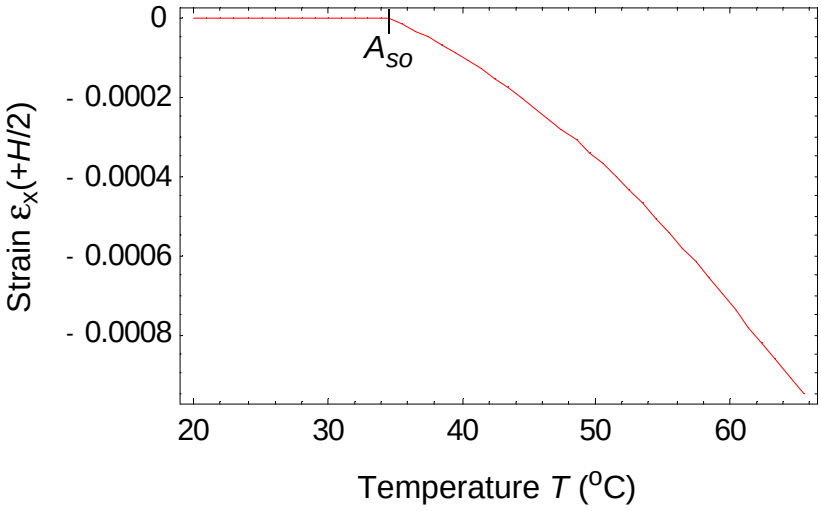

Fig 5-11. Strain-temperature relation on the top surface of the plate

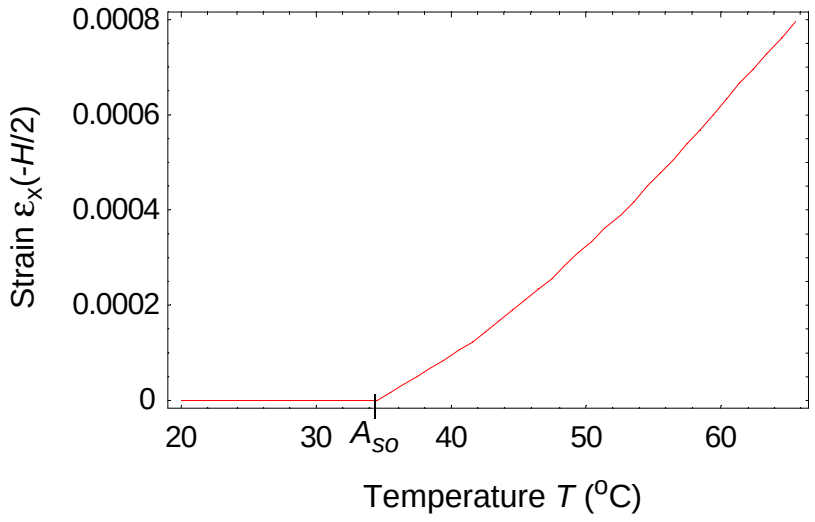

Fig 5-12. Strain-temperature relation on the bottom surface of the plate

5.4 Experimental verification of the model

5.4.1 Description of set-up

The aluminium plate used in the experiments had the same characteristics as given in eq. (5.11). The SMA wire was stretched to generate an initial plastic strain ε_o of 5%. It was then attached to the plate using the same configuration as given by eq. (5.12). The properties of the SMA wire were assumed to be the same as the ones given in eq. (5.18). However, the material properties related to the austenitic phase transformation (A_{so}, A_{fo}, and C_A) are strongly influenced by the manufacturing process and may not be exactly equal to the expected "standard" properties. As illustrated in Fig. 5-13, which illustrates the experimental set-up, one strain gage was bonded at the center of the top and bottom surface of the plate. The SMA wire was heated resistively by applying voltage. Two thermocouples were bonded to the wire to measure the temperature at two locations along the SMA wire. The temperature in the wire was evaluated by computing an average value of the two measurements.

5.4.2 Measurements

The SMA wire was heated progressively by slowly increasing the voltage. For each voltage increment, the temperature in the wire and the strains in the plate were measured. The voltage had to be increased slowly in order to catch the beginning of the austenitic transformation, temperature A_{so}. As the austenitic start temperature was reached, the phase transformation occurred quite fast and it was actually difficult to simultaneously measure the strains and the temperature. As the voltage was further increased, the strains in the plate reached a stationary value, indicating that the phase transformation was finished.

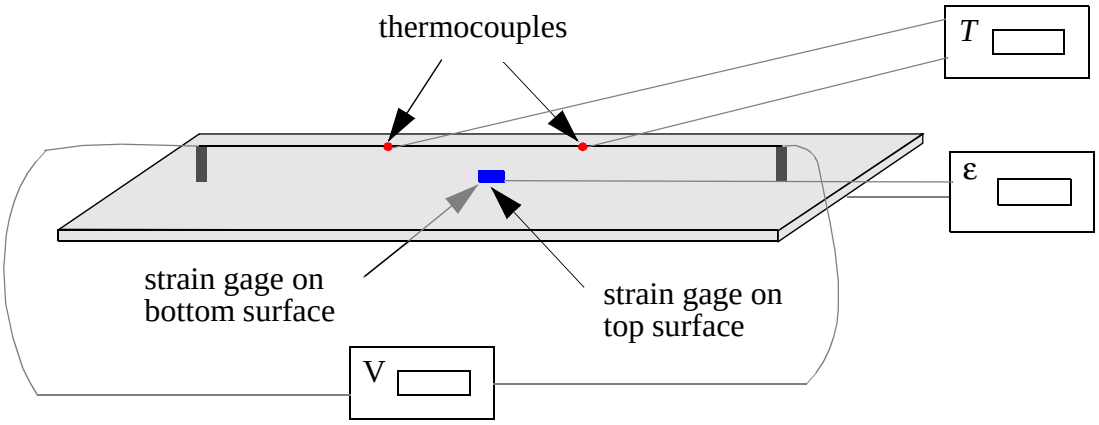

Fig 5-13. Description of aluminium plate set-up

5.4.3 Experimental results

The strains measured as a function of temperature are represented in Figs. 5-14 and 5-15. Predictions of the model are also indicated in the figures. As the wire is heated from room temperature, the strains remain close to zero. After the temperature has reached about 30 ^{o}C, the strains start increasing at a high rate. When the temperature equals 60 ^{o}C, the strains stop increasing and remain constant, even though the SMA wire continues to be heated. Comparing the experimental results with the predictions computed previously (dotted lines, which are the solid lines from Figs. 5-11 and 5-12), it can be observed that the austenitic start temperature A_{so} is actually slightly less than its theoretical value of 34.6 ^{o}C used in the prediction. Furthermore, the rate of increase of the measured strains is different than predicted. In the experiments, the strains increase at a higher rate than predicted and reach a plateau at about 60 ^{o}C, whereas the predictions indicate that the strains are still increasing after that temperature. From these observations it seems that the austenite finish temperature (A_{fo}) in the experiments was actually less than the

theoretical value of 49 ^{o}C. Using a simple method of trial and error on the value for A_{fo}, it was found that using 38 ^{o}C for A_{fo} and 30 ^{o}C for A_{so} in the model gave predictions which were quite close to the experimental measurements, as illustrated in Figs. 5-14 and 5-15.

Predictions for the total strain of the SMA wire during the phase transformation are shown in Fig. 5-16. As can be seen, the SMA wire has actually not quite recovered all its initial plastic strain when the phase transformation is interrupted due to the SMA wire becoming saturated with stress, i. e., ξ in eq. (5.3) did not reach zero.

Photos were taken during the experiment. One photo, Fig. 5-17 (a), shows the plate before voltage was applied to the SMA wire. The SMA wire was not generating any force and thus the plate is completely flat. The other photo, Fig. 5-17 (b), was taken after the SMA wire had saturated with strain (note that the voltage is now non-zero in the picture). The force generated by the SMA wire is maximum and the plate has reached its greatest deflection.

From the experimental results presented in this chapter, it appears that the constitutive model of Lagoudas and co-workers adequately represents the behavior of SMA wire within the context of usage in the current study. The theoretical temperatures associated with the phase transformation, A_{so} and A_{fo}, provided by the manufacturer had to be decreased by a few degrees to match the ones observed experimentally. After this adjustment, reasonably good correlations were established between the experiments and the predictions. Since the behavior of SMA wire on a simple structure like this aluminium plate seems to be understood and correctly predicted, using SMA wires on more complex structures like unsymmetric laminates can now be considered. This is the subject of the next chapter.

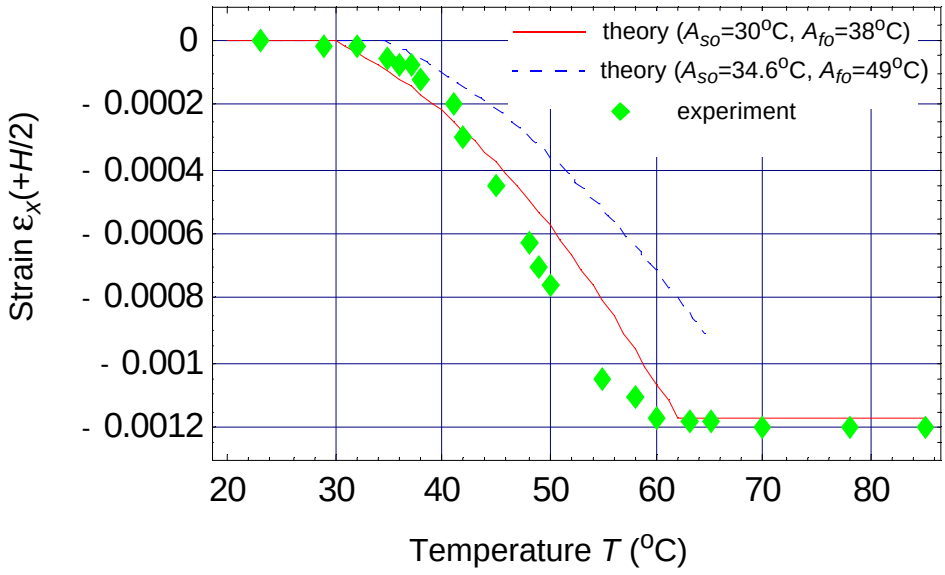

Fig 5-14. Strain at the top surface: Comparison of the measurements with the predictions

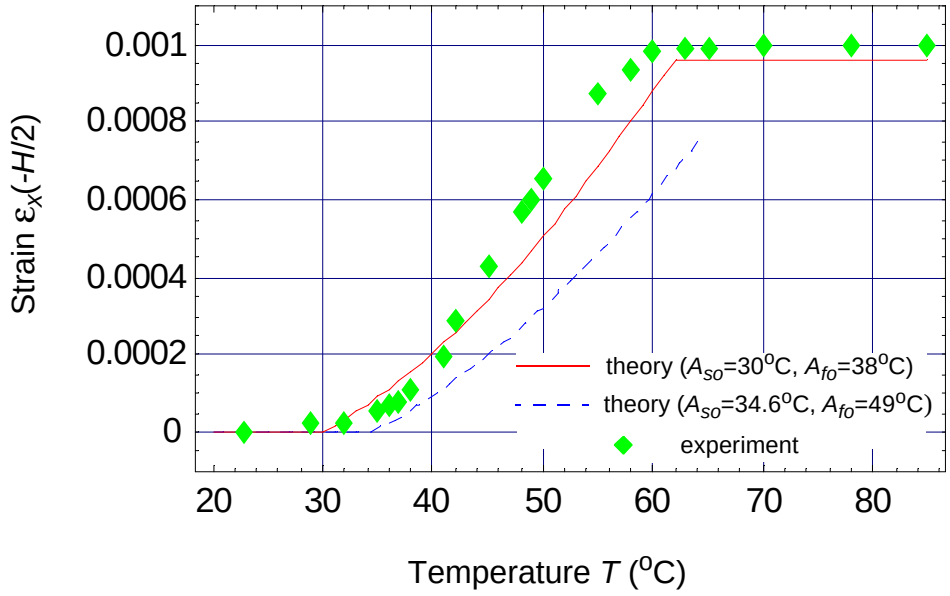

Fig 5-15. Strain at the bottom surface: Comparison of the measurements with the predictions

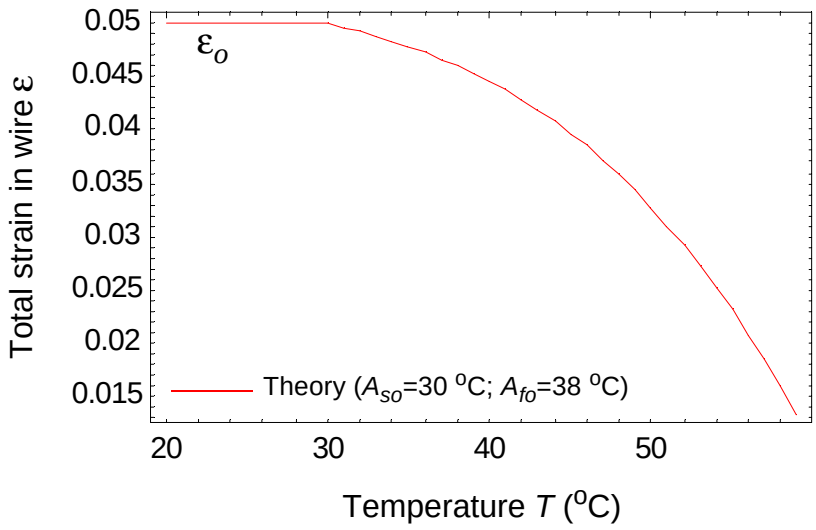

Fig 5-16. Total strain-temperature relation in the SMA wire

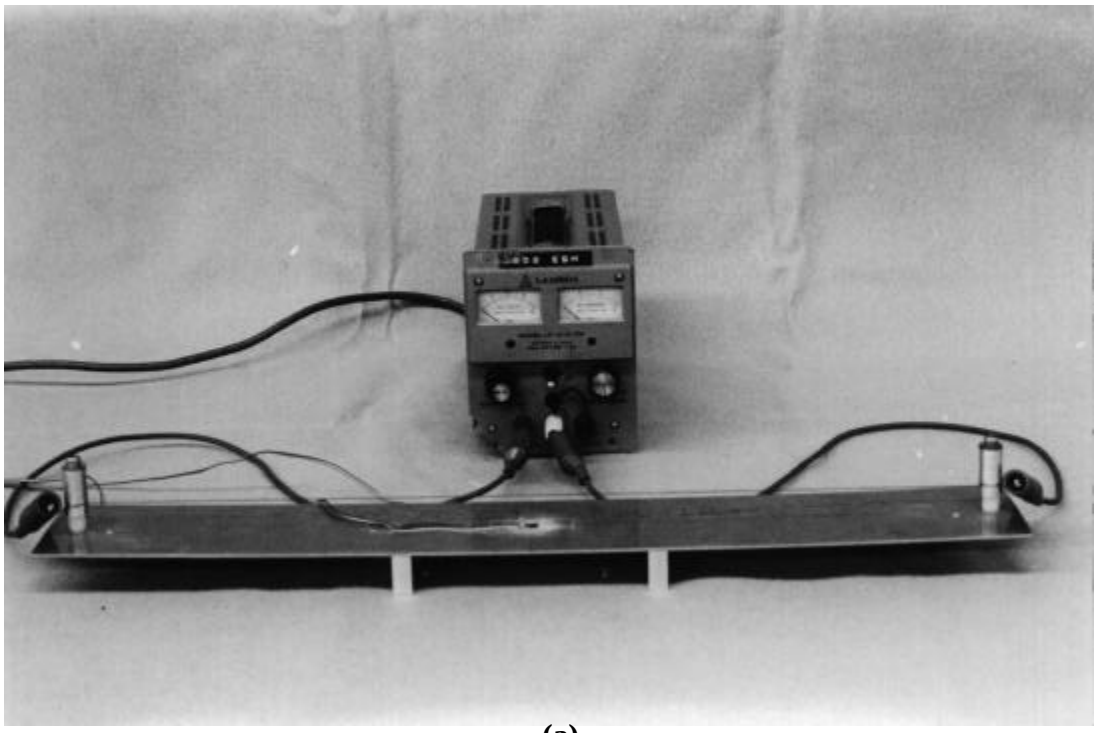

(a)

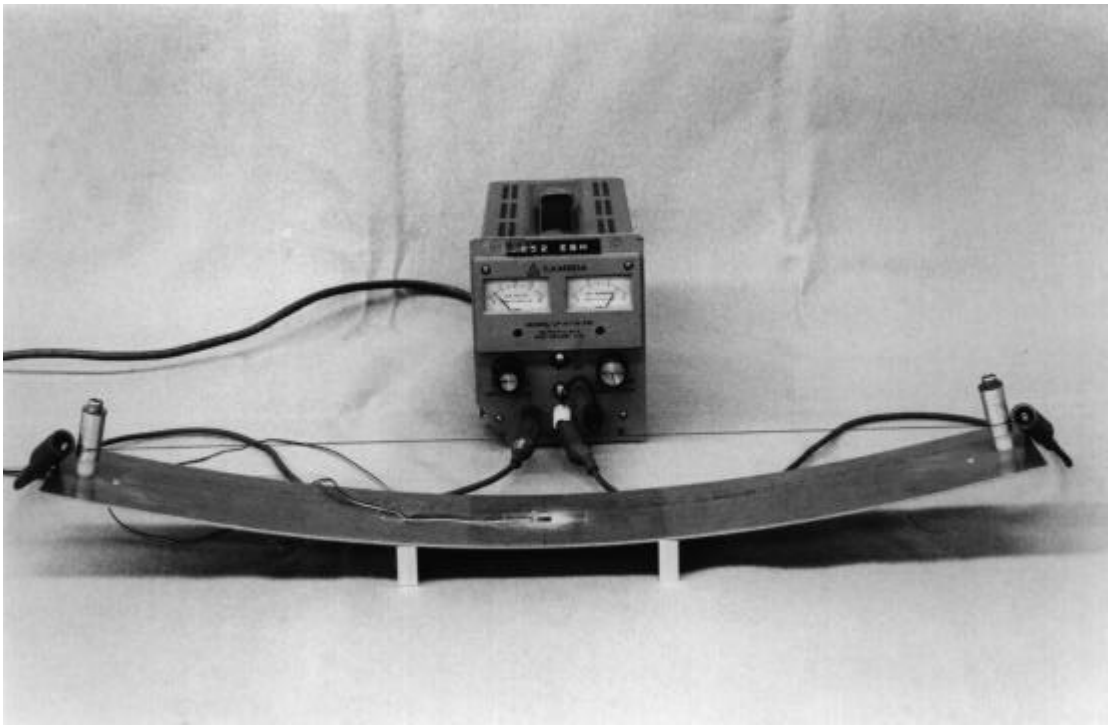

(b)

Fig 5-17. Plate during the experiment: (a) before voltage is applied, (b) after the SMA wire has saturated with strain

Chapter 6 Use of SMAs with unsymmetric laminates

6.1 Preliminary design considerations

When using SMAs with highly curved unsymmetric laminates, several important issues have to be considered. First, the SMA wire should be attached on the laminate close enough to its surface so that the strain needed for recovery to make the laminate snap does not exceed the maximum recovery strain of 8% [31], i. e., ε_o<8%. However, the supports to which the SMA wire is attached should be long enough, i.e., the dimension *e* in Fig. 4-1 (b) large enough, so that the SMA wire does not touch the laminate, as illustrated in Fig. 6-1. The issue is to find a good combination for x_s and *e* which satisfies the strain recovery and the geometric conditions. Since the cross-ply laminate exhibits the largest curvature, this laminate will require the largest SMA strain recovery when compared to the other laminates. Therefore, the $[90_4/0_4]_T$ laminate is a good case for determining the design of the wire support geometry.

The second issue to consider is the force level necessary for snapping. As was seen in Chapter 4, the force level needed for snapping depends on the laminate family and on Θ within the family. Also, as observed during the experiment with the aluminium plate, discussed in Chapter 5, the SMA wires can become saturated with stress. As the $[90_4/0_4]_T$ laminate requires the most force to produce snapping, this laminate can also be used to study force level requirements. Both issues are discussed below.

6.1.1 Geometric considerations

To obtain a geometry for which the SMA wire just touches the laminate, it can be seen from Fig. 6-1 that *e* has to be equal to

$$e = \frac{|a| x_s^2}{2\cos a x_s}. \tag{6.1}$$

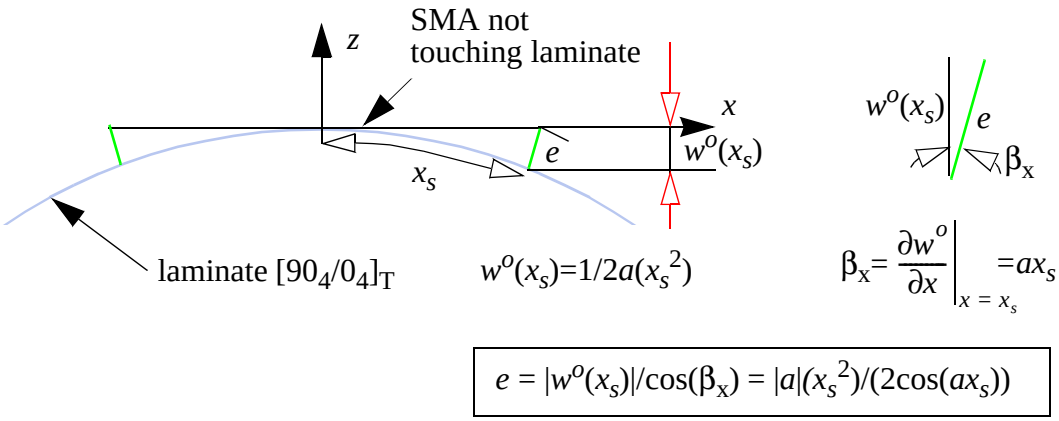

Fig. 6-1. Geometry of SMA wire and support on unsymmetric laminate

Additionally, the SMA wire should be allowed to recover enough strain so that the laminate can reach an unstable configuration thus snap through. For the case of the $[90_4/0_4]_T$ laminate, the unstable shape is a shallow saddle shape. The strain needed to be recovered, noted ε_r, is computed so that the laminate reaches the unstable saddle shape, $a=a_s$ at force level $F=F_s$, as illustrated in Fig. 6-2. Using eq.(5.16), the strain ε_r is given by

$$\varepsilon_r = \frac{L_{SMA} - L^o_{SMA}}{L^o_{SMA}} = \frac{\left|\vec{R}_F(x_S) - \vec{R}_F(-x_S)\right|_{F=F_s}}{\left|\vec{R}_F(x_S) - \vec{R}_F(-x_S)\right|_{F=0}} - 1 \,. \tag{6.2}$$

Fig. 6-2. Computation of the strain in the SMA wire

However, the unstable saddle configuration curvature with force applied (point G on Figs. 4-5, 4-7, and 4-9) is slightly greater than the unstable saddle configuration curvature without force applied (point E on Figs. 4-5, 4-7, and 4-9). Furthermore, the configuration with force applied depends on x_s, e, etc. To have a conservative estimate of necessary recovery strain, the saddle configuration with no force applied is used to compute strains, i.e., the value of a_s used

corresponds to the one of point E in Figs. 4-5, 4-7, and 4-9. Using the conservative estimate of curvature change, using the expression for $\bar{\bar{R}}_F$, eq. (4.8), and substituting e as a function of x_s from eq. (6.1), the strain recovered ε_r in eq. (6.2) can be computed as a function of x_s. The strain ε_r is represented as a function of x_s in Fig. 6-3. According to the figure it appears that the recovered strain does not exceed 5.5% for the range of values that x_s can take ($0<x_s<L_x/2$). Therefore, with L_x equal to approximately 6 in., a choice of 4 in. for x_s will result in a configuration whereby the wire spans a considerable portion of the dimensions of the laminate. By eq. (6.1), this results in e=0.55 in.

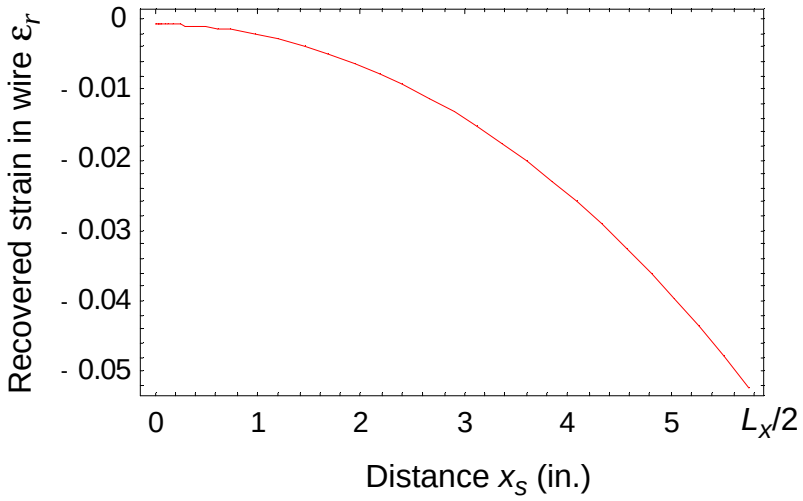

Fig. 6-3. Strain recovered by the SMA wire versus x_s

6.1.2 Force level considerations

From Fig. 4-7, the force required to snap the $[90_4/0_4]_T$ laminate is equal to 45.9 lb. This force is quite large but can be generated by using several SMA wires as opposed to one, as was the case for the narrow plate. Based on the results from that experiment, where a single wire was able to generate about 13 lb, it appears that four SMA wires would be needed to generated a force of 45.9 lb.

In summary then, for the unsymmetric laminates, up to four SMA wires will be used, and the geometry of the supports will be given by

$$\begin{aligned} x_s &= 4.0\,\text{in} \\ e &= 0.55\text{in}\cdot \end{aligned} \tag{6.3}$$

6.2 Modeling the SMA-induced deformations of the $[90_4/0_4]_T$ laminate

The laminate deformations induced by the SMA wires are computed using the same iterative process as described previously. The computations are performed using the properties for the laminate and the SMA wire given, respectively, by eqs. (2. 22) and (5.18), except the SMA wire area which is taken to be four times larger than the one used in the narrow aluminum pate computation to account for the use of four wires instead of one. Thus,

$$A_{SMA} = 4\left(\frac{\pi D^2}{4}\right). \tag{6.4}$$

The results are represented in Figs. 6-4 and 6-5 in the form of the curvature of the laminate and the actuated force versus the temperature in the SMA wire. As can be observed in the figures, the SMA wire has to be heated above 52 ^{o}C to generate enough force ($F \geq 46.9$ lb) to make the laminate snap. Note in Fig. 6-5 that the force actuated by the SMA wires is well below the level given by the upper critical force line.

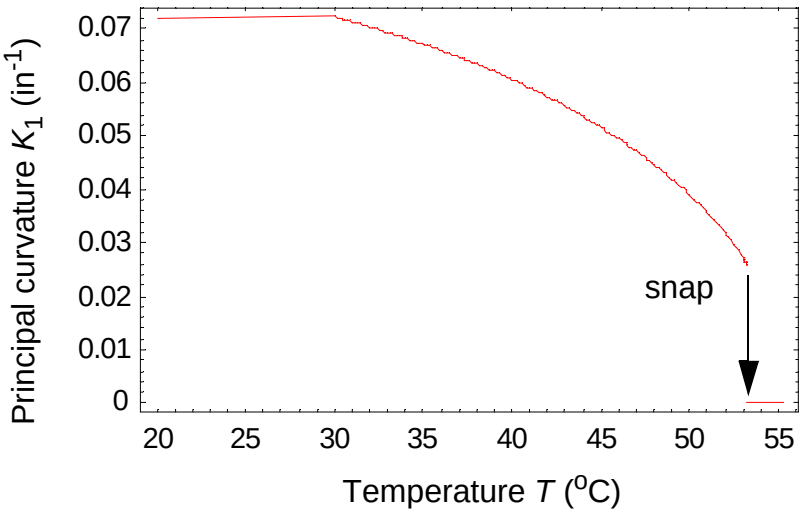

Fig. 6-4. Curvature-SMA wire temperature relation: $[90_4/0_4]_T$ laminate

Considering the total strain in the wire represented in Fig. 6-6, it is interesting to observe that the SMA wire has only to recover a small amount of strain to make the laminate snap.

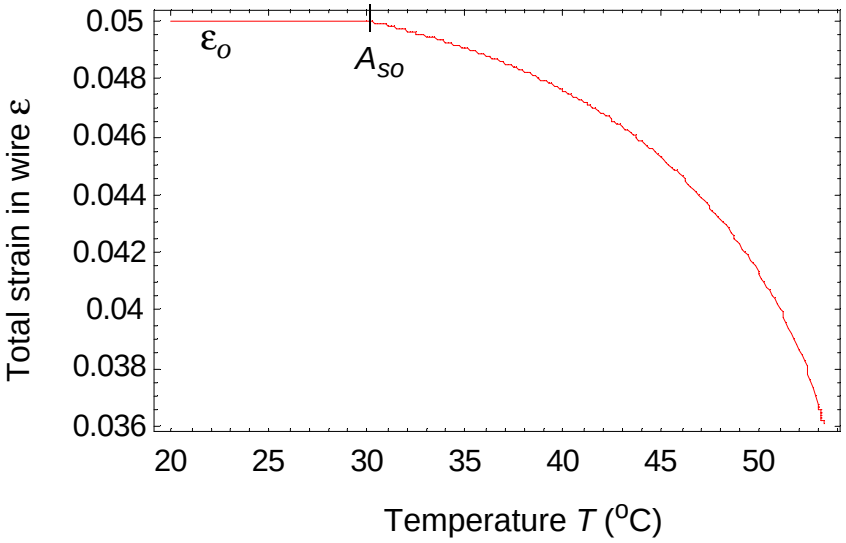

Fig. 6-5. Total strain-temperature relation: $[90_4/0_4]_T$ laminate

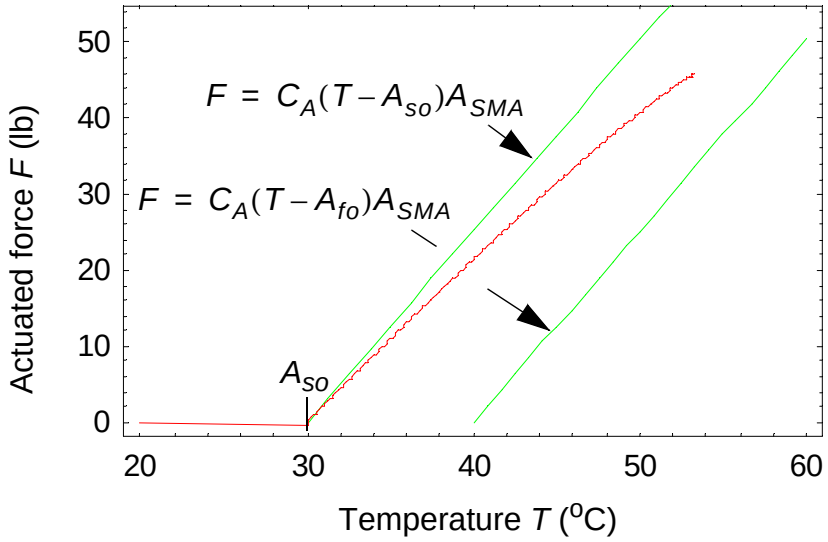

Fig. 6-6. Actuated force-SMA wire temperature relation

Based on these results obtained for the cross-ply $[90_4/0_4]_T$ laminate, and given that this particular laminate requires the largest SMA strain recovery and SMA-actuated force level, it seems that using SMA wires to change the configuration of the other unsymmetric laminates should be successful.

6.3 Modeling the SMA-induced deformations of general unsymmetric laminates

6.3.1 Design considerations

Since the set-up geometry chosen for the $[90_4/0_4]_T$ laminate, eqs. (6.3), leads to satisfactory results, the values for e and x_s are kept the same for the other unsymmetric laminates considered. The area of the SMA wire can be changed according to the number of wires required to snap the laminate. Table 6-1 outlines for each laminate what force level the SMA wire has to induce, and how many wires should be used to produce that force.

Family	Lay-Up	Snapping force (lb)	Min. number of wires
$[-\Theta_4/\Theta_4]_T$	$[-15_4/15_4]_T$	11.7	1
	$[-30_4/30_4]_T$	33.5	3
	$[-45_4/45_4]_T$	43.8	4
$[(90-\Theta)_4/\Theta_4]_T$	$[90_4/0_4]_T$	45.9	4
	$[75_4/15_4]_T$	35.0	3
	$[60_4/30_4]_T$	12.2	1
$[(\Theta-90)_4/\Theta_4]_T$	$[-90_4/0_4]_T$	45.9	4
	$[-75_4/15_4]_T$	45.3	4
	$[-60_4/30_4]_T$	44.2	4

Table. 6-1. Determination of the number of SMA wires to be used for each laminate

6.3.2 Theoretical results

The results for each laminate, except the $[90_4/0_4]_T$ which has already been studied, are presented in Fig. 6-7 to 6-13, in the form of the major principal curvature, the actuated force, and the SMA wire total strain versus the temperature in the SMA wire. Reflecting Table 6-1, it is seen from the figures that the smallest force level for snapping, about 12 lb, occurs for the $[-15_4/15_4]_T$

and $[60_4/30_4]_T$ laminates, both of which have 30^o between fiber orientations. The $[90_4/0_4]_T$, discussed previously, and the $[-45_4/45_4]_T$, $[-75_4/15_4]_T$, and $[-60_4/30_4]_T$ laminates require somewhat over 46 lb, all of these laminates having 90^o between fiber orientations. An intermediate level of about 35 lb is required for the $[-30_4/30_4]_T$ and $[75_4/15_4]_T$ laminates, reflecting the 60^o angle between fiber orientations. The total strain in the wire at snapping is nowhere near the maximum recovery level of 8% for any of the laminates, the recovery being not over 2% in all cases. From these figures it seems that it will be possible to design the number of wires and the geometry of the wire supports so that the configuration of unsymmetric laminates can be changed using SMA. There are adequate margins for necessary force levels and recovery strain for the SMA to operate properly and predictably.

The next chapter presents experiments that were conducted to check the accuracy of this model.

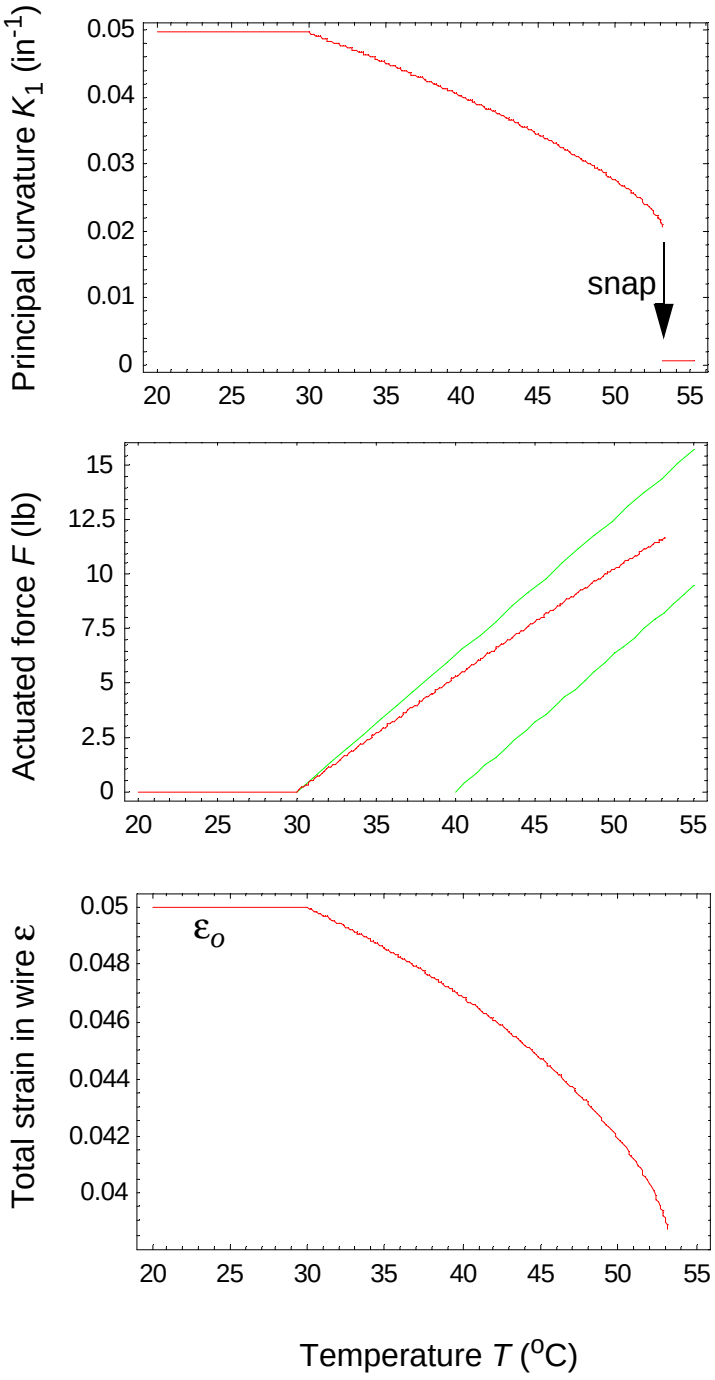

Fig. 6-7. SMA-induced response of the $[-15_4/15_4]_T$ laminate

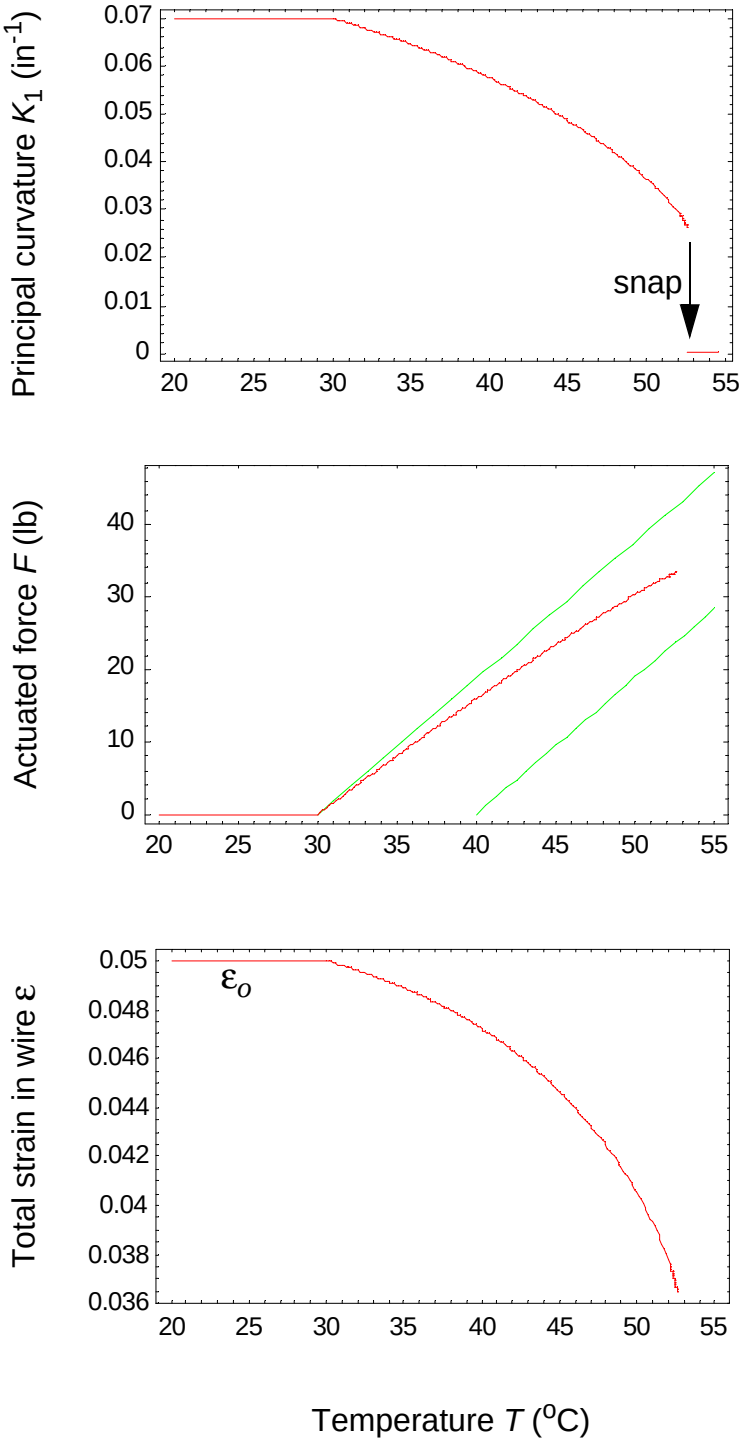

Fig. 6-8. SMA-induced response of the $[-30_4/30_4]_T$ laminate

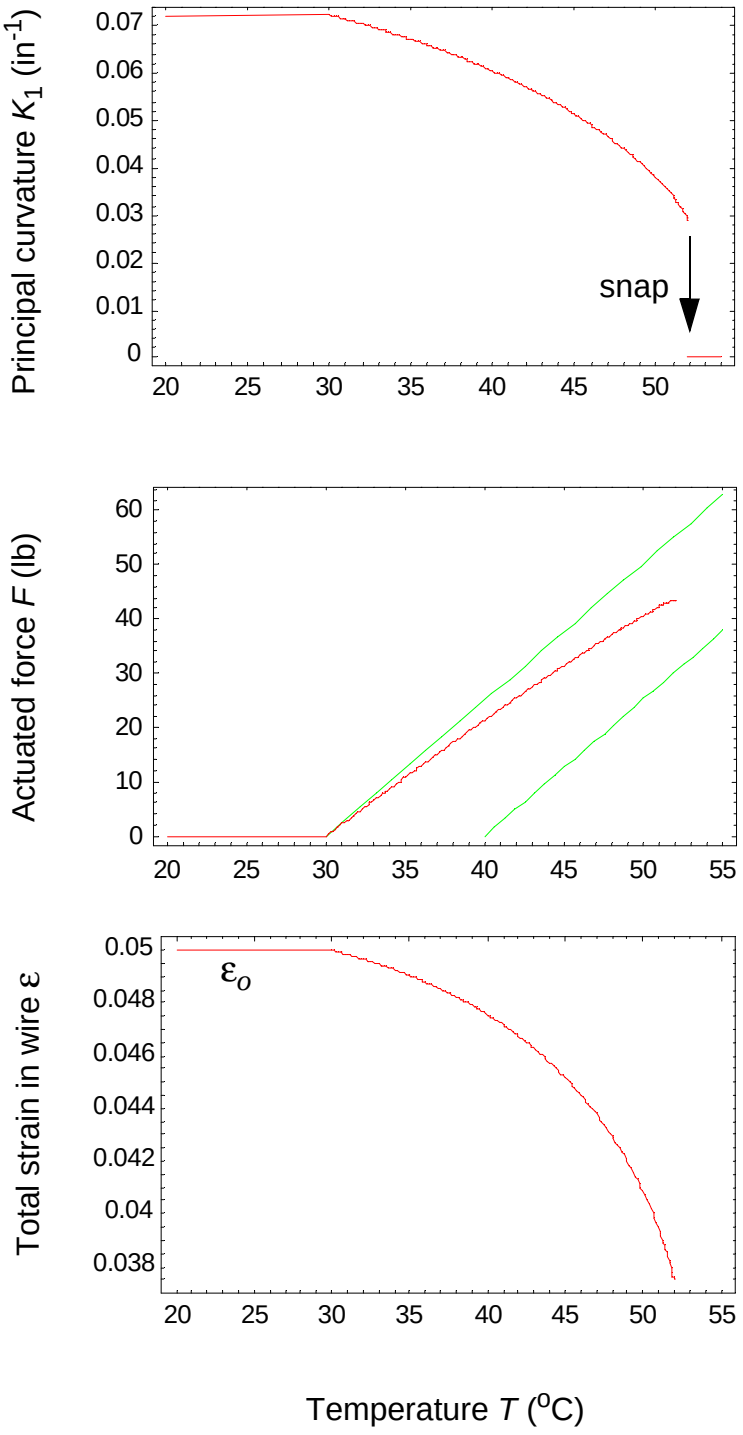

Fig. 6-9. SMA-induced response of the $[-45_4/45_4]_T$ laminate

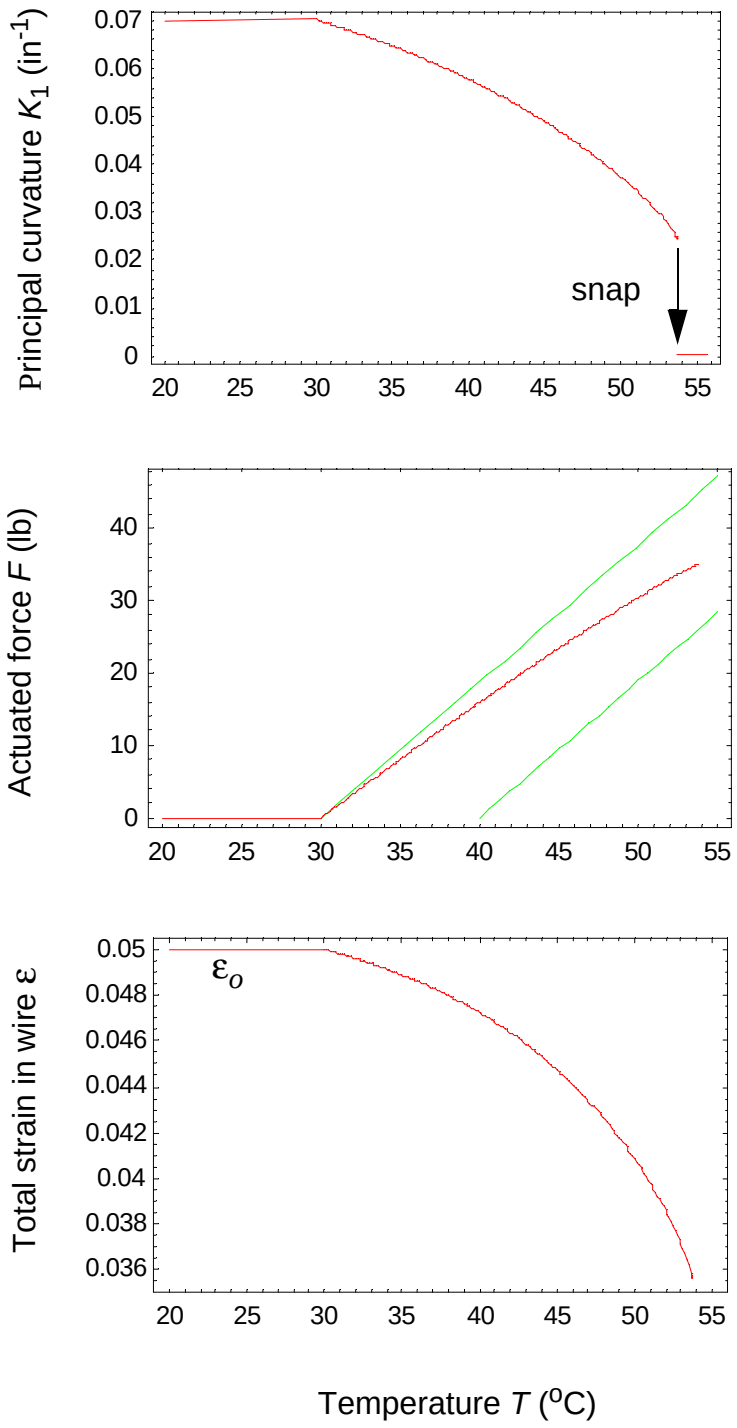

Fig. 6-10. SMA-induced response of the $[75_4/15_4]_T$ laminate

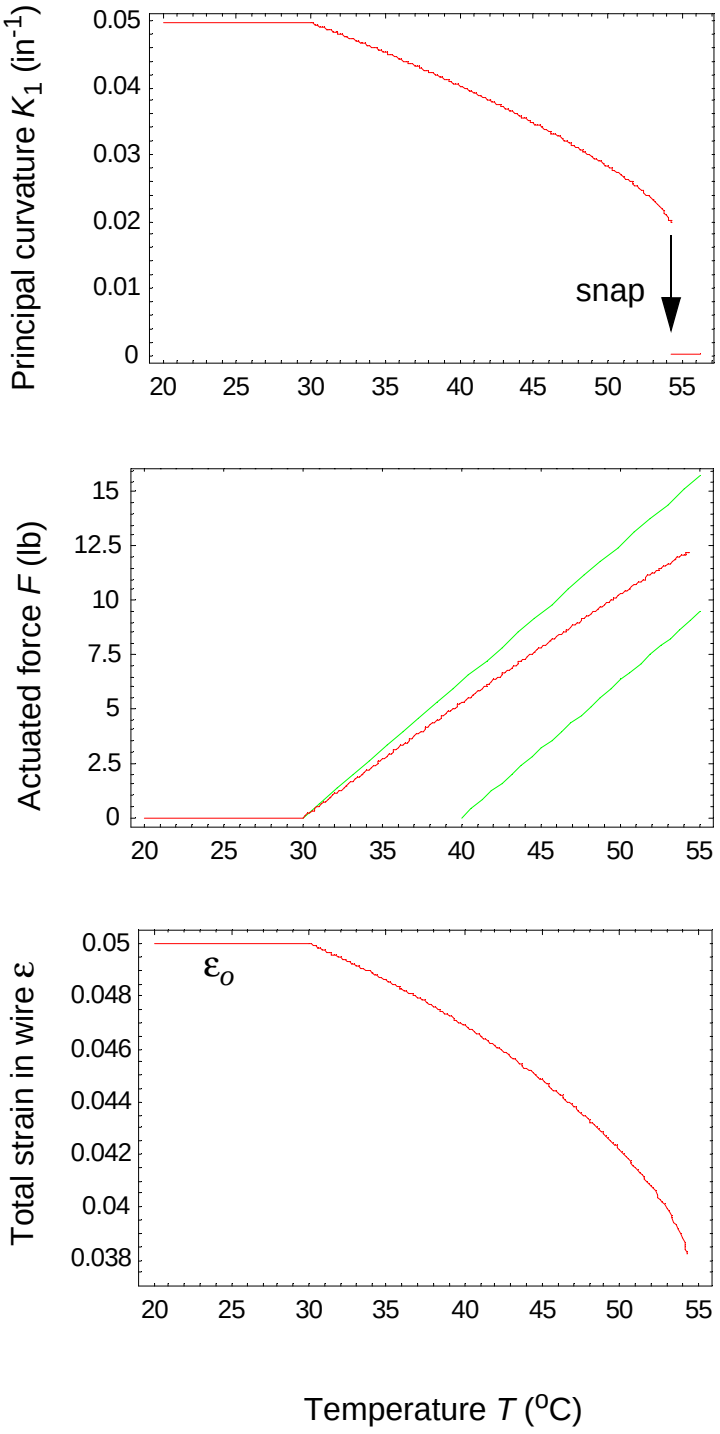

Fig. 6-11. SMA-induced response of the $[60_4/30_4]_T$ laminate

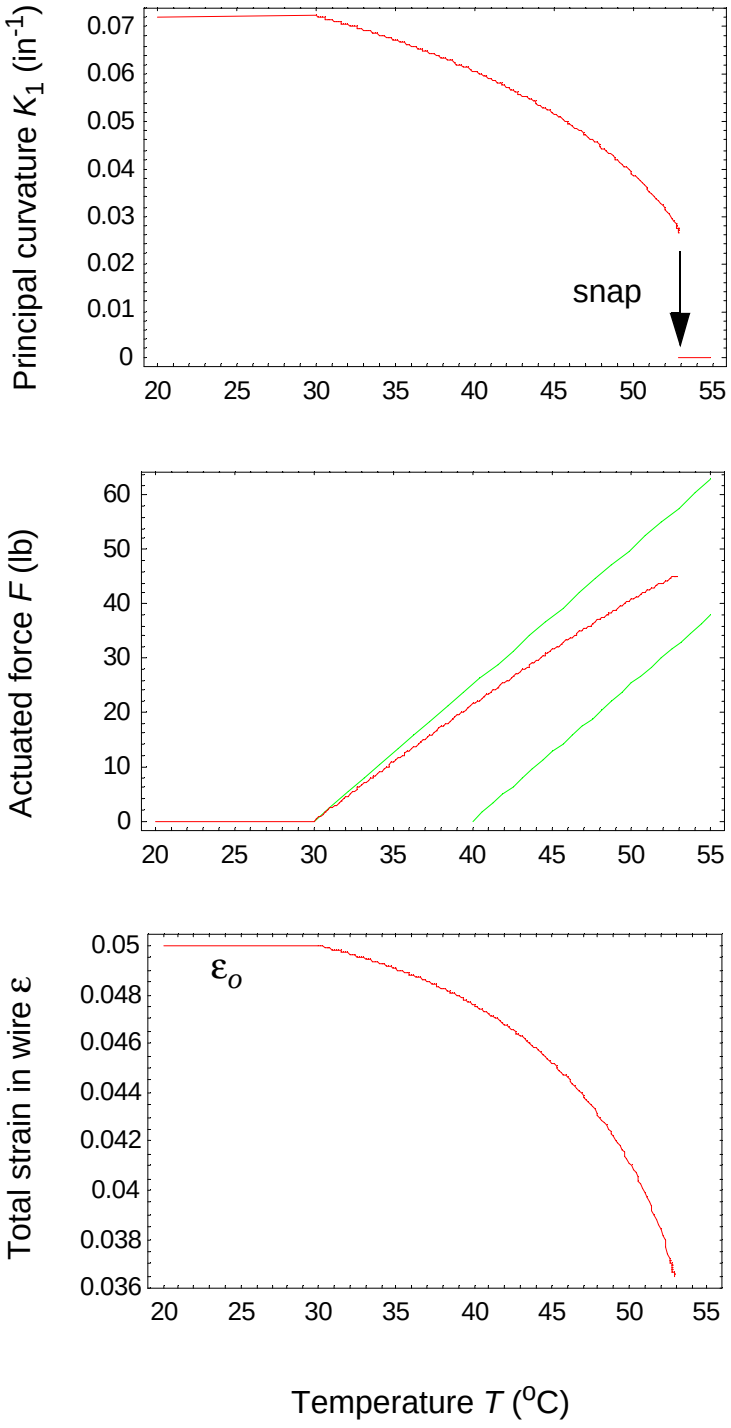

Fig. 6-12. SMA-induced response of the $[-75_4/15_4]_T$ laminate

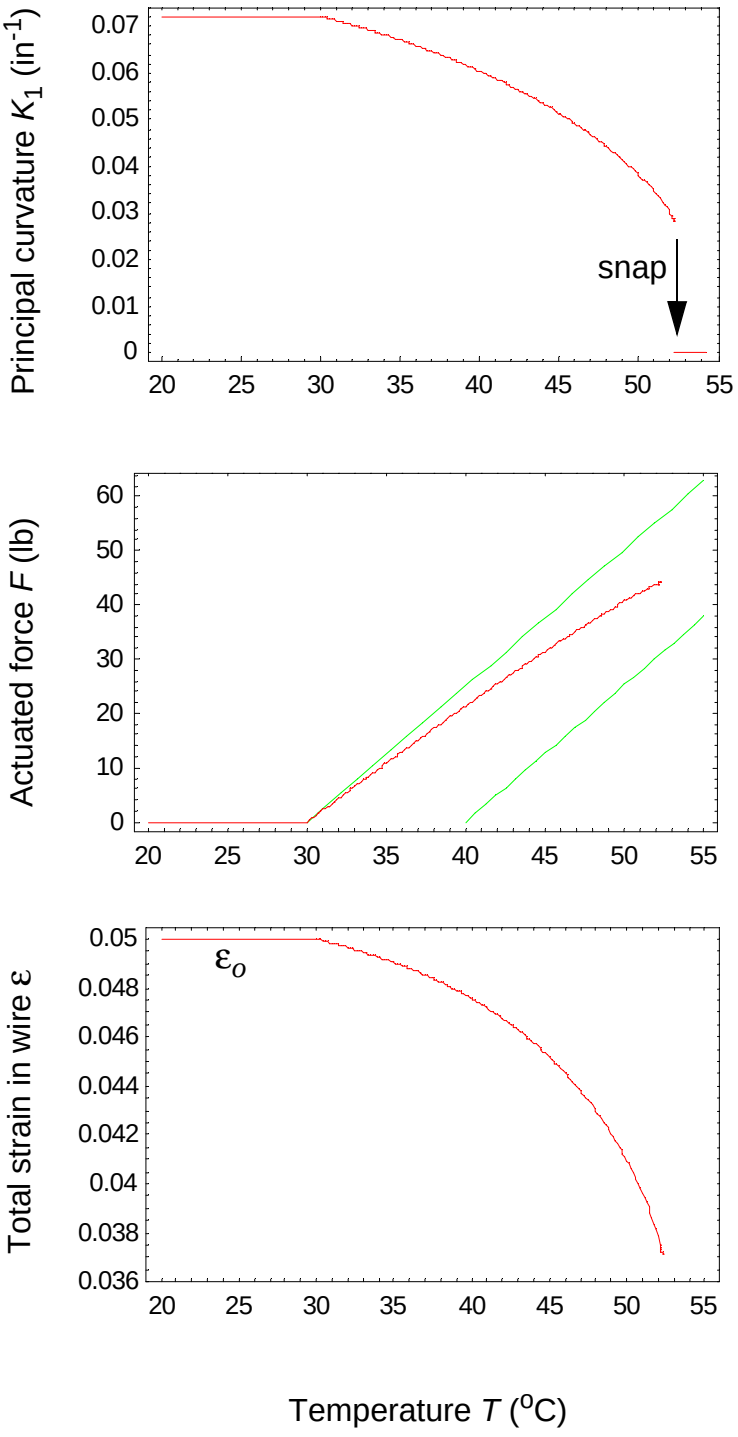

Fig. 6-13. SMA-induced response of the $[-60_4/30_4]_T$ laminate

Chapter 7 Experiments using SMA to induce snap through of unsymmetric laminates

The culmination of the efforts described in the previous chapters was experiments designed to measure the response of unsymmetric laminates forced to change configuration by attached SMA wires. Experiments on one laminate per family, specifically the $[-30_4/30_4]_T$, $[60_4/30_4]_T$, and $[-60_4/30_4]_T$ laminates, were conducted. In addition, the cross-ply laminate $[90_4/0_4]_T$ was also tested. The results of these experiments and correlation with the predictions are described below. Details of the wire attachments and some of the practical issues of working with SMA and unsymmetric laminates are also discussed.

7.1 Preliminary considerations

7.1.1 SMA wire attachment

In Chapter 5 it was discussed that more than one wire was needed to generate the force level required to produce the laminate snap through. To simulate the effects of several wires, a single wire was used, stretched back and forth across the laminate surface between multiple supports, as illustrated in Fig. 7-1 (a). As seen in the figure, there were two types of supports, end supports and sliding supports. The single SMA wire was attached at the end supports but was free to slide around the sliding supports. The forces generated by a wire attached in this fashion were statically equivalent to the ones that several individual wires would produce, as shown in Fig. 7-1 (b). Using configuration (a) over (b) offered the advantage of obtaining a force in the SMA wire which would be uniform along the length of the wire. In configuration (b) the SMA wires would have to be attached with the same initial tension to generate the same force when heated. This could actually be difficult to achieve in practice.

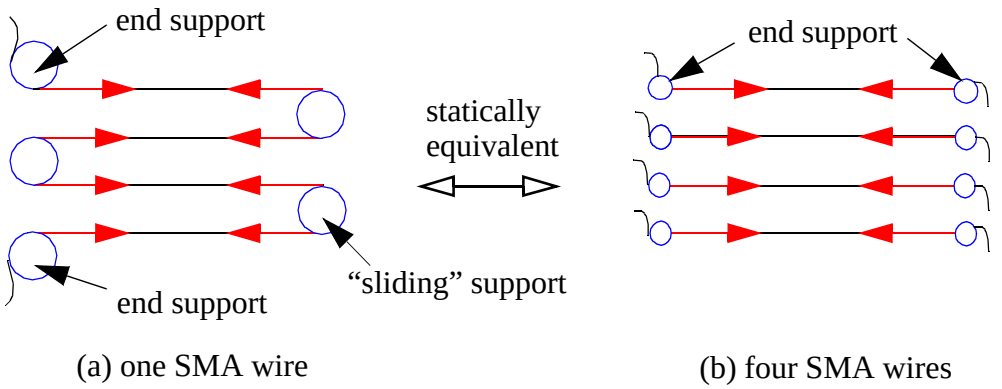

Fig. 7-1. SMA wire attachment

7.1.2 Measurement of the laminate deformations

Another aspect to consider was how to measure the response of the laminate as forces in the SMA wire were generated. In Chapter 5 the laminate response was represented by the change in the principal curvatures and principal curvature direction. However, these variables could not be easily measured directly during the experiment. Rather, it was found more convenient to measure the strains in the laminate to characterize the laminate response. The strains were measured along three different directions, specifically along the x and y axes, and along the axis oriented at 45^o from the x axis. Back-to-back gages were used. With this arrangement, the strains in any direction, e. g., the principal curvature directions, could be computed as a function of SMA wire temperature.

7.2 Description of experiments

7.2.1 Strain gage locations and details regarding the supports and the thermocouples

Six back-to-back strains gages were bonded on the laminate surfaces along the three different directions, as illustrated in Fig. 7-2. The gages were positioned to be as close as possible to the center of the laminate center. Supports were fastened to the top surface of the laminate. A different support configuration had to be used for each laminate since the number and location of supports depended on the laminate principal curvature direction Φ_o and the laminate snapping force level F_s. Figure 7-3 depicts the support configuration that was selected for each laminate. Note that for the $[-30_4/30_4]_T$ and $[60_4/30_4]_T$ laminates the support configuration simulated the

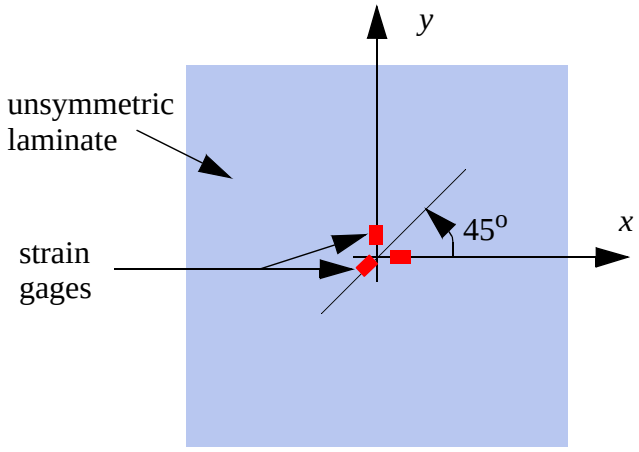

Fig. 7-2. Strain gage orientations

effect of, respectively, two and four SMA wires, whereas it was discussed in Chapter 6 that, respectively, one and three wires were enough. It was found to be more convenient to use a configuration simulating the effect of an even number of wires. Note also the similarity of Fig. 7-3 and Figs. 2-7, 2-8, and 2-9.

The distance between two adjacent supports, denoted d in the figure, and the distance between two opposite supports, denoted L, were the same for all laminates. Distance L was chosen to be equal to 8 in. according to the design considerations stated in Chapter 6, eq. (6.3). As illustrated in Fig. 7-4, distance d was computed from the radius of the support, denoted r_s, and was equal to 0.75 in.

It should be mentioned that the supports were fabricated from aluminium, an electrically conducting material. The SMA wires were attached directly to the supports with no electrical insulation.The carbon fibers in the laminates were also electrically conducting. To prevent any unwanted electrical effects, the supports were attached to the laminates with nylon screws, and a nylon washer was used between the base of the support and the laminate, as illustrated in Fig. 7-5.

Before being attached to the supports, the SMA wire was elongated plastically to generate a 5% initial strain, and unloaded. The wire was then attached to one end support, around the sliding supports, and back to the other end support, as was illustrated in Fig. 7-1. Finally, the ends of the SMA wire were connected to a power supply and two thermocouples were taped on the SMA wire. Since the SMA wires were electrically conductive and the thermocouple wires were electrically conductive, the thermocouple was electrically insulated from the wire with a small piece of cellophane tape. It is feared there could be some thermal insulation effect from the tape and the thermocouple would not measure exactly the SMA wire temperature. However, electrical isolation was important.

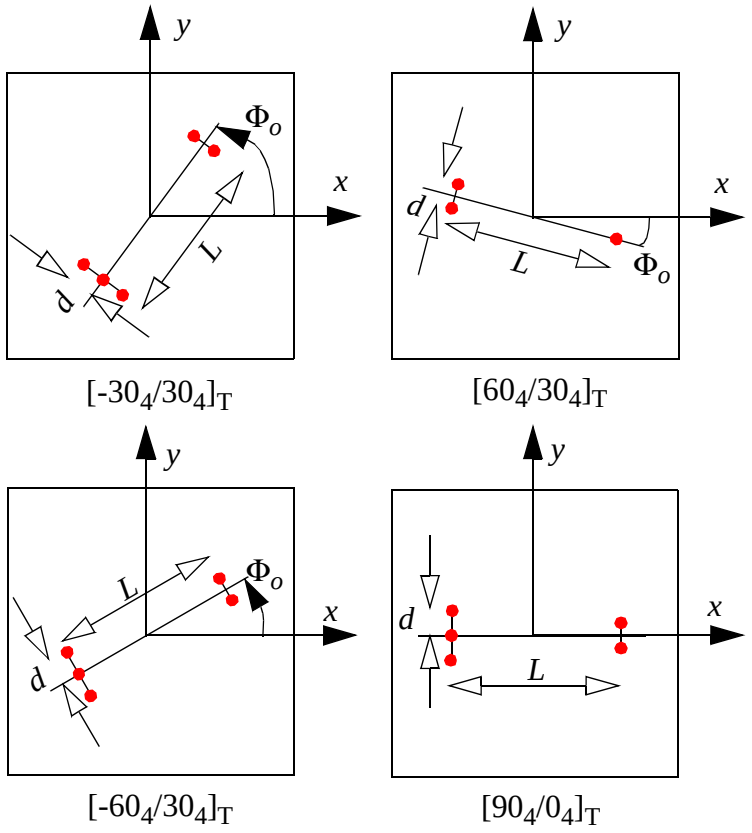

Fig. 7-3. General configuration of the supports

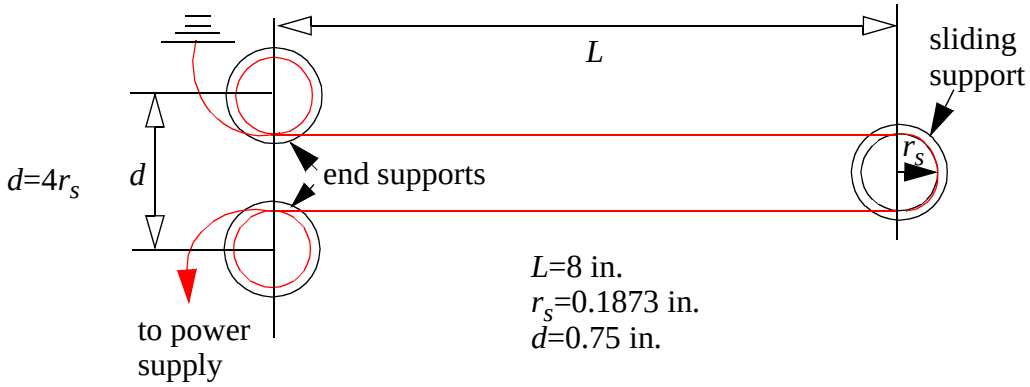

Fig. 7-4. Definition of the support geometry

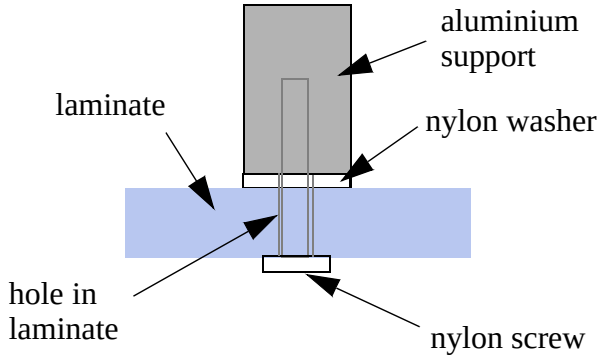

Fig. 7-5. Details of attachment of supports to the laminate

7.2.2 Experimental measurements

The six strains gages and one of the two thermocouples were connected to a data acquisition system, programed to record the strains and temperature every 60 milliseconds. The second thermocouple was read manually at regular intervals during the experiment. The voltage in the SMA wire was increased gradually using small voltage increments. Between each voltage increment it was necessary to allow some time for the thermocouples and the strain gages to stabilize. The experiments on each of the four laminates, specifically the $[-30_4/30_4]_T$, $[60_4/30_4]_T$, $[-60_4/30_4]_T$, and $[90_4/0_4]_T$, laminates were conducted twice to assess repeatability of results. Results from both sets of measurements are shown.

7.3 Presentation of the results

The experimental results obtained for each of the four laminates are presented in Figs. 7-6 to 7-17. For each laminate, the two sets of measurements are depicted in the form of the strains in the laminate and the temperature in the wire versus time. Also, the results from the two experiments are compared by illustrating the laminate strains as a function of the temperature in the wire. The strains along the *x*, *y*, and 45^o axes are denoted in the figures respectively by, ε_0, ε_{90}, and ε_{45}. When examining the figures it can be noticed that some strain measurements are more noisy than others. However in some cases the strains may seem more noisy because of the scale, as the scale is not the same for all the plots. Also, the strains in the laminate are generally not equal to zero before the wire is heated. The strain gages were calibrated before the supports and

the wire were attached to the laminate. Screwing the supports on the laminate created some initial strain in the laminate. In addition, the SMA wire was fastened to the supports under a small initial tension to prevent it from being slack. The combined effects of the attachment of the supports and the SMA wire caused initial strains in the laminate. It can also be noticed in the figures that the temperature measurements are not as smooth as the strain measurements. This difference is due to the resolution of the data acquisition system, which was limited to 2.5 mV. This resolution was not high enough to obtain smooth data for the temperature, since the range for the output voltage of the thermocouple was small, i. e., about 80 mV. On the other hand, since the output voltage for the strain gages ranged from about 0.5 V to up to 1.8 V, the data acquisition system was able to record the strains in a smoother fashion. To obtain a smooth representation of the strains versus the temperature, the data for the temperature were smoothed by using *Mathematica* to perform a convolution on the temperature data. (For more details, see section 3.8 entitled *Numerical Operations on Data* in the Mathematica manual [33]). In the figures to follow, the smoothed data are presented by the continuous line drawn over the original measurements. The triangles in the figures represent the temperature recorded manually using the second thermocouple.

$[-30_4/30_4]_T$ laminate

As can be observed in Figs. 7-6 and 7-7, for the $[-30_4/30_4]_T$ laminate the strains increase at a very slow rate, or not at all, as the SMA wire is first heated above room temperature. As the SMA wire is further heated, the rate of increase of the strains changes continuously, reaching its maximum value when the snap through occurs. The snap through is characterized by a sudden jump in the strains to larger values and a small drop of the temperature in the wire. Note that the strain along the 45^o axis, ε_{45}, changes the most before the snap through occurs. This is actually excepted, since the 45^o axis, compared to the *x* and *y* axes, is the closest to the principal curvature direction, along which the strain should undergo the largest increase. Looking at the ε_{45} time-strain relation, it is interesting to observe that this strain increases as soon as the temperature increases a few degrees. Note also that the strains at the top surface ($z=+H/2$) are negative since the top surface is in compression when forces are applied. The strains at the bottom surface ($z=-H/2$) are positive since the bottom surface is in tension during the deformations. After the laminate snaps, it is interesting to note that the strains $\varepsilon_0(+H/2)$ and $\varepsilon_{90}(+H/2)$ at the top surface and the strains $\varepsilon_0(-H/2)$ and $\varepsilon_{90}(-H/2)$ at the bottom surface are, respectively, equal in magnitude. Referring to the time-temperature relations, it can be observed that the temperatures measured by the manually recorded and automatically recorded thermocouples are within half a degree from each other.

Figure 7-8 presents the measurements from the two experiments in the form of the laminate strains versus the wire temperature. As can be noticed, relative to the first heating, the laminate response follows similar trends as the SMA wire is heated a second time. Also, in each heating case, the strains reach the same magnitude before and after the snap through. The major difference is in the magnitude of the temperature in the wire when the snap through occurs. From the first to the second experiments, the temperature at the snap through decreases from 39.8 ^{o}C to 36.8 ^{o}C, a difference of about 3 ^{o}C.

$[60_4/30_4]_T$ laminate

As illustrated in Figs. 7-9 and 7-10, for the $[60_4/30_4]_T$ laminate the response follows the same characteristics as observed for the $[-30_4/30_4]_T$ laminate, i. e., the rate of change of the strains increases with time and then the strains suddenly jump at the snap through to large positive values at the bottom surface, and to large negative values at the top surface. For this laminate the strain ε_0 has the largest change before the snap through. This can be explained by the fact that ε_0 is the strain along the direction which is the closest to the principal curvature direction. It is interesting to observe that the strain at the bottom surface $\varepsilon_{90}(-H/2)$ becomes negative as the temperature in the wire is increased, whereas the two other strains on the bottom surface are positive. However as the snap through occurs, $\varepsilon_{90}(-H/2)$ suddenly changes to a large positive value. After the snap through, note that the strains $\varepsilon_0(+H/2)$, $\varepsilon_{90}(+H/2)$, and $\varepsilon_{45}(+H/2)$ at the top surface are, respectively, similar in magnitude but opposite in sign to the strains $\varepsilon_{90}(-H/2)$, $\varepsilon_0(-H/2)$, and $\varepsilon_{45}(-H/2)$ at the bottom surface. Referring to the time-temperature relation of Fig. 7-9, a small drop in the temperature can be observed as the laminate snaps, as it was the case for the $[-30_4/30_4]_T$ laminate.

The temperature-strains relations obtained from the two experiments are illustrated in Fig. 7-11. As can be observed, the temperature-strains relations correlate very well with one another until the temperature in the wire reaches about 34 ^{o}C. When the wire is heated further, the strains of the experiment conducted the first time increase at a higher rate than the strains of the second experiment. As a result, the snap through in the first experiment occurs at a temperature equal to 35.8 ^{o}C whereas in the second experiment the snap through occurs as the temperature reaches 37.7 ^{o}C. This represents a 2 ^{o}C difference. After the snap through the strains reach similar levels in both experiments.

$[-60_4/30_4]_T$ laminate

The laminate strains and SMA wire temperature versus time for the $[-60_4/30_4]_T$ laminate are illustrated in Figs. 7-12 and 7-13. As observed for the previous laminates, the strains increase at a higher rate as the temperature increases. As the snap through occurs, the strains jump suddenly to reach large values, which are positive for the strains at the bottom surface and negative for the strains at the top surface. The largest strains before the snap through are the strains measured along the 45 ^{o} axis, because this particular axis is the closest to the principal curvature direction. After the snap through it is interesting to note that the strains $\varepsilon_0(+H/2)$ and $\varepsilon_{90}(+H/2)$ at the top surface are equal in magnitude but opposite in sign to, respectively, the strains $\varepsilon_{90}(-H/2)$ and $\varepsilon_0(-H/2)$ at the bottom surface. Referring to the time-temperature relations, a small drop in the temperature right after the snap through can be again noticed.

The temperature-strain relations obtained for the two experiments are illustrated together in Fig. 7-14. From the figure it can be observed that the initial strain is not exactly the same for both experiments. This is probably due to a difference in the tension applied on the SMA wire as the wire was attached to the supports. However, the general trends are the same. The temperature at the snap through is different by about 2 ^{o}C, being equal to 43.4 ^{o}C in the first experiment and to

41.1 ^{o}C in the second. This is quite good given that the initial conditions were not exactly identical.

$[90_4/0_4]_T$ laminate

The strains and temperature measured versus time for the $[90_4/0_4]_T$ laminate are presented in Figs. 7-15 and 7-16. As observed previously for the other laminates, the strains ε_0 and ε_{45} increase at a higher rate as the SMA wire is heated. The strain ε_0 is the strain which undergoes the largest increase, since the *x* axis is the principal curvature direction for that laminate. The strain in the *y* direction, ε_{90}, has an interesting behavior before the snap through. At the top surface ε_{90} increases slightly at first to take a small positive value, and then decreases back to about zero before jumping suddenly to a large negative value at the snap through. On the other hand, at the bottom surface, ε_{90} decreases slightly to reach a small negative value, and then jumps to a large positive value at the snap through. The evolution of the ε_{90} strain seems to indicate that a small anticlastic curvature may be developing along the *y* direction as the forces are applied along the *x* direction. As observed previously for the other laminates, after the snap through the strains at the top surface are negative since the laminate top surface is under compression, and the strains at the bottom surface are positive since the laminate bottom surface is under tension. In particular, the strains $\varepsilon_0(+H/2)$ and $\varepsilon_{90}(+H/2)$ are equal but opposite in sign to, respectively, the strains $\varepsilon_{90}(-H/2)$ and $\varepsilon_0(-H/2)$. Referring to the time-temperature relation, a small drop in the temperature can be observed as the laminate snaps.

Looking at Fig. 7-17, it is striking how well the data from both experiments correlate. The only difference lies, as observed for the other laminates, in the temperature at which the laminate snaps. For the first experiment this temperature is equal to 41.7 ^{o}C whereas it was equal to 41 ^{o}C for the second experiment, a difference of 0.7 ^{o}C.

These experimental results show that the response of the laminate is very similar from the first to the second experiments, for all the laminates that were tested. Also it can be noticed in the figures that for all laminates the strains in the laminate are changing as soon as the temperature in the SMA wire increases above room temperature. This was, in fact, not expected since the austenite start temperature had been determined to be 30 ^{o}C in Chapter 5. Since the strains start to change before the temperature in the wire has reached 30 ^{o}C, it is probable that the austenite start temperature has decreased since the time the SMA wire was calibrated. This issue is discussed in detail in the next section.

7.4 Issues on predicting the measured laminate response

7.4.1 Change in the thermal properties of the SMA wire

Thermal properties of SMAs, especially the phase transformation temperatures, can

influence greatly the shape recovery process by governing the phase transformation occurrence. Thus, the accuracy of the model predictions depends strongly on the precision with which the phase transformation properties can be determined. Since the austenite start transformation temperature is suspected to have changed over the course of the experiments, a period of about 6 months, the experiment on the narrow aluminium plate was conducted a second time, after all the experiments on the unsymmetric laminates were finished. The results of this experiment are presented by the diamonds shapes in Fig. 7-18 in the form of the strains measured at the top and bottom surfaces of the plate as a function of the temperature measured in the SMA wire. Results from the original experiment are depicted by the triangles. As can be observed, the major differences occur at the beginning of the phase transformation. It seems that the austenitic transformation was initiated at a temperature that was lower in the second experiment than it was in the original experiment. The phase transformation the second time began as soon as the SMA wire was heated above 25 ^{o}C, whereas earlier the wire had to be heated above 30 ^{o}C to initiate the phase transformation. From these observations, it seems that the austenite start temperature, A_{so}, decreased from 30 ^{o}C to 25 ^{o}C with time and repeated usage of the SMA wire. After the temperature in the SMA wire reaches about 45 ^{o}C, the two sets of experimental results correlate well. The austenite finish temperature, A_{fo}, does not seem to have changed from the original experiment to the second. Predictions from the model are also illustrated in the figure. The dashed line and the full line represent, respectively, the model predictions using A_{so}=30 ^{o}C and A_{so}=25 ^{o}C, A_{fo} being equal to 38 ^{o}C in both cases. It is obvious that the full line captures better than the dashed line the experimental data from the second experiment. To further demonstrate the change in the start austenite temperature, results from an experiment which was conducted on the $[90_4/0_4]_T$ laminate right after the original experiment on the narrow aluminium plate are presented. During that experiment, a different data acquisition system was used to record the strains in the *x* direction at the top and bottom surfaces of the laminate, and the temperature in the SMA wire. The results of that original experiment are presented in Fig. 7-19 in the form of the strain along the *x* direction, ε_0, and the temperature in the wire versus time. In addition, the strains ε_0 are depicted as a function of the temperature in the wire in Fig. 7-20. The strains ε_0 measured during the later experiments and presented in Fig. 7-17 are also presented in the figure. It is interesting to note that the strains from the two later experiments increase with temperature in a very different manner when compared to the original experiment. During the original experiment the wire needed to be heated above 30 ^{o}C to begin to induce an increase of the strains. During the two later experiments, the strains increased as soon as the temperature in the wire was above 25 ^{o}C. It seems that the austenite transformation during the original experiment started to occur at a temperature which was higher than the temperature at which the phase transformation started in the two later experiments. Since the phase transformation started at a more elevated temperature in the original experiment, the wire needed to reach a higher temperature to generate enough force to make the laminate snap. Thus, in the original experiment the laminate snapped as the temperature reached about 48 ^{o}C, whereas the snap through was activated in the later experiments as the temperature reached about 41 ^{o}C. From these observations, it appears that the thermal properties of the SMA wire may have changed relative to the time when the wire was calibrated during the original experiments with the narrow aluminium plate.

In Fig. 7-21 the original temperature-strain relations from Fig. 7-20 are represented along

with the predictions from the developed theory using A_{so}=30 ^{o}C. As can be observed, the measured strain levels correlate fairly well with the predicted strains and the occurrence of the snap through is predicted quite accurately. However, the measured strains increase at slower rate than predicted.

Hence, because of the differences in results between the original experiments and the later experiments, with both the narrow aluminium plate and the $[90_4/0_4]_T$ unsymmetric laminate, further numerical calculations will use the lower value of A_{so}, specifically, 25 ^{o}C.

7.4.2 Relaxation effects in the laminates and initial forces

Another important aspect to consider when using the developed theory to predict the laminate response to SMA-induced force is the fact that the laminate curvatures decreased since the time they were cured, as was discussed in Chapter 3. The decrease was presumably due to relaxation effects in the epoxy matrix. The decrease in the laminate curvatures may have an important influence on the laminate response as forces are applied. In particular, a decrease of the snapping force would be expected. This would mean that the SMA wire may not need to be heated to the temperatures predicted in Chapter 6.

In order to obtain predictions that reflect as much as possible the actual SMA-induced deformations in the laminate, the developed theory should ideally predict quite accurately the initial laminate curvatures when no force is applied. If the predicted initial curvatures do not correlate well, the SMA-induced deformations are unlikely to be predicted accurately. In order to obtain valid predicted curvatures, the temperature change ΔT was decreased from its initial -280 ^{o}F to reflect relaxation effects. The value of ΔT which was used for each laminate and the changes it made in the predicted curvature and the snapping force magnitudes are presented in Table 7-1. Table 7-1 also presents the laminate curvatures that were measured just after cure and then again after a six-month period.

As can be observed from Table 7-1, for the $[-30_4/30_4]_T$, $[60_4/30_4]_T$, $[-60_4/30_4]_T$, and $[90_4/0_4]_T$ laminates, the temperature change has to be changed to, respectively, -236 ^{o}F, -197 ^{o}F, -235 ^{o}F and -239 ^{o}F to obtain good correlations between the predicted and measured initial curvatures. For the $[60_4/30_4]_T$ laminate the magnitude of the temperature change has to be decreased more than for the other laminates because even just after cure the curvatures of the laminate were already smaller than the predicted curvatures computed using ΔT=-280 ^{o}F. For the other three laminates the curvatures just after cure were very close to the predicted curvatures computed using ΔT=-280 ^{o}F. Thus, for the $[60_4/30_4]_T$ laminate the temperature change has to decrease as low as -197 ^{o}F to account for the difference in the curvatures right after cure in addition to the relaxation effects. Decreasing the magnitude of the temperature change affects the response of the laminate to applied forces by, especially, decreasing the level of the snapping force as observed in Table 7-1.

Laminate	Measured curvatures (in^{-1})		ΔT=-280 ^{o}F		New ΔT		
	Just after cure	After 6 months	Predicted curvatures (in^{-1})	Predicted F_s (lb)	ΔT (^{o}F)	Predicted curvatures (in^{-1})	Predicted F_s (lb)
$[-30_4/30_4]_T$	κ_x^o =0.0236 κ_y^o =0.0385 κ_{xy}^o=0.0603	κ_x^o =0.0224 κ_y^o =0.0364 κ_{xy}^o=0.0573	κ_x^o =0.0246 κ_y^o =0.0452 κ_{xy}^o=0.0672	33.5	-236	κ_x^o =0.0207 κ_y^o =0.0379 κ_{xy}^o=0.0566	25.2
$[60_4/30_4]_T$	κ_x^o =0.0399 κ_y^o =5.6 10^{-4} κ_{xy}^o=-0.0181	κ_x^o =0.0322 κ_y^o =-5.6 10^{-4} κ_{xy}^o=-0.0123	κ_x^o =0.0463 κ_y^o =2.9 10^{-3} κ_{xy}^o=-0.0251	12.2	-197	κ_x^o =0.0232 κ_y^o =1.7 10^{-3} κ_{xy}^o=-0.0173	6.5
$[-60_4/30_4]_T$	κ_x^o =0.0539 κ_y^o =0.0188 κ_{xy}^o=0.0659	κ_x^o =0.0454 κ_y^o =0.0150 κ_{xy}^o=0.0528	κ_x^o =0.0540 κ_y^o =0.0178 κ_{xy}^o=0.0627	44.2	-235	κ_x^o =0.0453 κ_y^o =0.0149 κ_{xy}^o=0.0526	33.7
$[90_4/0_4]_T$	κ_x^o =0.0719 κ_y^o =-3.5 10^{-4} κ_{xy}^o=-3.0 10^{-4}	κ_x^o =0.0619 κ_y^o =-2.6 10^{-4} κ_{xy}^o=2.4 10^{-4}	κ_x^o =0.0723 κ_y^o =-1.4 10^{-4} κ_{xy}^o=0.0	45.9	-239	κ_x^o =0.0616 κ_y^o =-1.6 10^{-4} κ_{xy}^o=0.0	36.2

Table. 7-1. Effect of changing ΔT on the predictions of the laminate curvatures and snapping forces

Another aspect to consider in computing the predictions is the fact that during the experiments, a small initial force was applied on the laminate, as was observed in Figs.7-6 to 7-17, to prevent the SMA wire from being slack. This initial force was evaluated using the measured initial strains and was taken into account in the SMA model by adding an initial stress in the equations.

7.5 Comparisons of the experimental results with the predictions of the developed theory

The theory presented in Chapters 4 and 5 is used to obtain predictions of the strains at the laminate surfaces as a function of the temperature in the SMA wire for the four laminates that were tested. In this section, the strain predictions from the theory are compared with the experimental results just presented. The predicted strains in the x and y directions, $\varepsilon_0(z)$ and

$\varepsilon_{90}(z)$, are simply equal to, respectively, $\varepsilon_x(z)$ and $\varepsilon_y(z)$, which were defined in Chapter 2 by eq. (2.2). The predicted strain along the 45^o axis was computed using a standard strain transformation equation given by

$$\varepsilon_{45}(z) = \frac{\varepsilon_x(z) + \varepsilon_y(z)}{2} + \frac{\varepsilon_x(z) - \varepsilon_y(z)}{2}\cos(2(45^o)) + \frac{\gamma_{xy}(z)}{2}\sin(2(45^o)), \tag{7.5}$$

where $\gamma_{xy}(z)$ was defined in eq. (2.2). In the definitions of the strains $\varepsilon_0(z)$, $\varepsilon_{90}(z)$, and $\varepsilon_{45}(z)$, z is set equal to $+H/2$ for the computation of the strains at the top surface and is set equal to $-H/2$ for the computation of the strains at the bottom surface.

The predicted and measured wire temperature-laminate strain relations are presented for the four laminates in Figs. 7-22 to 7-25.

$[-30_4/30_4]_T$ laminate

As can be observed from Fig. 7-22, the predicted and measured strains for the $[-30_4/30_4]_T$ laminate follow the same trends. The magnitudes of the strains before and after the snap through correlate well. The temperature at which the snap through occurs is also quite close. However, some differences can be noticed as the wire is heated above room temperature. The measured strains increase at a much slower rate than the predicted strains. As the laminate approaches the snap through, however, the increase is much more rapid for the measured strains than it is for the predicted strains.

$[60_4/30_4]_T$ laminate

The predicted and measured wire temperature versus laminate strain relations for the $[60_4/30_4]_T$ laminate are presented in Fig. 7-23. It can be observed in the figure that the overall deformation behavior is captured by the theory. However, the strain levels before and after snap through do not correlate as well as for the previous laminate. The predicted snap-through strains are smaller than the measured strains along the x and 45^o axes. Along the y axis the correlation between the measured and predicted snap-through strains is better, but the negative values that the $\varepsilon_{90}(-H/2)$ takes before the snap through are not captured by the model.

$[-60_4/30_4]_T$ laminate

The predicted and measured strains for the $[-60_4/30_4]_T$ laminate are presented in Fig. 7-24. The predicted and measured strains follow similar trends, but the measured strains increase at a smaller rate than the predicted strains do as the temperature increases. The predictions for the temperature associated with the snap through are quite accurate. The temperatures at which the laminate snapped during the experiments are within the range of temperatures determined by the predictions. Note that the measured strains before the snap through are smaller than the predicted strains, but after the snap through the measured strains and predicted strains correlate well.

$[90_4/0_4]_T$ laminate

Figure 7-25 presents the response of the $[90_4/0_4]_T$ laminate which was measured during the two later experiments and the response predicted by the model. Referring to the figure, the overall response of the laminate is predicted quite accurately. Except for $\varepsilon_0(+H/2)$ after snapping, the strain levels before and after the snap through are well predicted. Note that the small relative decrease of the strain ε_{90} before the snap through is captured by the model at the bottom surface, but not at the top surface.

7.6 Observations and concluding remarks

A SMA wire was successfully used to change the configuration of four unsymmetric laminates. Each laminate was tested twice and the results from both experiments correlated well for all laminates. It is excepted that similar results would have been obtained with the remaining four laminates, i. e., the $[-15_4/15_4]_T$, $[-45_4/45_4]_T$, $[15_4/75_4]_T$, $[-15_4/75_4]_T$ laminates. It was observed from the experimental results that the start austenite temperature had changed since the time the SMA wire was calibrated. New predictions reflecting as closely as possible the experimental conditions, i. e., initial stress in the SMA wire, initial curvatures of the laminates, new austenite start temperature, were computed and compared with the experimental results. From the correlations it was observed that the overall laminate response is generally predicted quite well. The strain levels before and after the snap through are generally quite close, and the temperature at which the laminate snaps is predicted within a few degrees. Given that the snap through of the laminate is a dynamic and unstable event, which can be influenced by small unwanted perturbations, the correlation between the experiments and the predictions is thought to be quite good. It would, in fact, have been quite exceptional to obtain correlations as good as the ones obtained with the narrow aluminium plate, since the mechanisms involved in the laminate snap through are much more complex. One major difference between the experiments and the predictions are in the rate of increase of the laminate strains with respect to the temperature in the SMA wire. During the experiments it was observed that the strains were increasing at a rate slower than predicted. On the other hand, in the experiment with the narrow aluminium plate the measured and predicted strains increased at a similar rate. However, the experiments on the unsymmetric laminates were quite different than the experiment on the narrow aluminium plate. First, the configuration used for the attachment of the SMA wire was not exactly the same. For the unsymmetric laminates the SMA wire was stretched around several supports whereas for the aluminium plate the wire was simply stretched between two end supports. Second, unsymmetric laminates are a more complex structure than the narrow aluminium plate. It is possible that the theory developed in Chapter 4 is not able to fully represents the mechanics involved in the response of unsymmetric laminates to applied forces. Experiments which were previously conducted on a $[0_2/90_2]_T$ laminate and were briefly presented at the end of Chapter 4 showed that the strains in the laminates induced by known applied forces were very well predicted by the developed theory. However, it is possible that the function which was selected in Chapter 2 for the out-of-plane displacement, $w_o(x, y)$, may not be able to fully represent the shape of the

laminate as forces are applied, even though this function was found to correlate well with the measured room-temperature shapes of the laminates, as observed in Chapter 3. Since the displacements of the laminate are directly used to evaluate the recovery strain of the SMA wire, a small discrepancy between the actual shape and the predicted shape would affect the relations between the laminate strains, the recovery strain, and the temperature in the SMA wire. The recovery strain is used in the SMA constitutive model to evaluate the force generated by the wire at a given temperature. The deformations of the laminate are then computed for the corresponding force level. This solution procedure was described in detail in Chapter 5. Thus the relations between the strains in the laminate, the recovery strains, and the temperature in the wire involve complex phenomenon, which may be quite difficult to capture precisely. But as observed, the developed theory is able to predict the overall laminate response to SMA induced forces quite well.

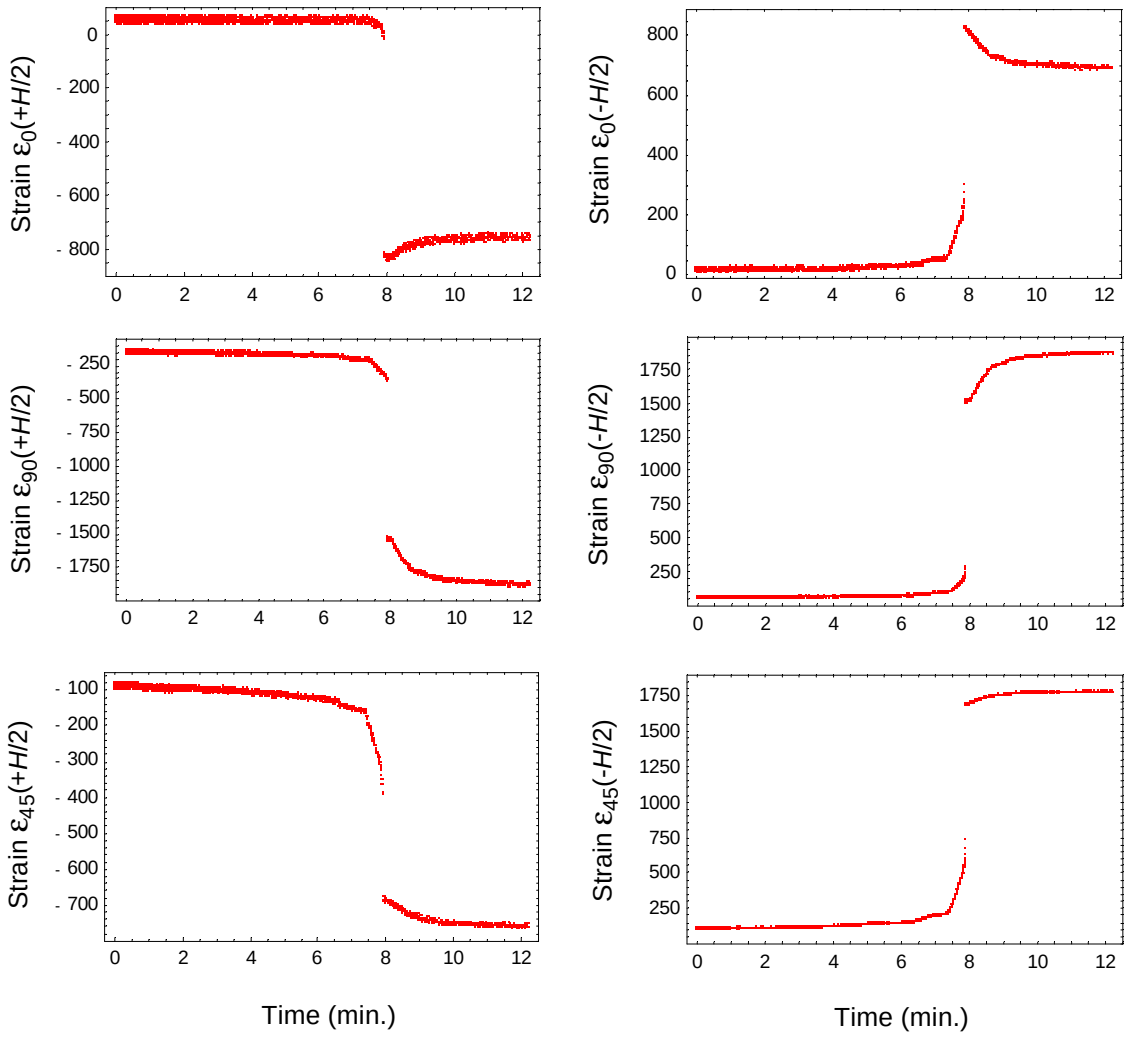

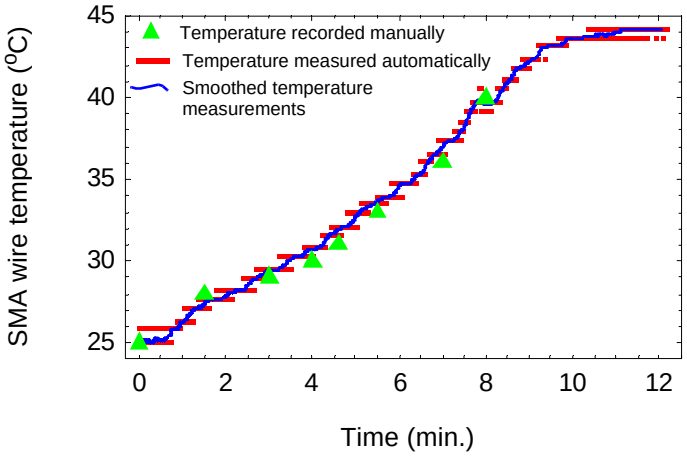

Fig. 7-6. Strain and temperature measurements: $[-30_4/30_4]_T$ laminate, first experiment

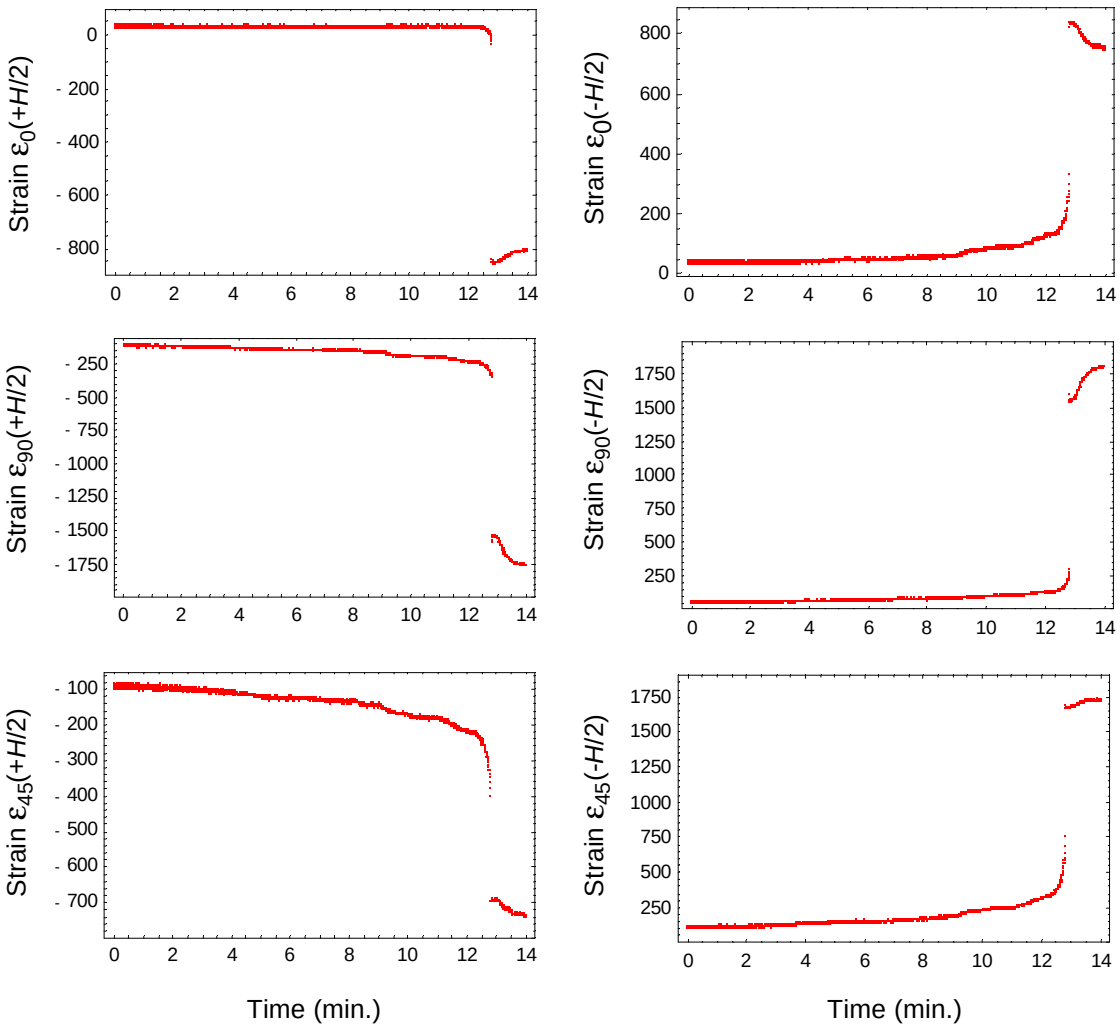

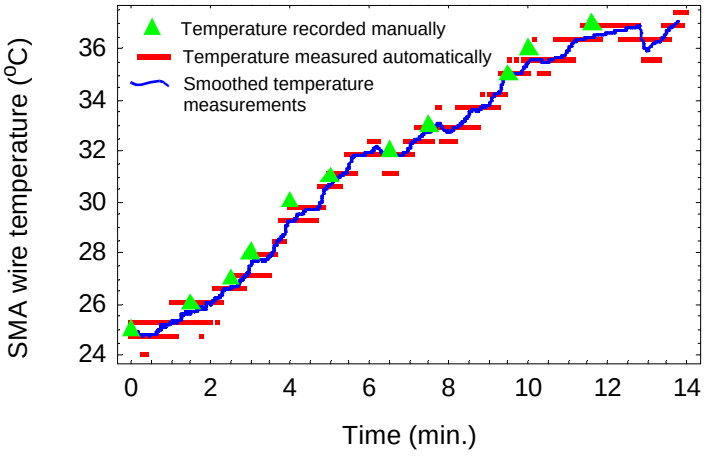

Fig. 7-7. Strain and temperature measurements: $[-30_4/30_4]_T$ laminate, second experiment

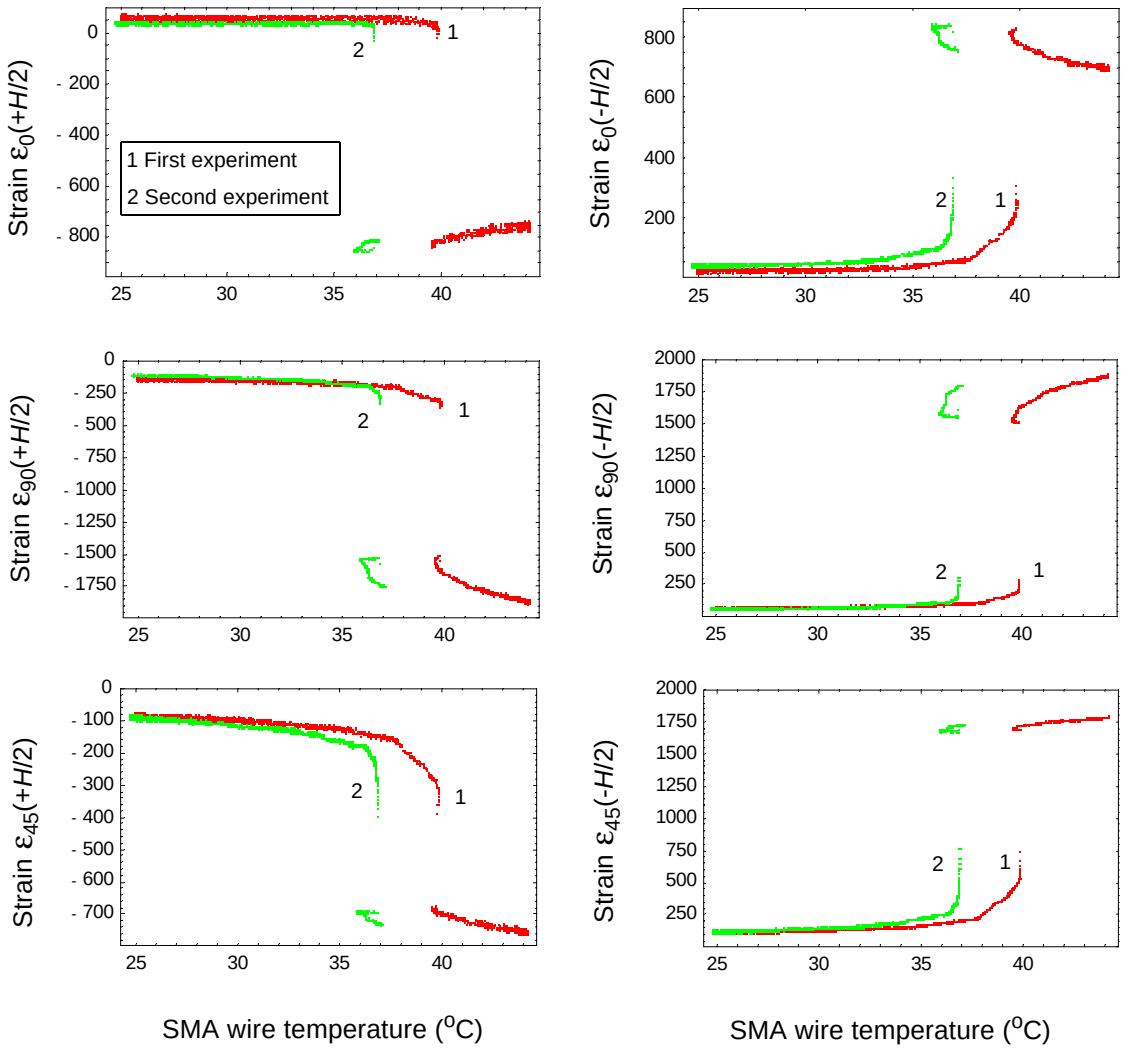

Fig. 7-8. Wire temperature-laminate strain relations from the first and second experiments: $[-30_4/30_4]_T$ laminate

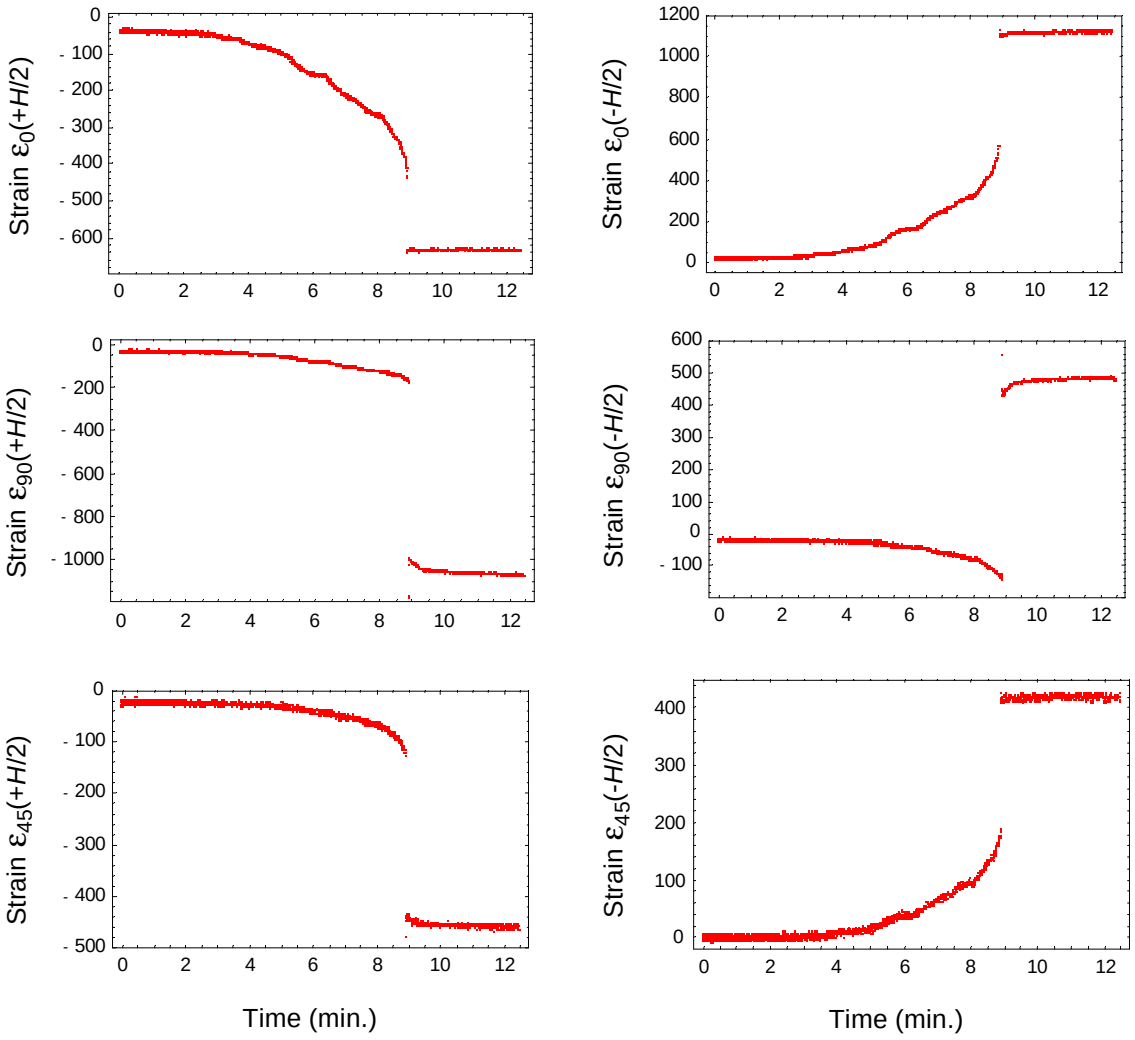

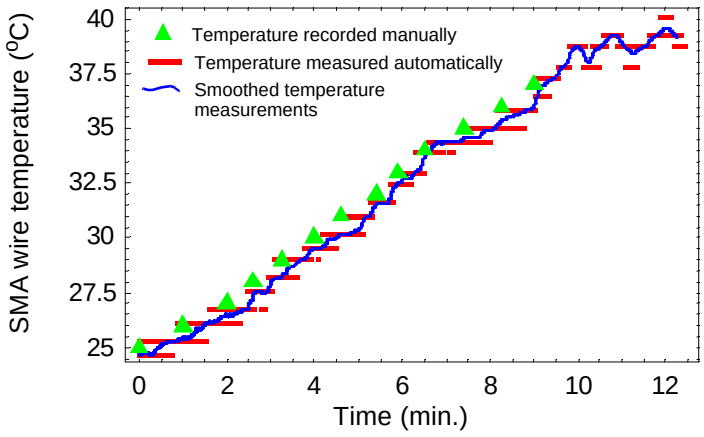

Fig. 7-9. Strain and temperature measurements: $[60_4/30_4]_T$ laminate, first experiment

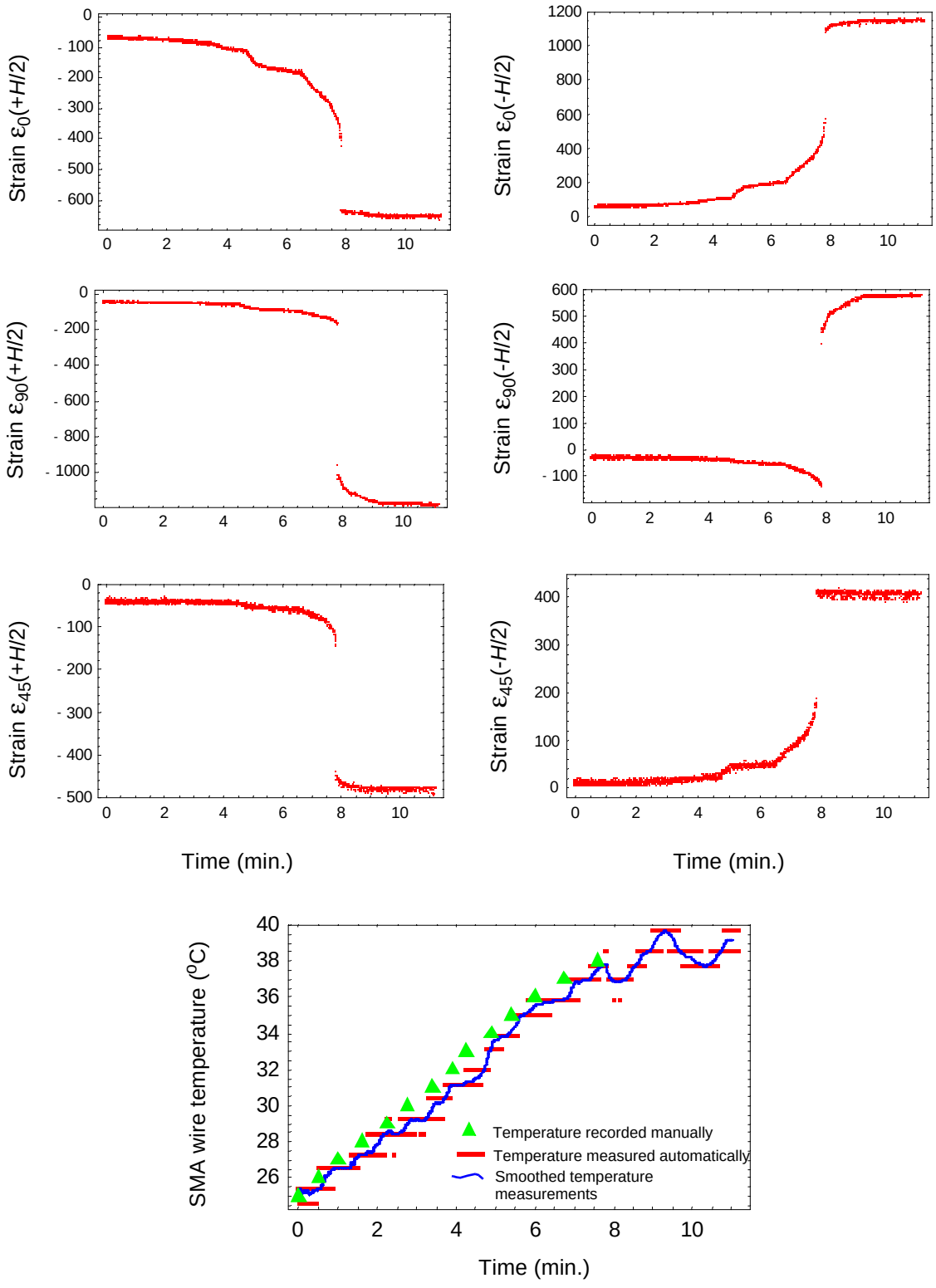

Fig. 7-10. Strain and temperature measurements: $[60_4/30_4]_T$ laminate, second experiment

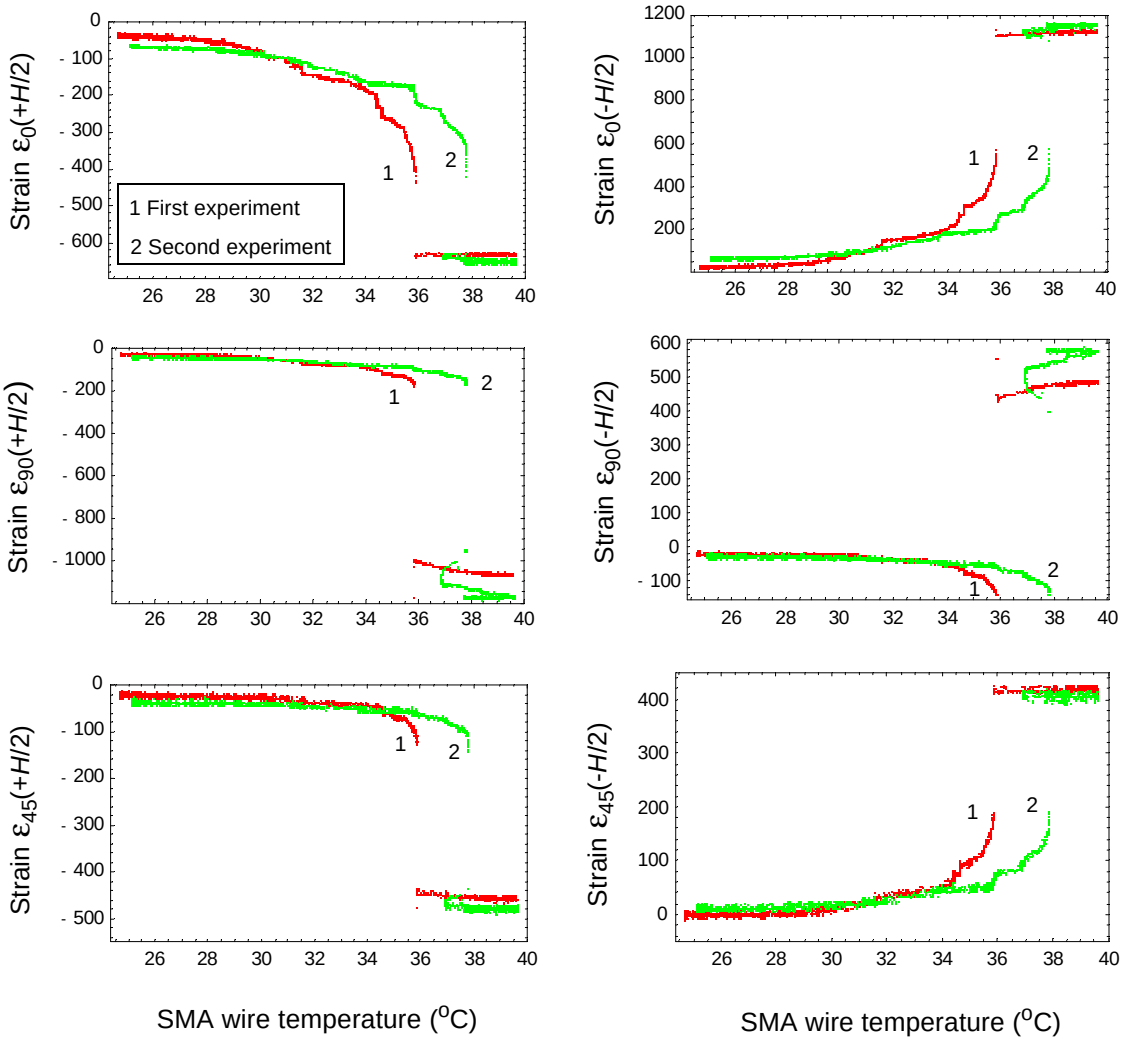

Fig. 7-11. Wire temperature-laminate strain relations from the first and second experiments: $[60_4/30_4]_T$ laminate

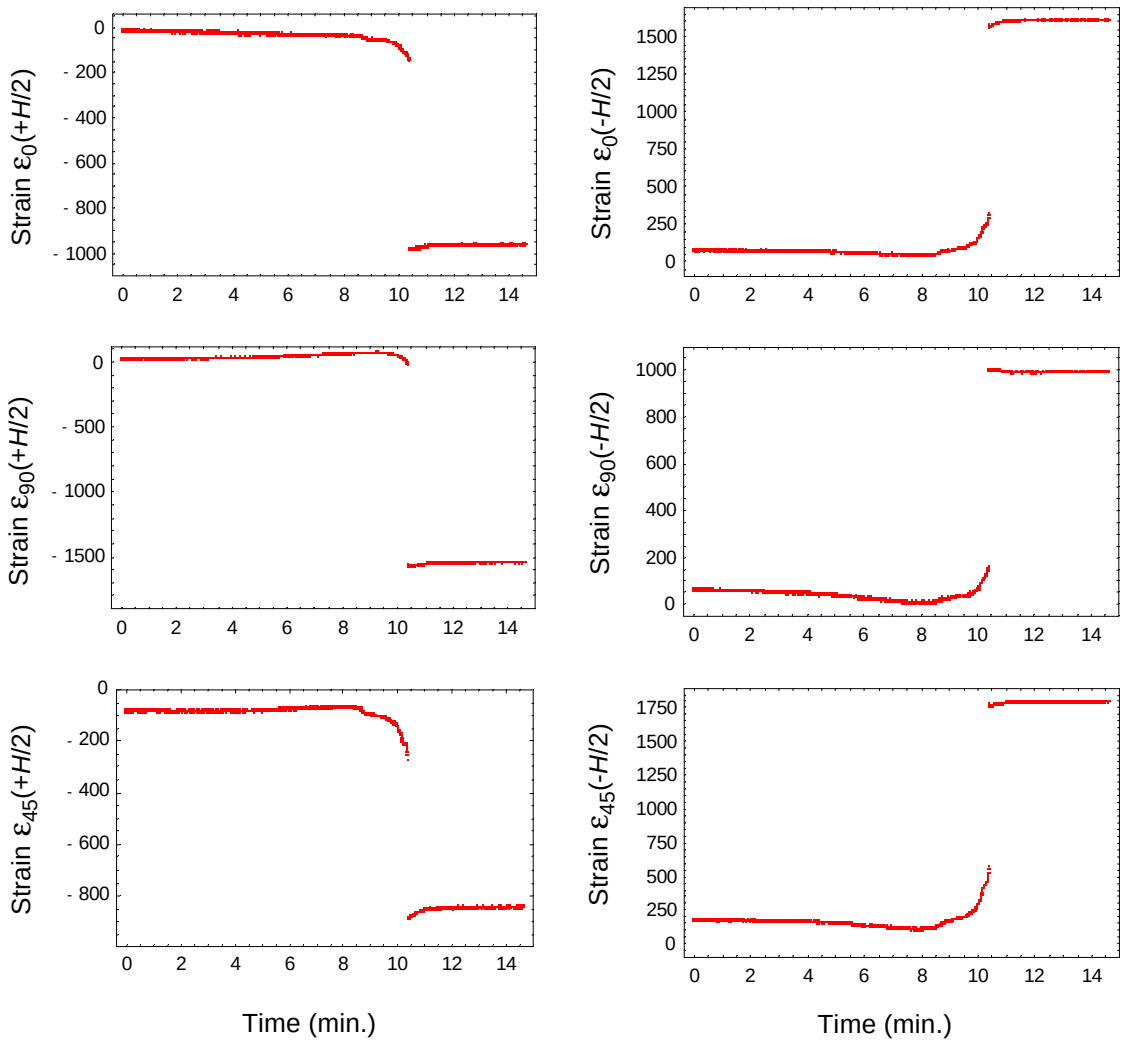

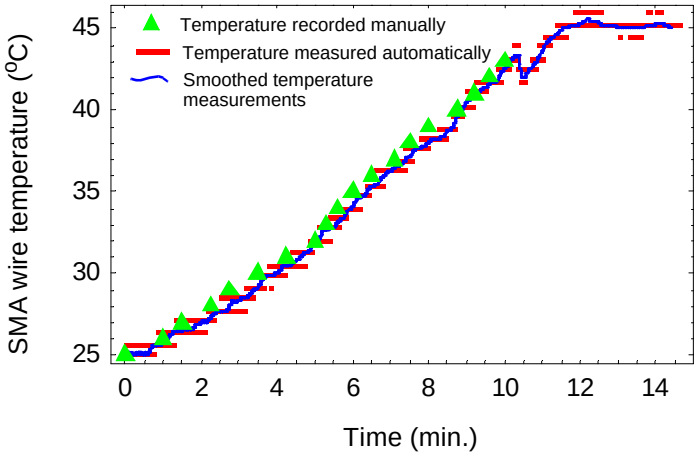

Fig. 7-12. Strain and temperature measurements: $[-60_4/30_4]_T$ laminate, first experiment

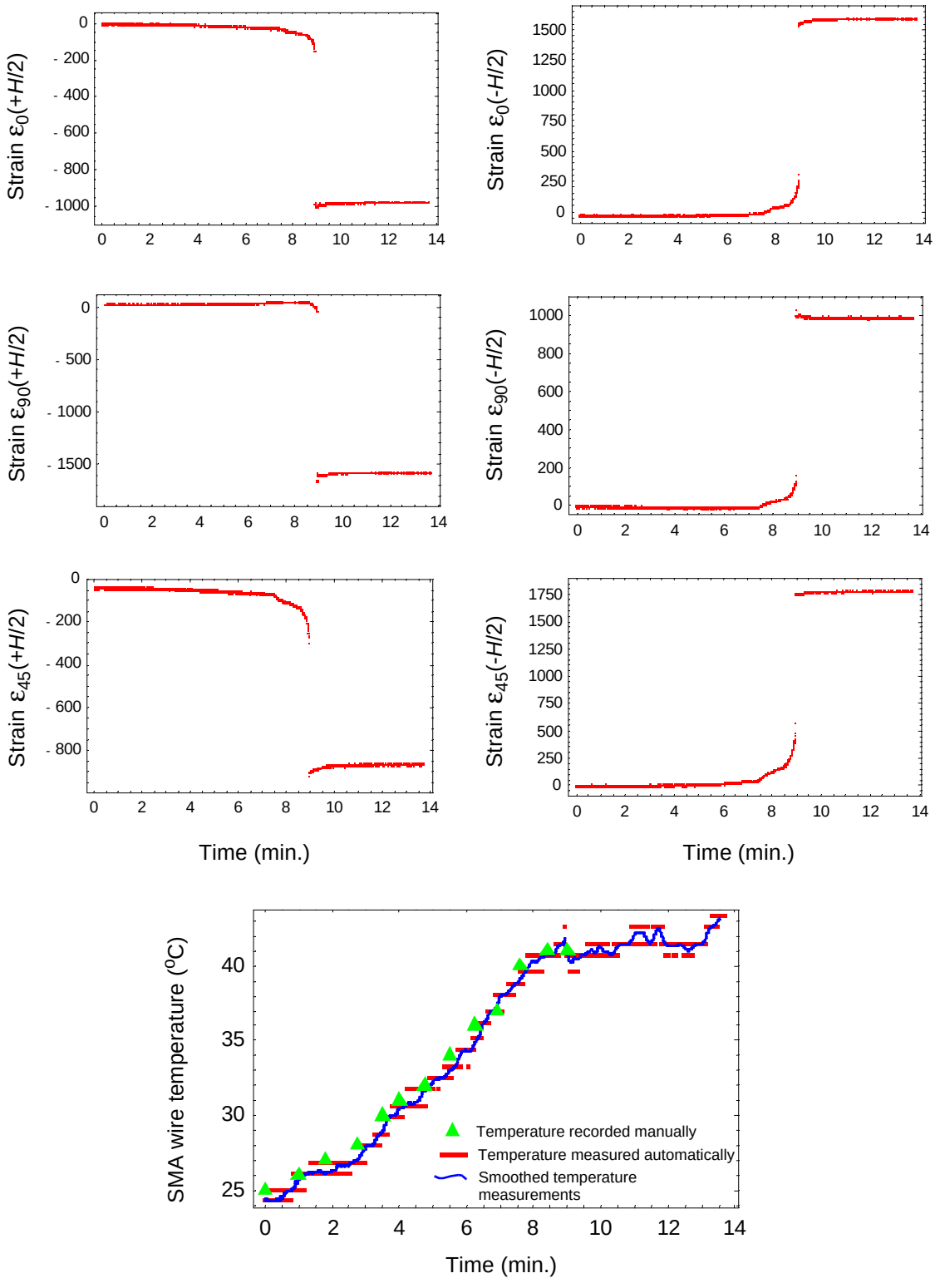

Fig. 7-13. Strain and temperature measurements: $[-60_4/30_4]_T$ laminate, second experiment

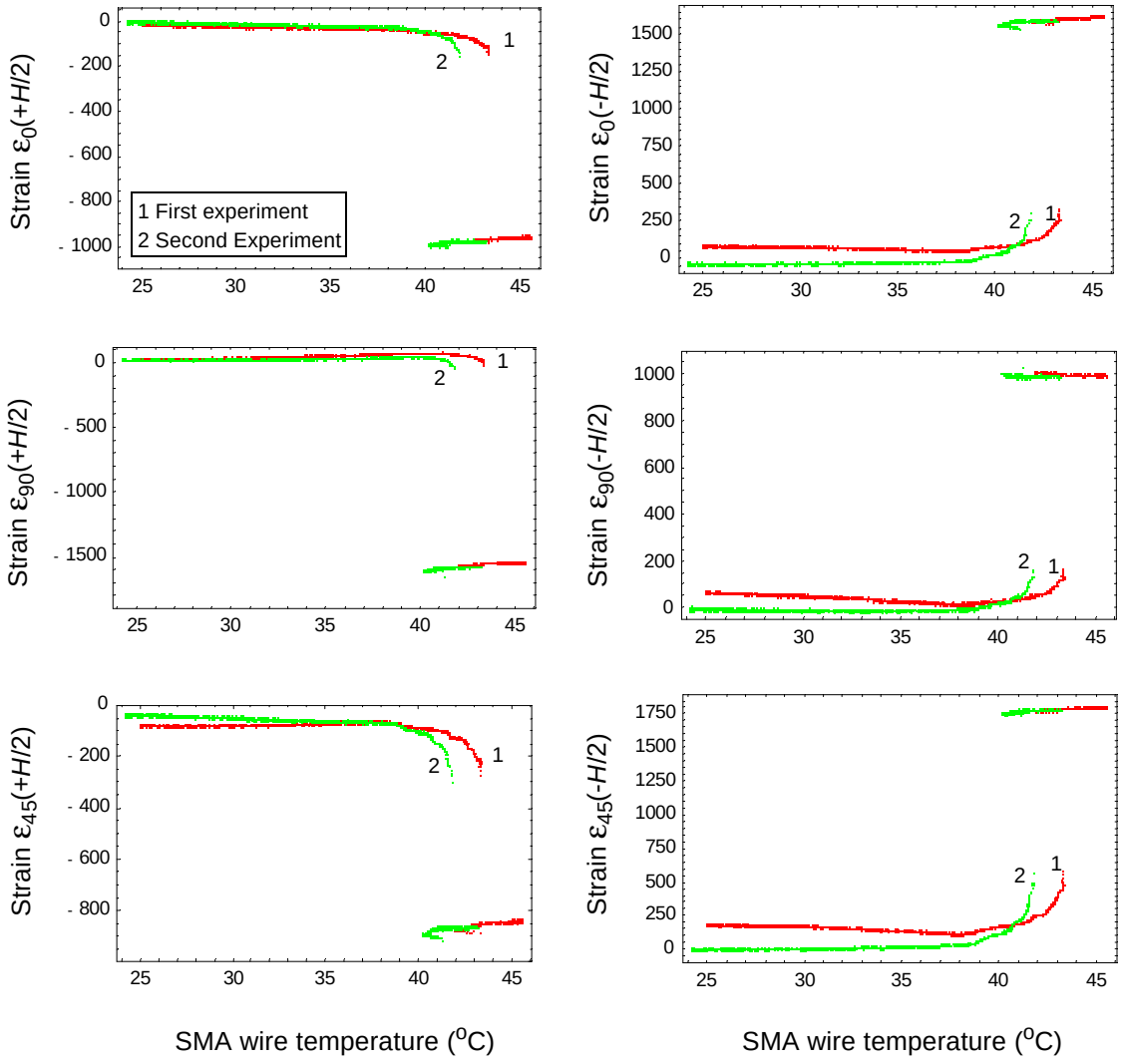

Fig. 7-14. Wire temperature-laminate strain relations from the first and second experiments: $[-60_4/30_4]_T$ laminate

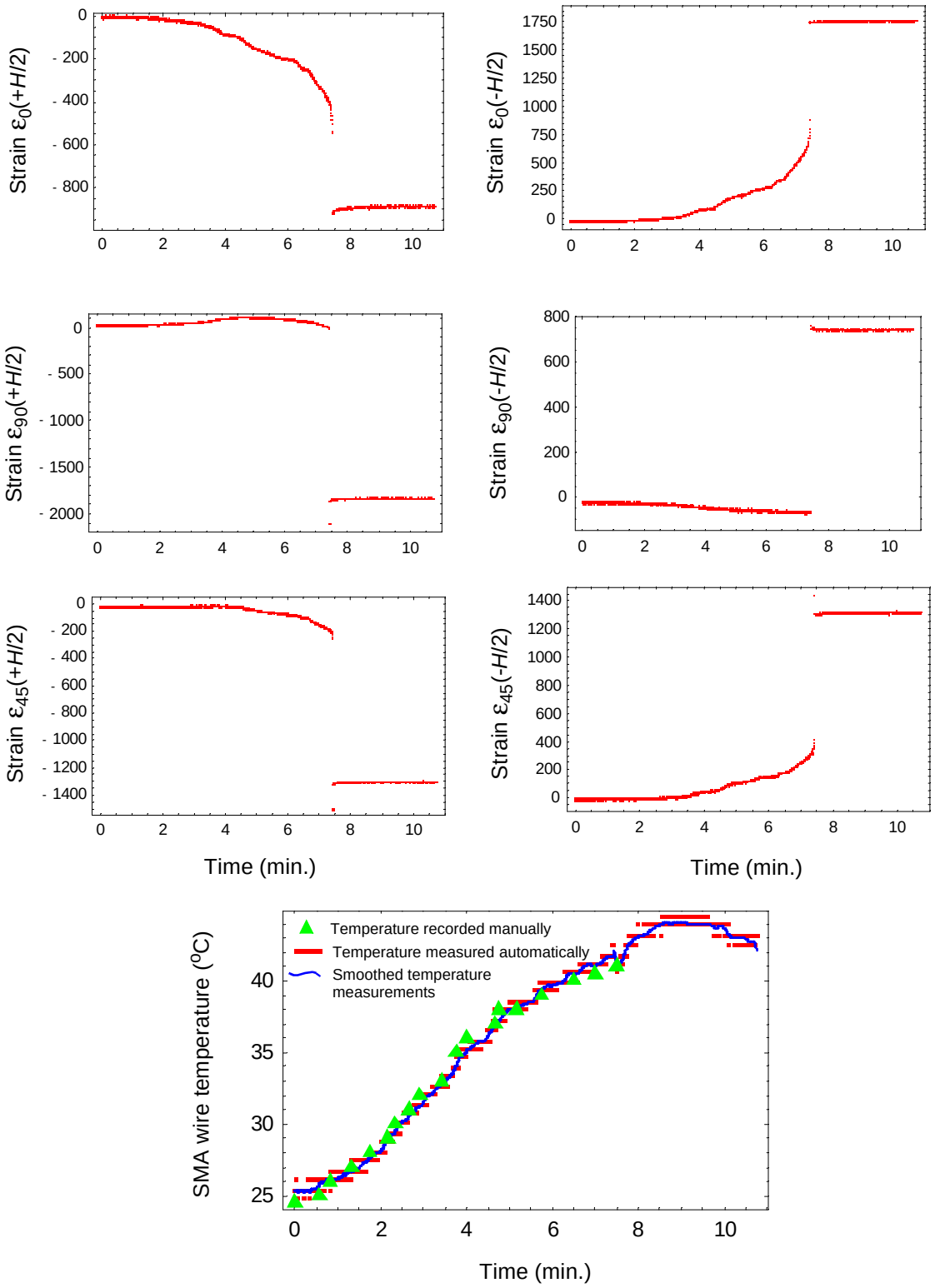

Fig. 7-15. Strain and temperature measurements: $[90_4/0_4]_T$ laminate, first experiment

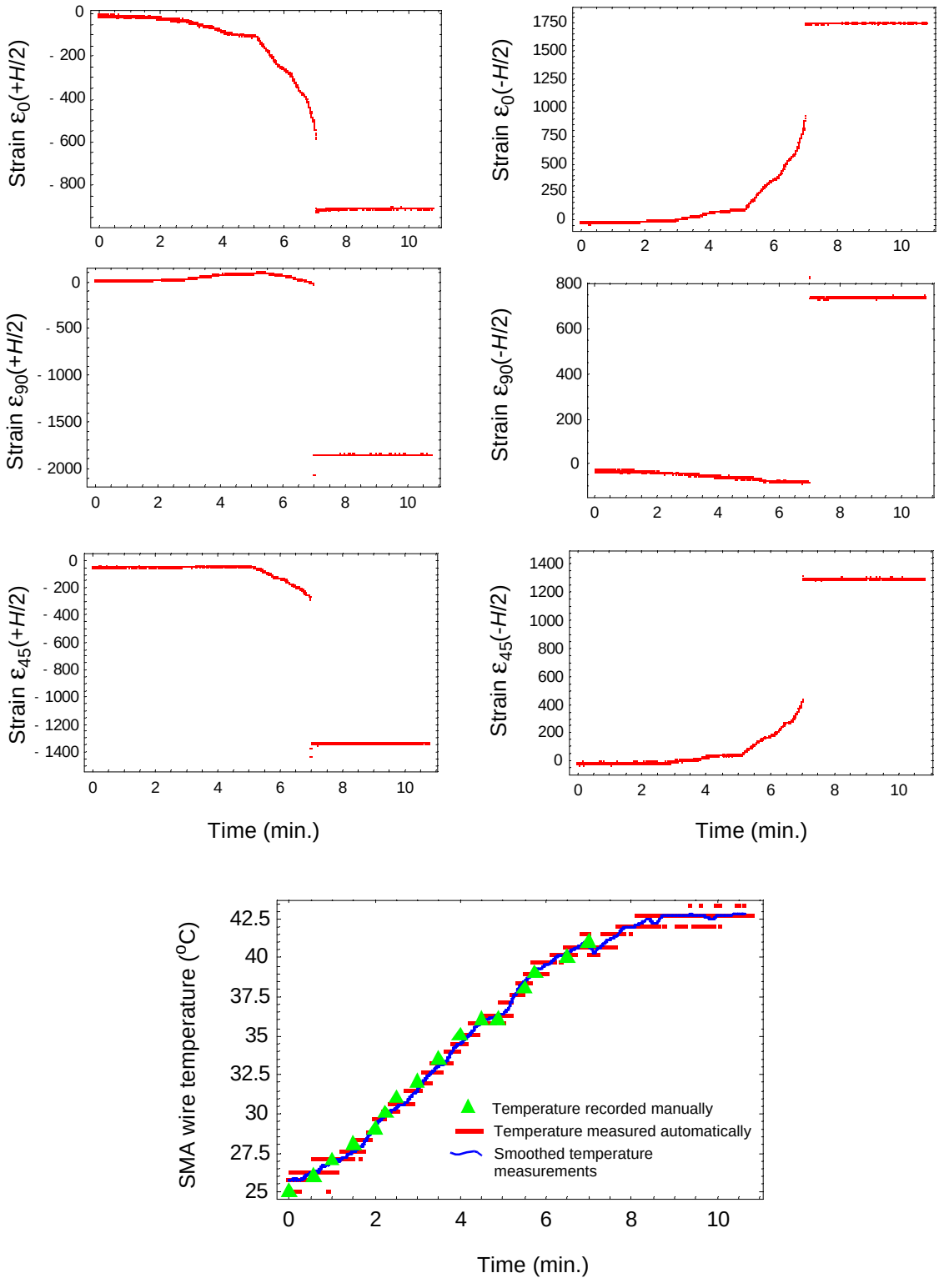

Fig. 7-16. Strain and temperature measurements: $[90_4/0_4]_T$ laminate, second experiment

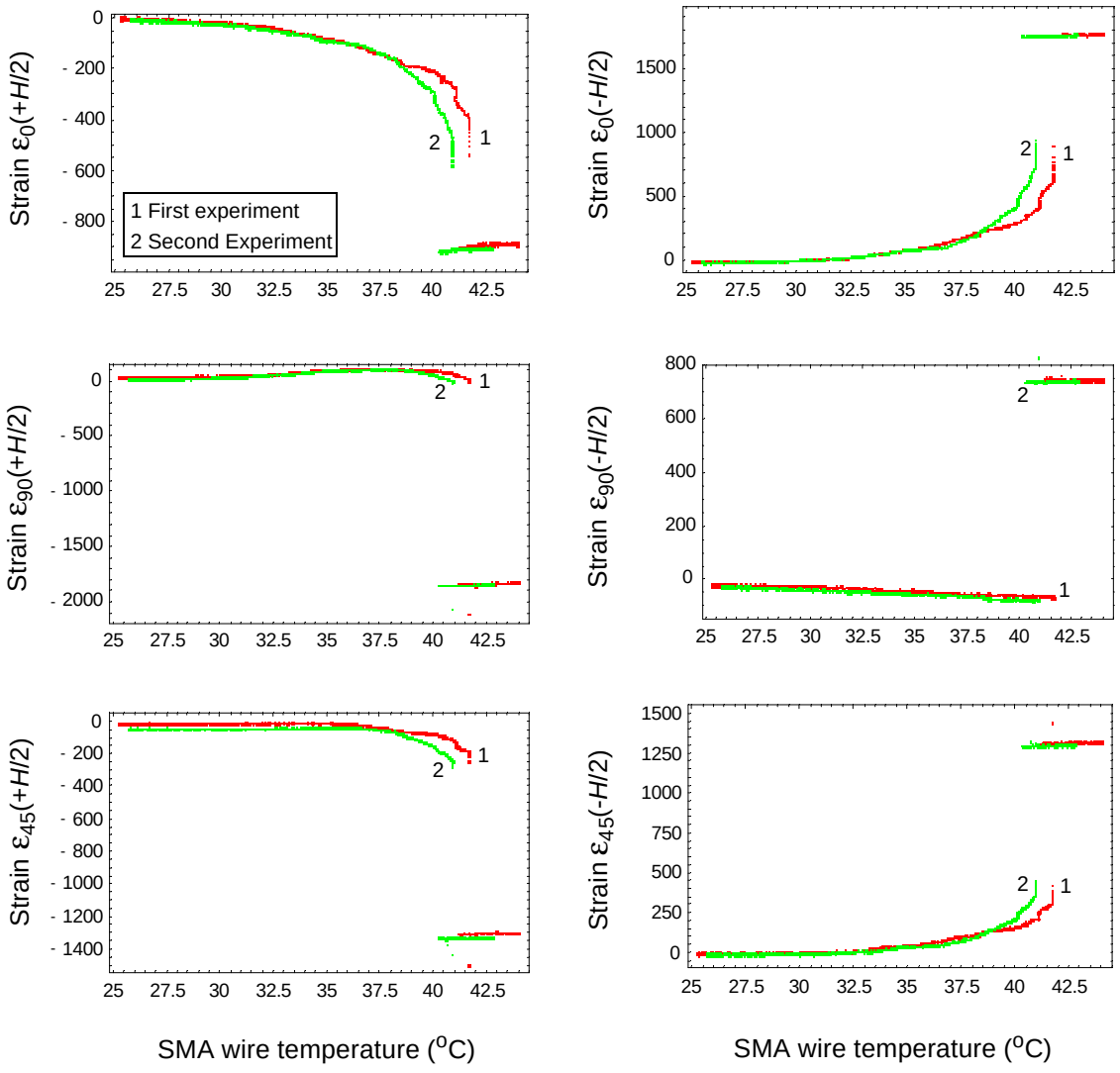

Fig. 7-17. Wire temperature-laminate strain relations from the first and second experiments: $[90_4/0_4]_T$ laminate

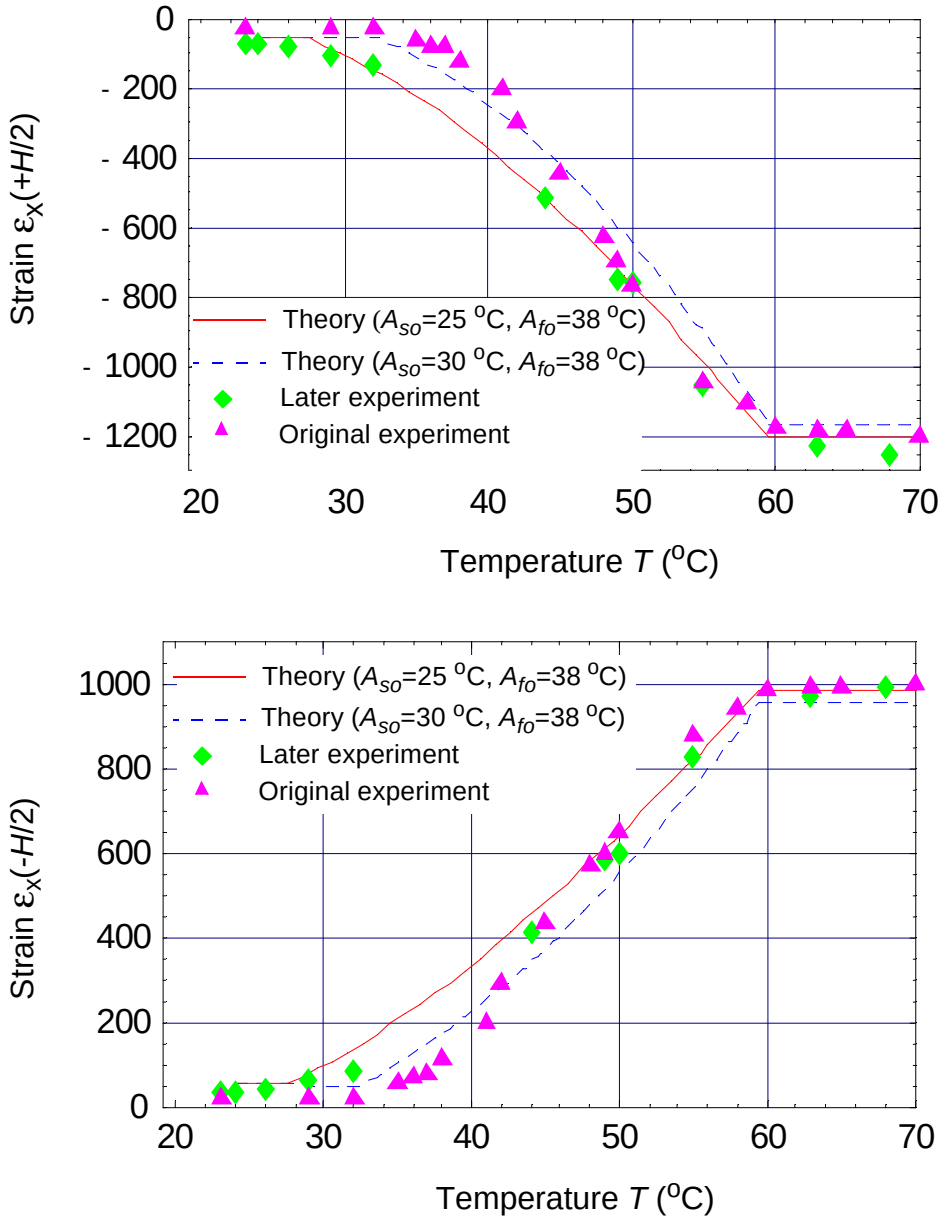

Fig. 7-18. Comparison of the temperature-strain relations of the narrow aluminium plate measured at two different times with the predictions of the model using two different sets of phase transformation temperatures

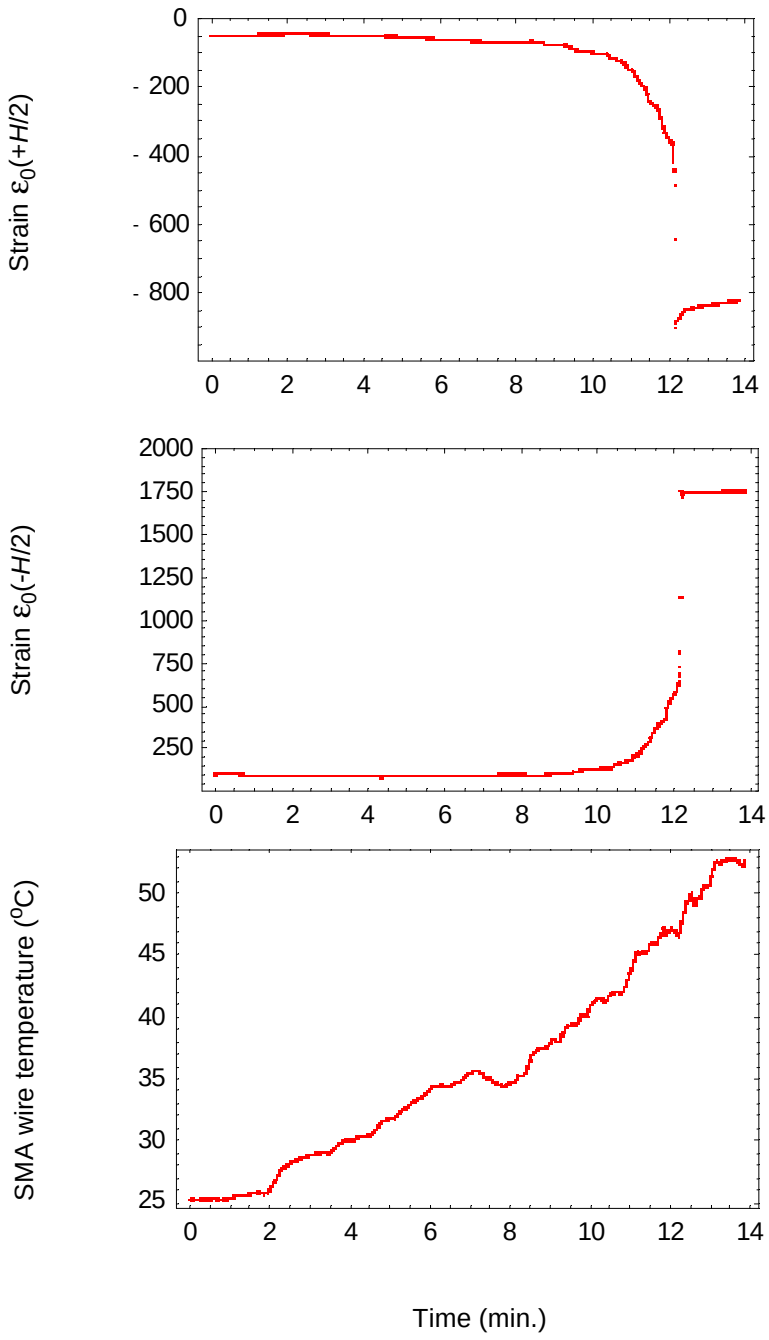

Fig. 7-19. Strain and temperature measurements: $[90_4/0_4]_T$ laminate, original experiment

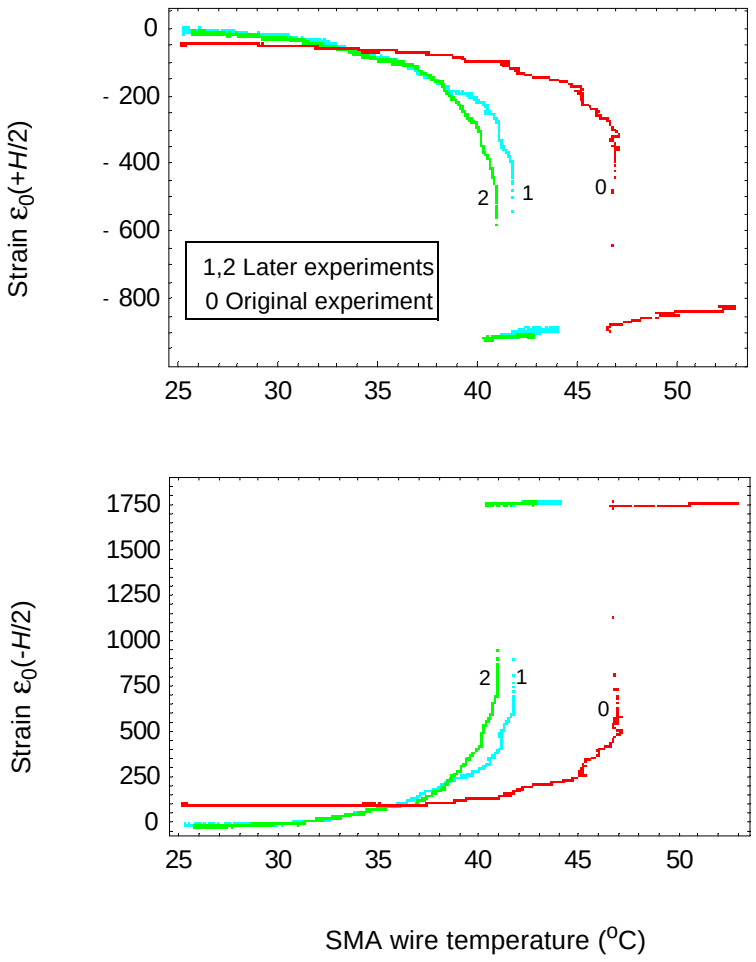

Fig. 7-20. Wire temperature-laminate strain relations: $[90_4/0_4]_T$ laminate, original and later experiments

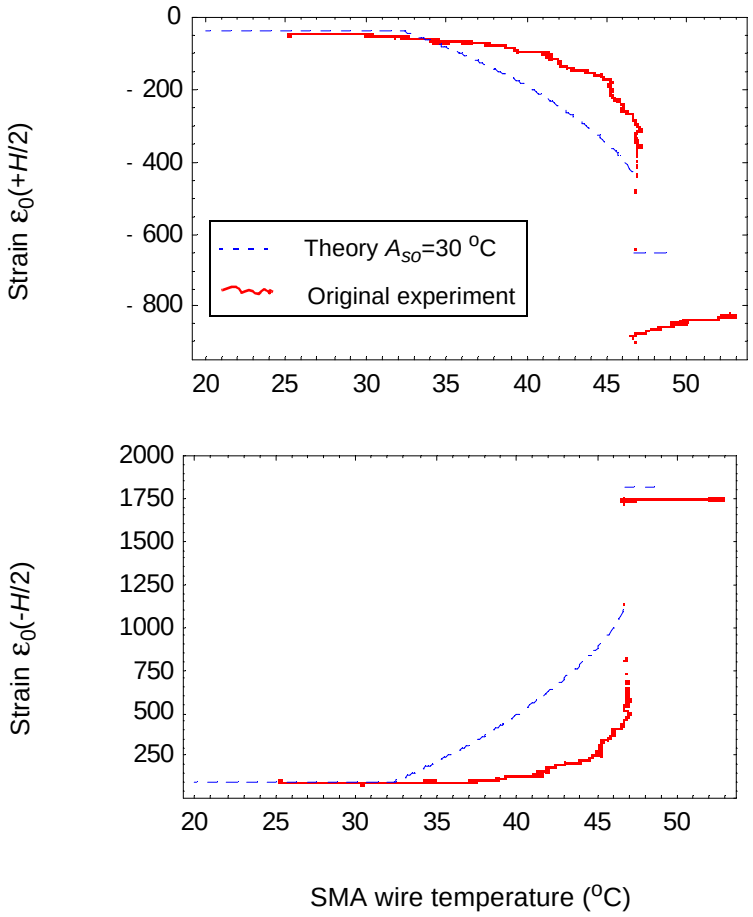

Fig. 7-21. Measured and predicted wire temperature-laminate strain relations: $[90_4/0_4]_T$ laminate, original experiment

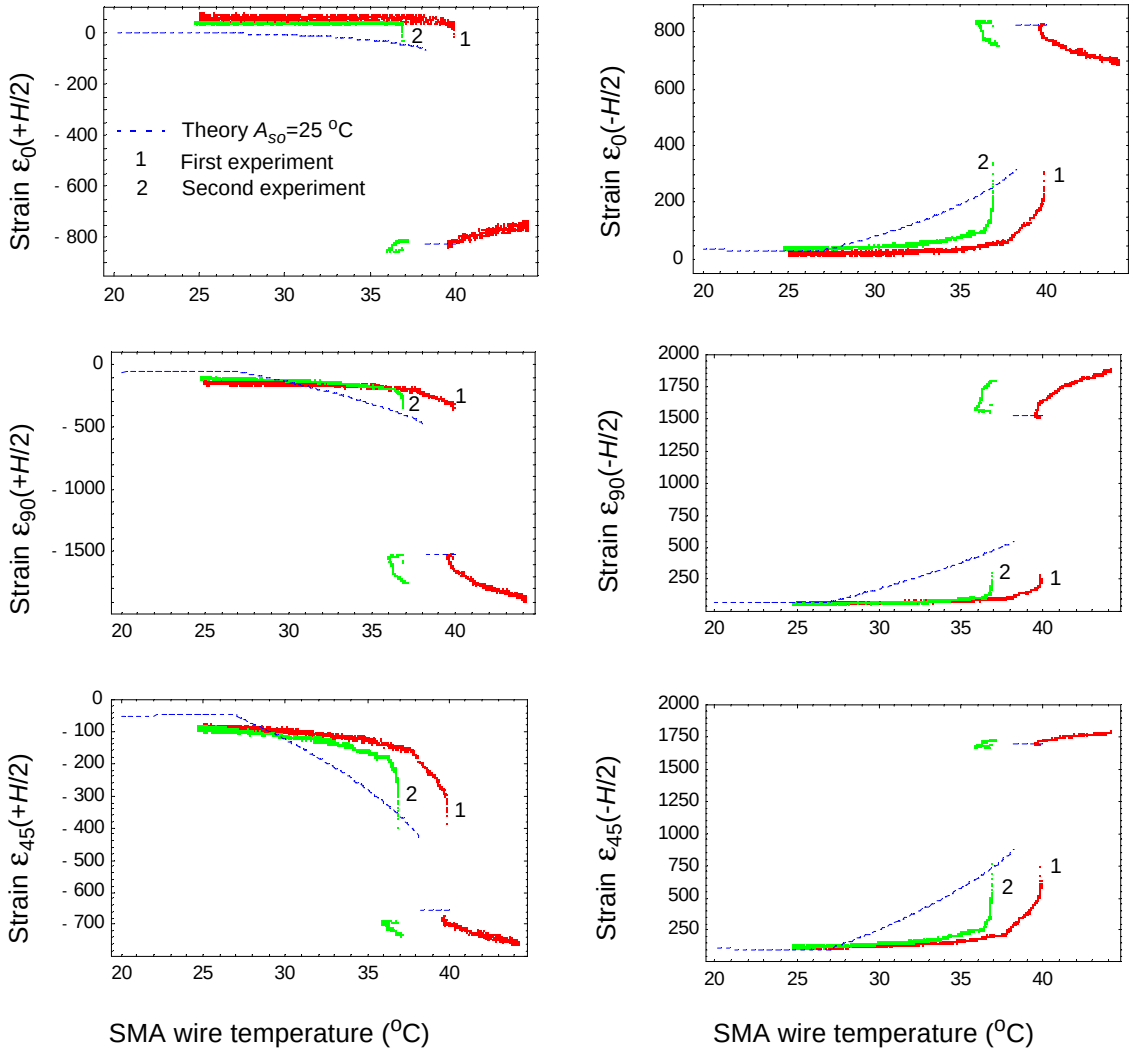

Fig. 7-22. Measured and predicted wire temperature-laminate strain relations: $[-30_4/30_4]_T$ laminate

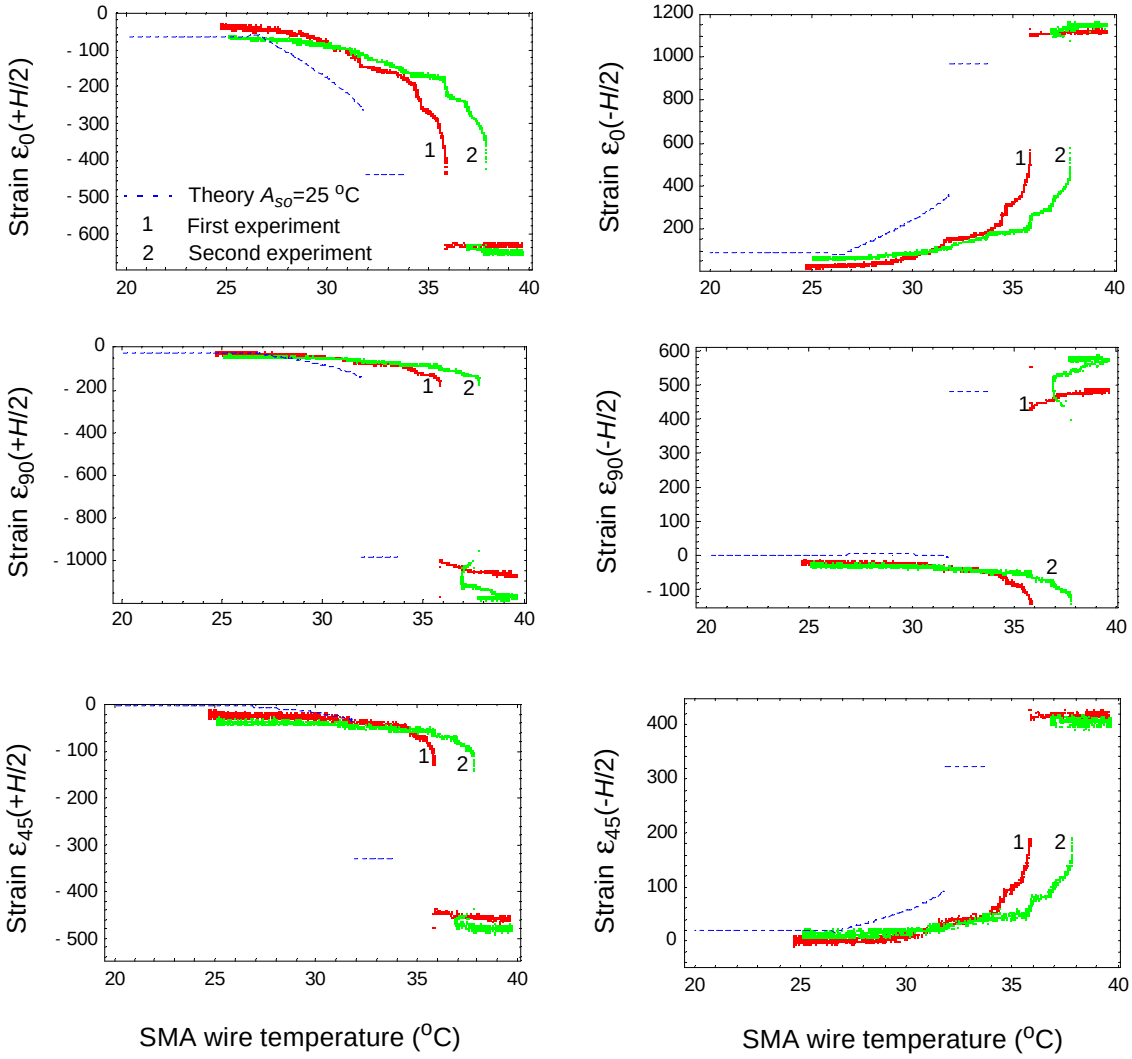

Fig. 7-23. Measured and predicted wire temperature-laminate strain relations: $[60_4/30_4]_T$ laminate

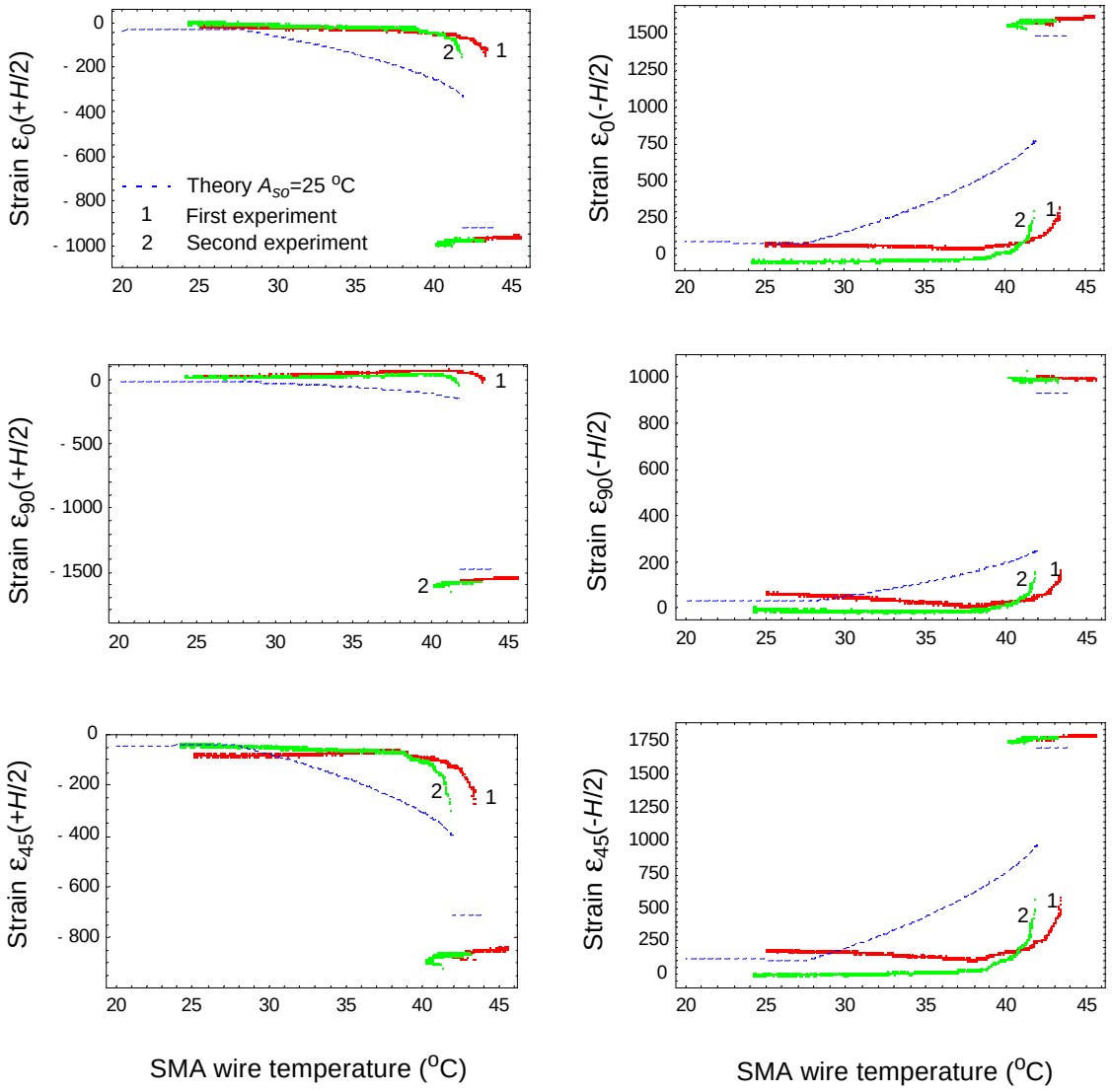

Fig. 7-24. Measured and predicted wire temperature-laminate strain relations : $[-60_4/30_4]_T$ laminate

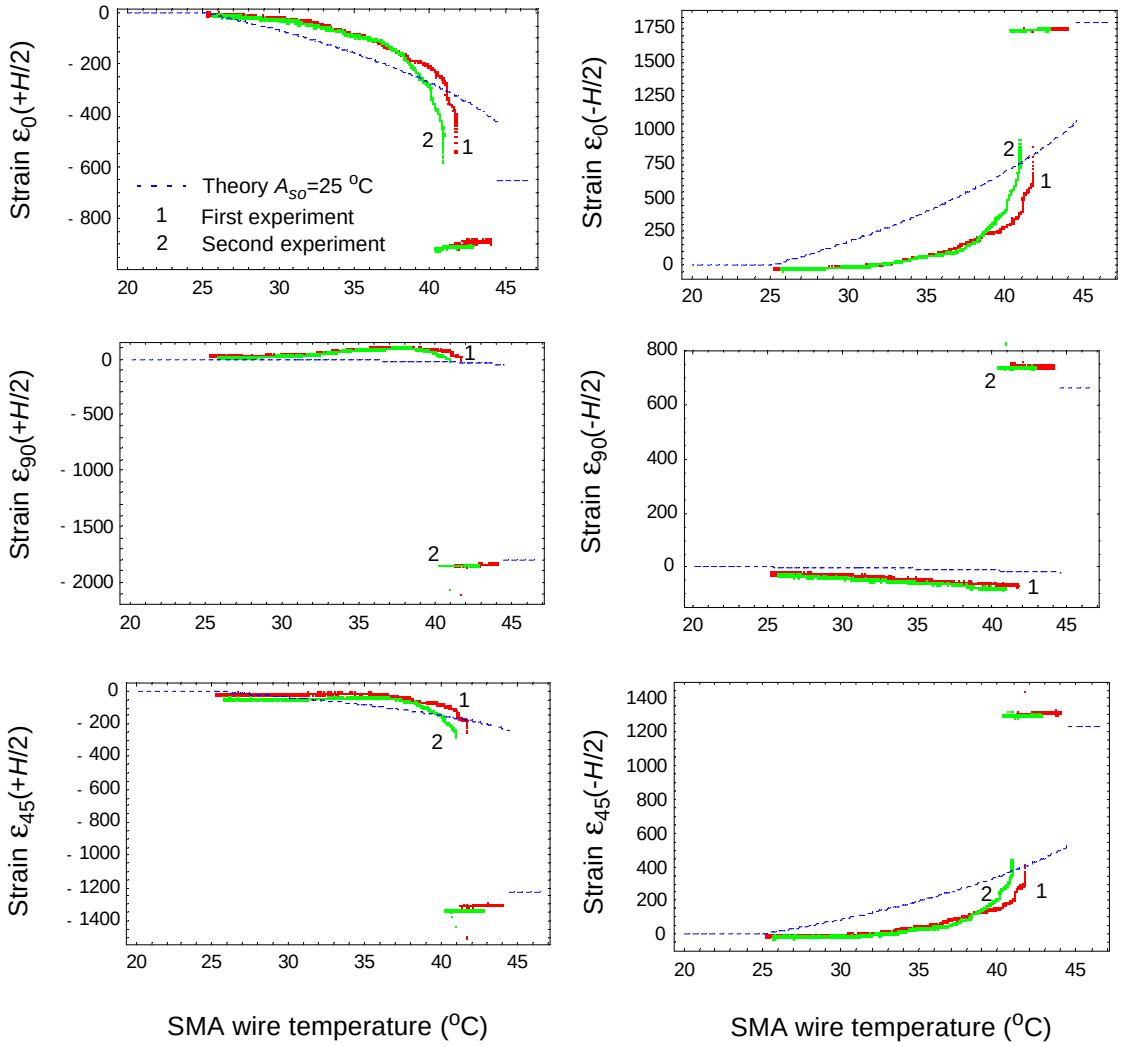

Fig. 7-25. Measured and predicted wire temperature-laminate strain relations: $[90_4/0_4]_T$ laminate

Chapter 8 Closure

8.1 Summary of the work accomplished

1. A theory to predict thermally-induced deformation behavior in unsymmetric laminates was developed.

A nonlinear theory, based on polynomial approximations to the midplane strains and out-of-plane displacements and a Rayleigh-Ritz approach to represent the total potential energy, has been develop to predict the deformation behavior of general unsymmetric laminates subjected to a temperature change, especially the cooling from the elevated cure temperature flat condition to room temperature. To further study unsymmetric laminates and to verify the Rayleigh-Ritz approach, finite-element analyses were conducted using the commercial code ABAQUS. Also the predictions obtained with the developed theory were compared with predictions obtained with previously developed theories, especially, Peeter, Powell, and Warnet's theory [17] and Jun and Hong's theory [16]. The comparisons of the predictions from the developed theory with predictions from ABAQUS and previously developed theories demonstrated that:

- The curvatures of the laminates at room temperature predicted by the developed theory correlate well with the finite-element predictions.

- The theory developed by Peeter, Powell, and Warnet to predict the thermally-induced deformations of angle-ply unsymmetric laminates is based on an incorrect assumption, i. e., that the principal curvature direction for all angle-ply laminates is 45^{o}.

- The laminate deformations predicted by the developed theory are more accurate around the bifurcation temperature than the predictions from Jun and Hong. Being able to predict the deformations near the bifurcation point correctly is important for studying the snap-through phenomenon associated with unsymmetric laminates.

2. The shapes of a wide range of unsymmetric laminates were measured experimentally.

A total of eight different unsymmetric laminates were manufactured. Their room-temperature shapes were measured twice, one time right after curing and a second time six months later. The experimental results from the first measurement correlated well with the predictions from the theory and the finite-element program ABAQUS. The measurement conducted the second time revealed that the curvatures of all laminates had decreased. Reasons for the curvature change is not obvious. It may be possible that relaxation of the epoxy-matrix occurred during the elapsed time, leading to a decrease in the laminate curvatures. From these experiments it can be concluded that:

- The developed theory predicts quite accurately the shapes of unsymmetric laminates at room temperature.

- The room-temperature shapes of unsymmetric laminates may change with time, depending on fluctuations of the environmental conditions (temperature, humidity) or depending of the aging of the material (matrix relaxation).

3. The developed theory was extended to predict the laminate response to simple applied forces.

The effects of forces applied on unsymmetric laminates were modeled and implemented in the developed theory so that the laminate deformations could be predicted at any temperature change ΔT and applied force level F. In particular the deformation behavior as the laminates reached the snap through was studied. As the applied force was increased, the laminate shape changed to become similar to the unstable shape at the snap through. As a result, the principal curvature direction gradually decreased to become close to the one of the unstable shape. It was also noted that the force level required to generate the snap through was proportional to the magnitude of the initial laminate curvatures, which were themselves proportional to the angle between the fibers in the plies. From these predictions, it seems that:

- The developed theory is able to capture the snap-through phenomenon correctly.

- Changing the configuration of the cross-ply unsymmetric laminate requires the largest applied force.

4. A SMA constitutive model was implemented in the developed theory.

Since the ultimate objective of this work was to model the deformation behavior of unsymmetric laminates to SMA-induced forces, an existing SMA constitutive model was implemented in the developed theory. Preliminary experiments were conducted on a narrow aluminium plate on which a SMA wire was attached. The measurements of the strains induced in the plate as a function of the temperature in the SMA wire showed that the phase transformation temperatures, A_{so} and A_{fo}, supplied by the manufacturer were not representative of the phase transformation temperatures of the actual material. In addition, the temperatures could change with time and material usage. After these temperatures were modified, good correlations were obtained between the measurements and the predictions of the developed theory applied to the

aluminium plate. The theory was then used to predict the response of unsymmetric laminates to SMA-induced forces. From the preliminary experiment conducted on the narrow aluminium plate and the simulations computed using the theory, it can be concluded that:

- The thermal properties of SMA specified by the manufacturer are not necessary representative of the thermal properties of the actual material.

- The theory predicts quite accurately the SMA-induce deformations of the aluminium narrow plate.

- SMAs should be able to actuate sufficient force and recover enough strain to change successfully the laminate configuration.

5. The configuration of unsymmetric laminates was successfully changed in experiments by using a SMA wire as actuator.

A pre-strained SMA wire was attached on the laminate surface. By applying voltage, the SMA wire was resistively heated until the wire had actuated enough force to induce the laminate snap through. During these experiments the strains in the laminates and the temperature in the SMA wire were measured. The experimental results showed that the austenite start temperature had decreased since it was evaluated during the original experiment on the narrow aluminium plate. After adjusting the theory to account for the start austenite temperature decrease, the laminate curvature decreases, and the initial pre-stress in the SMA wire to reflect as much as possible the experimental conditions, the predictions obtained for the laminate response as the SMA wire is heated were quite close to the experimental measurements. The temperature in the SMA wire at which the laminate snapped through is predicted within a few degrees. The predicted strains in the laminate before and after the snap through correlate quite well. The main differences between the predictions and the experimental measurements are in the rate of increase of the laminate strains versus the temperature in the SMA wire. As the SMA wire is heated, the measured strains increase at a rate slower than predicted. The reasons for the difference are not obvious since the relations between the strains in the laminate and the temperature in the wire involve complex mechanics. It is possible that the assumed function for the laminate out-of-plane displacement is not adequate to represent the out-of-plane deflection of the laminate as forces are applied. But as observed, the developed theory is able to predict the overall laminate response to SMA induced forces quite well, especially after and before the snap through. This is a significant contribution to the literature.

8.2 Suggestions for further research

From the work that was accomplished and presented in the previous chapters, the following suggestions for future research are proposed:

1. The decrease in the unsymmetric laminate curvatures after cure should be studied more

fully.

It was observed during the measurement of the room-temperature shapes of the laminates that the laminate curvatures had decreased in magnitude since the time the laminates were cured. The reason for the decrease is not obvious. The laminates were kept in a dry environment so that moisture absorption would not be a factor. A possible explanation is that the epoxy matrix had relaxed with time. This is only an assumption which should be further investigated.

2. The laminate response to applied forces could be checked experimentally.

The experiments using an SMA wire to generate forces on unsymmetric laminates showed that the developed theory could predict quite accurately the overall response of the laminate. However, as the SMA wire is heated, it was observed that the strains in the experiments increased at a rate slower than predicted. The reasons for the differences are not obvious. To understand why the developed theory does not capture the increase of the strains better, it would certainly be valuable to check experimentally the laminate response to known applied forces. Measuring the strains in the laminate and the displacements of the supports as a function of known applied force, not necessarily generated by SMA wires, would provide a check on the accuracy of the developed theory.

3. The SMA wire should be trained.

It was observed during the experiments with the SMA wire that the properties of the wire changed since the time the wire was originally used. The change in the response of SMAs as cyclic loading is applied is a phenomenon that has been observed previously by some investigators [35-36]. In order to stabilize the SMA response, a so-called thermomechanical training can be performed. The training consists in performing a cycling thermal and/or mechanical loading on the SMA until the response of the SMA has stabilized. In addition, by using a proper thermomechanical cycling, a two-way shape memory alloy can be obtained [37]. A two-way shape memory alloy, as opposed to a one-way shape memory alloy, which was used in this research, has the advantage of exhibiting a reversible shape-memory effect. A two-way shape memory alloy is able to recall both undeformed and deformed shapes when, respectively, heated above the austenite finish temperature and cooled below the finish martensite temperature. Thus, using a two-way shape memory alloys could be more convenient than using a one way-shape memory alloys to control the shape of structures.

References

[1] Dano, M.-L. 1993. “SMA-Induced Deformations in Unsymmetric Cross-Ply Laminates,” M. S. Thesis in Engineering Mechanics, Virginia Polytechnic Institute and State University, Blacksburg, VA.

[2] Dano, M. -L. and M. W. Hyer. 1996. “The Response of Unsymmetric Laminates to Simple Applied Forces,” *Mechanics of Composite Materials and Structures*, 3:65-80.

[3] Pagano, N. J. and H. T. Hahn. 1977. “Evaluation of Composite Curing Stresses,” J.G. Davis, Jr. (Ed), Composite Materials: Testing and Design, 4th Conference, American Society for Testing and Materials, Philadelphia, 317-329.

[4] Crossman, W., R. E. Mauri and W. J. Warren. 1985. “Moisture-Altered Viscoelastic Responses of Graphite-Epoxy Composites,” *Advanced Composite Materials-Environmental Effects*, ASTM STP 658, 205-220.

[5] Whitney, J. M. 1969. “Bending-Extensional Coupling in Laminated Plates Under Transverse Loading,” *J. Composite Materials*, 3: 20-28.

[6] Bert, C. W. and B. L. Mayberry. 1969. “Free Vibrations of Unsymmetrically Laminated Anisotropic Plates with Clamped Edges,” *J. Composite Materials,* 3: 282-293.

[7] Whitney, J. M. 1969. “Shear Buckling of Unsymmetrical Cross-Ply Plates,” *J. Composite Materials,* 3: 359-363.

[8] Jones, R. M. 1975. “*Mechanics of Composite Materials,*” McGraw-Hill Book Co, NY.

[9] Hyer, M. W. 1981. "Some Observations on the Cured Shapes of Thin Unsymmetric Laminates," *J. Composite Materials*, 15: 175-194.

[10] Hyer, M. W. 1981. "Calculations of the Room-Temperature Shapes of Unsymmetric Laminates," *J. Composite Materials*, 15: 296-310.

[11] Hyer, M. W. 1982. "The Room-Temperature Shapes of Four-Layer Unsymmetric Cross-Ply Laminates," *J. Composite Materials*, 16: 318-340.

[12] Hamamoto, A. and M. W. Hyer. 1987. "Non-Linear Temperature-Curvature Relationships for Unsymmetric Graphite Epoxy Laminates," *Int. J. Solids Structures*, 23(7): 919-935.

[13] Jun, W. J. and C. S. Hong. 1990. "Effect of Residual Shear Strain on the Cured Shape of Unsymmetric Cross-Ply Thin Laminates," *J. Composite Science and Technology*, 38: 55-67.

[14] Schlecht, M., K. Schulte and M. W. Hyer. 1995. "Advanced Calculations of the Room-Temperature Shapes of Thin Unsymmetric Composite Laminates," *Composite Structures*, 32: 627-633.

[15] Dang, J. and Y. Tang. 1986. "Calculation of the Room-Temperature Shapes of Unsymmetric Laminates," *Proc. Int. Sym. on Composite Materials and Structures* (available Technomic Publishing Co. Inc., Lancaster, PA), 201-206

[16] Jun, W. J. and C. S. Hong. 1992. "Cured Shape of Unsymmetric Laminates with Arbitrary Lay-Up Angles," *Journal of Reinforced Plastics and Composites*, II: 1352-1366.

[17] Peeters L. J. B., P. C. Powell and L. Warnet. 1996. "Thermally-Induced Shapes of Unsymmetric Laminates," *Journal of Composite Materials*, 30(5): 603-626.

[18] Gandhi, M. V. and B. S. Thompson. 1992. "*Smart Materials and Structures*," Chapman and Hall.

[19] Sarris, J. N. and N. A. Aspragathos. 1995. "Development of a Simple Anthropomorphic Robot Hand Using Shape Memory Alloys," IEE Manufacturing Division Colloqium on Innovative Actuators for Mechatronic Systems, 170: 16/1-16/3.

[20] Roglin, R. L. and S. V. Hanagud. 1996. "Helicopter with Adaptive Rotor Blades for Collective Control," *Smart Materials and structures*, 5(1):76-88.

[21] Hebda, A. D. and S. R. White. 1995. “Structural Behavior of SMA Composite Beams,” Proceedings of the 1995 Joint ASME Applied Mechanics and Materials Summer Meeting, Los Angeles, CA, AMD 206: 11-119.

[22] Müller, L. 1979. “A Model for a Body with Shape Memory,” *Arch. Rat. Mech. Anal.*, 70: 61-77.

[23] Tanaka, K. 1986. “A Thermomechanical Sketch of Shape Memory Effect: One Dimensional Behavior,” *Res. Mech.*, 18: 251-263.

[24] Liang, C. and C. Rogers. 1990. “One Dimensional Thermomechanical Constitutive Relations for Shape Memory Materials,” Collection of Technical Papers, AIAA/ASME/ASCE/AHS Structures, Structural Dynamics and Materials Conference, Long Beach, CA, 16-28.

[25] Liang, C. and C. Rogers. 1992. “Design of Shape Memory Alloy Actuators,” *Journal of Mechanical Design*, 114: 223-230.

[26] Brinson, L. C. 1993. “One Dimensional Constitutive behavior of Shape Memory Alloys: Thermomechanical Derivation with Non Constant Material Functions and Redefined Martensite Internal Variable,” *J. Intelligent Material System and Structures.*, 4(2): 229-242.

[27] Bo, Z. and D. C. Lagoudas. 1994. “Comparison of Different Thermodynamic Models for Shape Memory Alloys,” Adaptive Structure and Composite Materials, Analysis and Application, ASME, AD 45: 9-19.

[28] Boyd, J. G. and D. C. Lagoudas. 1994. “A Thermodynamic Constitutive Model for the Shape Memory Materials. Part I. The Monolithic Shape Memory Alloys,” Submitted for publication in *International Journal of Plasticity*.

[29] Chaudhry, Z. and C. A. Rogers. 1991. “Bending and Shape Control of Beams Using SMA Actuators,” *J. Intelligent Material System and Structures*, 2(4): 581-602.

[30] Brand, W., C. Boller, M. S. Huang, and L. C. Brinson. 1994. “Introducing the Constitutive Behavior of Shape Memory Alloys into Adaptive Engineering Structures,” ASME, AMD-vol 189/PVP-Vol. 292.

[31] Boller, C., W. Brand, L. C. Brinson, and M. S. Huang. 1993. “Some Basic Ideas on the Design of Adaptive Aircraft Structures Using Shape Memory Alloys,” 4th International Conference on Adaptive Structures, Köln Germany.

[32] Xu, G., D. C. Lagoudas, D. Hughes, and J. T. Wen. 1996. "Modelling of a Flexible Beam Actuated by Shape Memory Alloy Wires," Submitted for publication to *Smart Materials and Structures*.

[33] Wolfram, S. 1991. "*Mathematica: A System for Doing Mathematics by Computer*," Addison-Wesley Publishing Co., Redwood City, CA.

[34] Saada, A. S. 1974. "*Elasticity Theory and Applications*," Robert E. Krieger Publishing Company, Malabar, Florida.

[35] Contardo, L. and G. Guérin. 1990. "Training and Two Way Memory Effect in Cu-Zn-Al Alloy," *Acta Metall. Mater*, 38: 1267-1272.

[36] Miyazaki, S., T. Imai, Y. Igo and K. Otsuka. 1986. "Effect of Cyclic Deformation in the Pseudoelasticity Characteristics of TiNi Alloys," *Metall. Trans. A*, 17A: 115-120.

[37] Hebda, D. A., M. E. Whitlock, J. B. Ditman and S. R. White. 1995. "Manufacturing of Adaptive Graphite-Epoxy Structures with Embedded Nitinol Wires," *J. Intelligent Material Systems and Structures*, 6: 220-228.

Appendix A Additional comparisons of the experiments with the developed theory

To illustrate how the change in the SMA thermal properties affects the predictions from the developed theory, the predicted laminate response obtained using the values of 25 ^{o}C and 30 ^{o}C for the austenite start temperature is presented in Figs. A-1 to A-4, along with the experimental results presented in Figs. 2-22 to 2-25.

From the figures it can be observed that the occurrence of the laminate snap through is more accurately predicted when the value of 25 ^{o}C for A_{os} is used to compute the predictions, except for the $[60_4/30_4]_T$ laminate. For this particular laminate, the temperature at which the snap through occurs seems to be better predicted with A_{os} equal to 30 ^{o}C. However, it is important to recall that the temperature change at which the predictions were computed was set equal to -197 ^{o}F to obtain good initial predicted curvatures, as was indicated in Table 7-1. This temperature change was lower by about 40 ^{o}F compared to the temperature change selected to compute the predictions for the other laminates. This represents quite a large difference in magnitude. It is not clear how such a decrease in the temperature change can affect the laminate response to applied forces. It may be possible that the predicted response of the laminate using A_{os} equal to 30 ^{o}C is closer to the experimental results than the predictions using A_{so} equal to 25 ^{o}C because the temperature change was smaller in magnitude.

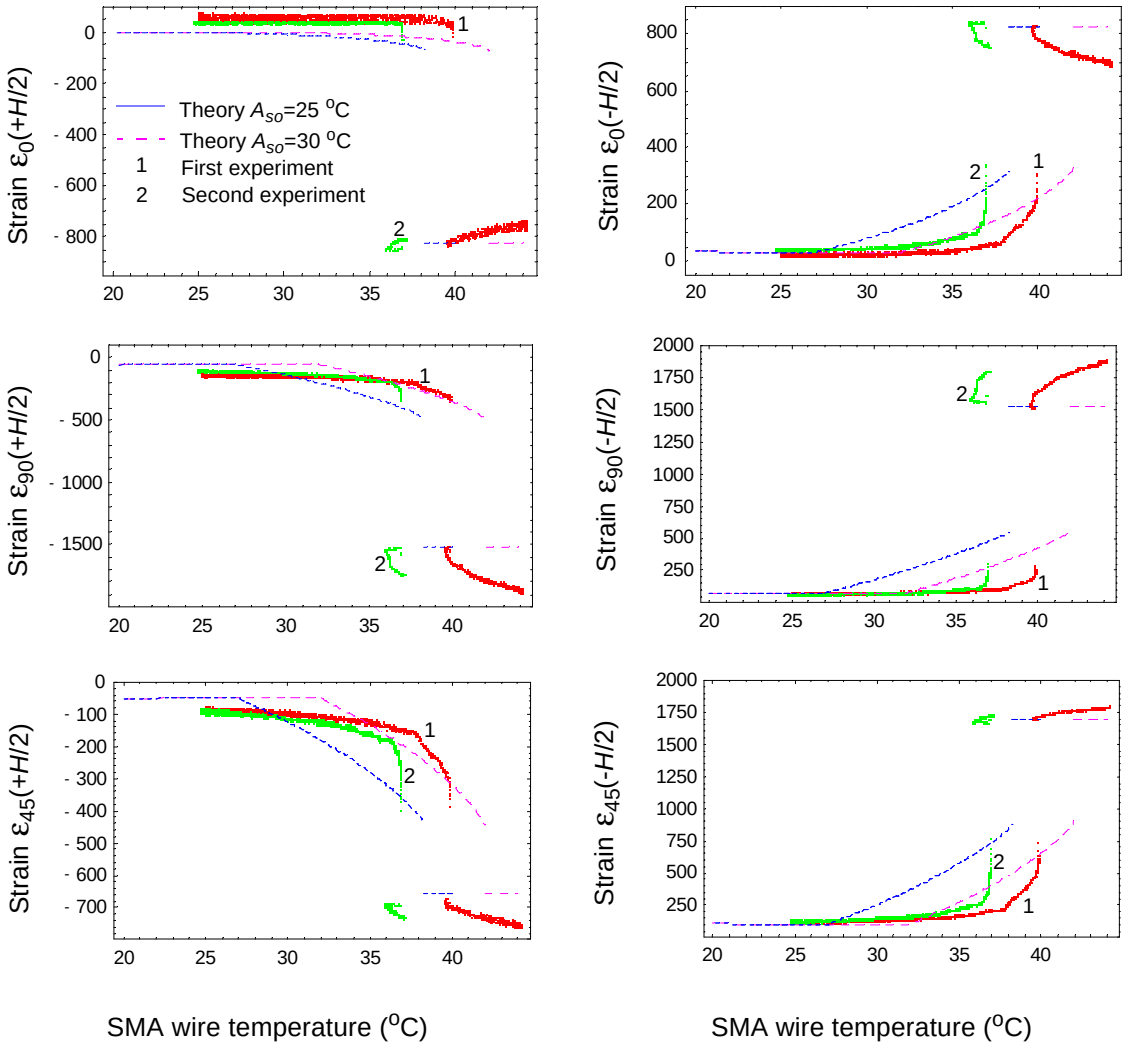

Fig. A-1. Measured and predicted wire temperature-laminate strain relations: $[-30_4/30_4]_T$ laminate

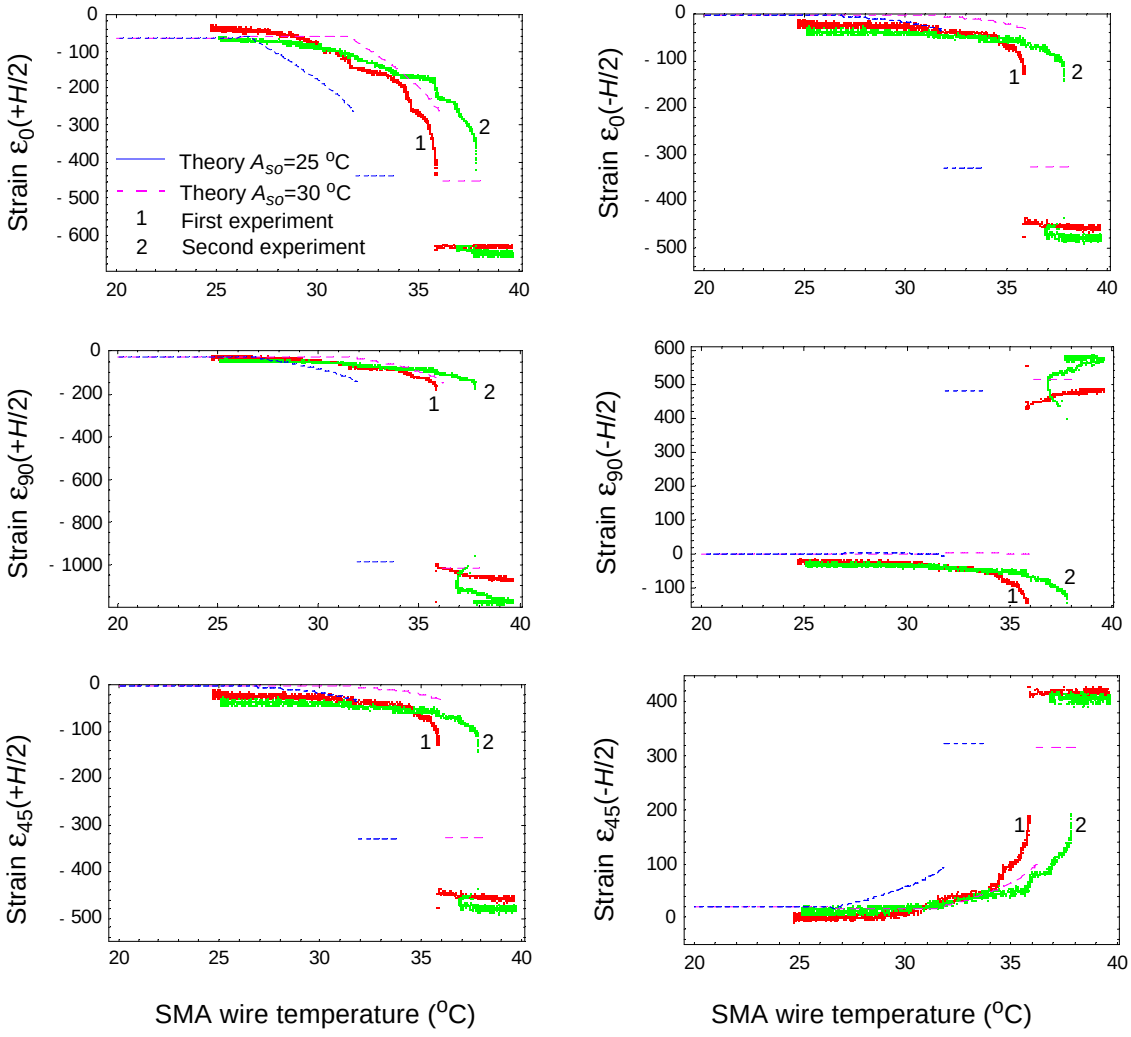

Fig. A-2. Measured and predicted wire temperature-laminate strain relations: $[60_4/30_4]_T$ laminate

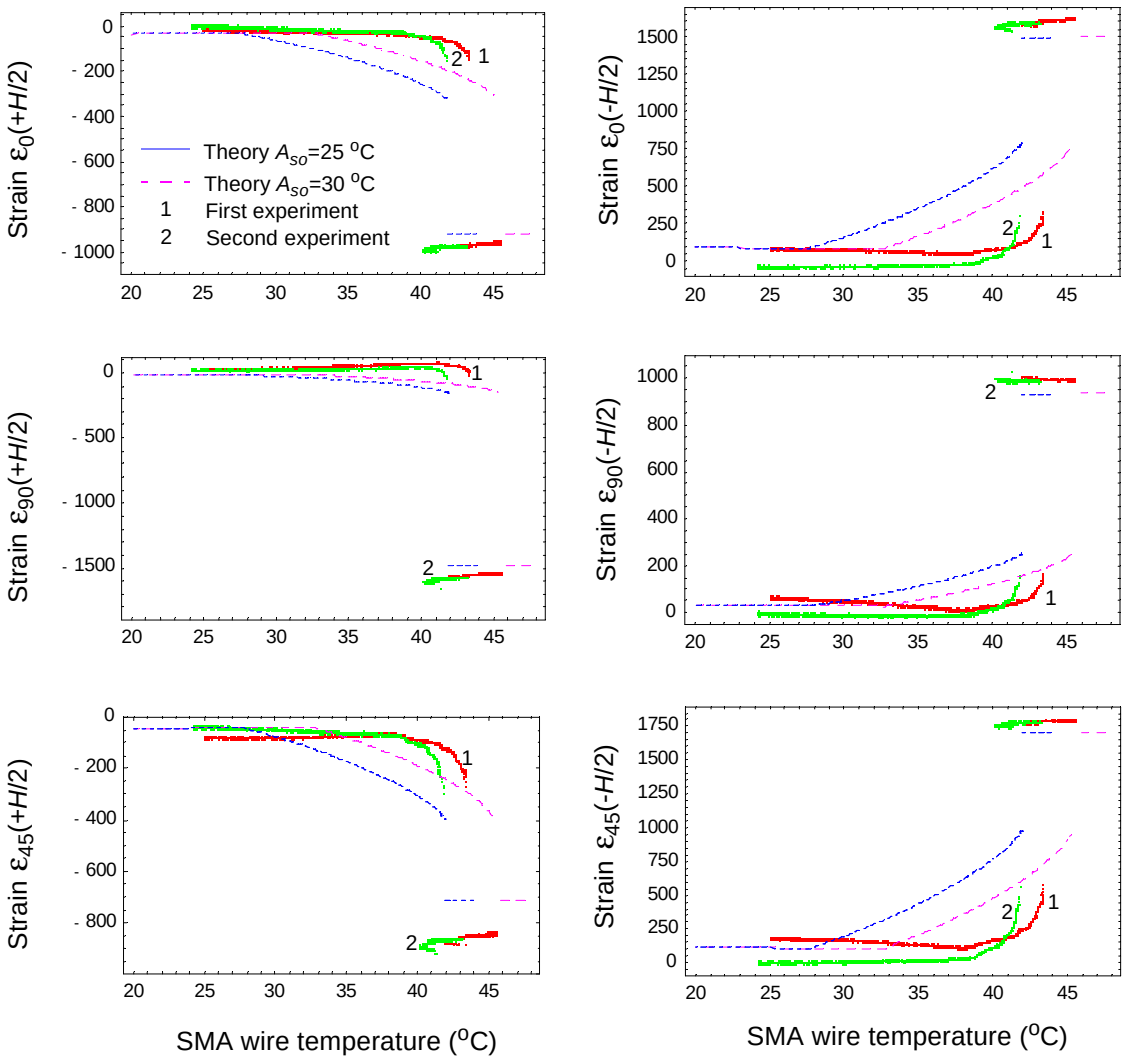

Fig. A-3. Measured and predicted wire temperature-laminate strain relations: $[-60_4/30_4]_T$ laminate

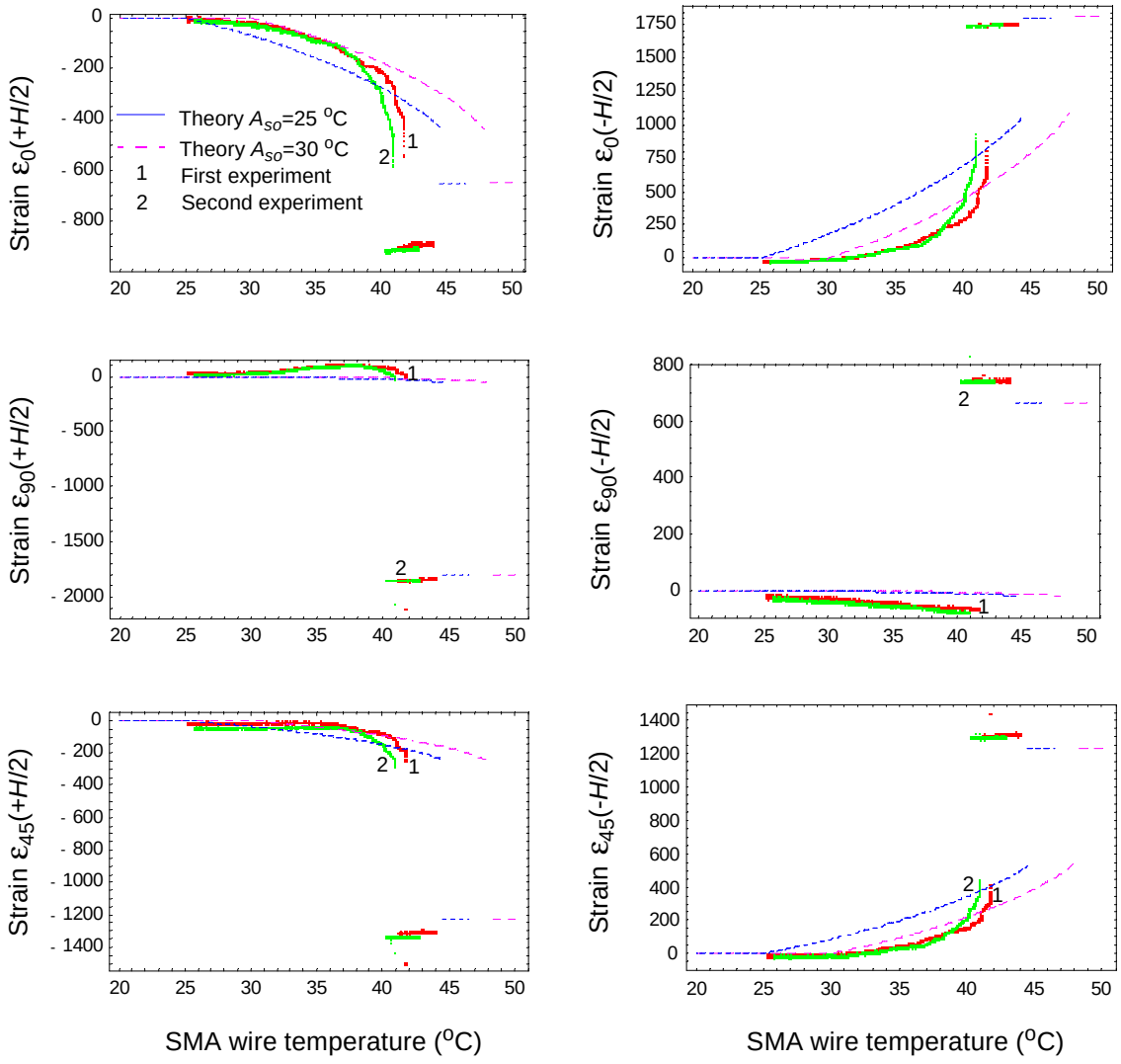

Fig. A-4. Measured and predicted wire temperature-laminate strain relations: $[90_4/0_4]_T$ laminate

Vita

Marie-Laure Dano

The author was born on March 18, 1970, in Saint Cloud, France. Upon completing high school in 1987, she pursued her studies at the *Université de Technologie de Compiègne* (U. T. C.), France, in the department of *Génie Mécanique*. While studying at this university, she participated in the U. T. C.-VirginiaTech exchange program to enroll in the Master Program in the Department of Engineering Science and Mechanics at Virginia Polytechnic Institute and State University in 1991. She received a french *Diplôme d'Ingénieur* in March 1993 and a Master of Science degree in Engineering Mechanics from VirginiaTech in June 1993. She pursued her graduate studies at Virginia Tech and completed her Doctor of Philosophy degree in Engineering Mechanics in April 1997.

Marie-Laure Dano